



HAL
open science

Molecular complexes for artificial photosynthesis

Youngju Ro

► **To cite this version:**

Youngju Ro. Molecular complexes for artificial photosynthesis. Inorganic chemistry. Université Paris Saclay (COmUE), 2019. English. NNT : 2019SACLS412 . tel-02408916

HAL Id: tel-02408916

<https://theses.hal.science/tel-02408916>

Submitted on 13 Dec 2019

HAL is a multi-disciplinary open access archive for the deposit and dissemination of scientific research documents, whether they are published or not. The documents may come from teaching and research institutions in France or abroad, or from public or private research centers.

L'archive ouverte pluridisciplinaire **HAL**, est destinée au dépôt et à la diffusion de documents scientifiques de niveau recherche, publiés ou non, émanant des établissements d'enseignement et de recherche français ou étrangers, des laboratoires publics ou privés.

Molecular complexes for artificial photosynthesis

Thèse de doctorat de l'Université Paris-Saclay
préparée à Université Paris Sud

École doctorale n°571 Sciences chimiques : molécules, matériaux,
instrumentation et biosystèmes (2MIB)
Spécialité de doctorat: Chimie

Thèse présentée et soutenue à Orsay, le 6 novembre 2019, par

Mme Youngju RO

Composition du Jury :

Pierre MIALANE Professeur, Université Versailles Saint-Quentin-en-Yvelines	Président
Sébastien RICHETER Maître de Conférences - HDR, Université de Montpellier	Rapporteur
Yann PELLEGRIN Directeur de Recherches, Université de Nantes	Rapporteur
Eric DORIS Chercheur de CEA, CEA Saclay	Examineur
Charles DEVILLERS Maître de Conférences - HDR, Université de Bourgogne	Examineur
Ally AUKAULOO Professeur, Université Paris Sud	Directeur de thèse



Acknowledgement

I appreciate Prof. Ally Aukauloo for giving me an opportunity to work in Laboratoire de Chimie Inorganique. I remember the moment when I met him first time. He convinced me to go ahead for the research to focus on science. The most memorable sentence which he told me is “I will take the challenge.”. With his impact decision, all situations flowed naturally, and I also reacted to produce fruitful output. I really liked to discuss with him whenever I had curiosity and questions in any kinds of topic. It had always been my strong motivation to go through the meaningful road. Especially, I could learn about Artificial Photosynthesis by approaching various points of view. Thank you for being my supervisor.

I would like to thank Dr. Winfried Leibl. He is my great advisor both in research and life. If someone ask me ‘express him in some words’, without hesitating, I would say ‘wisdom and warmness’, which I like most. We often shared the research idea, tried and finally succeed. Among his teaching for me, mainly I learned photophysics and understood the principle of photocatalysis.

I am thankful to Dr. Zakaria Halime. I was impressed with his passion toward the research. I could learn a lot from the beginning to the end! How to synthesis, characterize metal complexes, control the parameter to make crystal, and work in glove box....all about chemistry! When I asked about science, anytime he opened his heart and he spent time for me. Especially, I will miss his joking which makes me fun during working.

I thanks to Dr. Marie Sircoglou. She took care of my safe and security so I could be careful about my experiment. For the ion pair study, her comments helped me to approach in depth.

Thank you Dr. Annamaria Quaranta. When I used instruments in CEA, she helped me a lot. I was happy when you commented to me for my presentation during weekly seminar. I liked the environment which we could discuss freely.

Many thanks to Dr. Christian Herrero for EPR measurements. I would like to thank Dr. Régis for analysis crystals. Also, lots of thanks to Dr. Eric for the magnetism measurements. You all explained the data analysis carefully and always you welcome me!

I appreciate to Dr. Sébastien Richeter and Dr. Yann Pellegrin who accepted the task of being reporters of my defense. They reviewed my thesis report and commented to support the results. Furthermore, I would like to thank Prof. Pierre Mialane, Dr. Eric Doris, and Dr. Charles Devilliers for examining my thesis.

I always try to find for diverse challenging & rewarding higher education and the SERP-Chem which was my master program in Europe made it possible for me which I am always thankful for. Above all, I thanks to Prof. Sandrine Lacombe who is the director of the SERP-Chem Program, she listened to me always and suggest better way for me not only during master but also during my Ph.D.

I appreciate to people in Institut de Chimie Moléculaire et des Matériaux d'Orsay (ICMMO) at Université Paris-Sud, Institut de biologie intégrative de la cellule (I2BC) at CEA Saclay. In addition, thanks to École doctorale for the financial supporting during my Ph.D.

Last but not the least, I am always thankful to my family members. My study in Europe was fully supported by your love and pray! Jin Choi, my husband since my master in 2014, thanks for his following to cheer me up throughout my Ph.D degree have been memorable. Especially my lovely babies (puppies) Sun & Moon, you are my sunshine and moonlight during day and night. Let's make new road for the bright future together to be happy.

*The goal is not to be perfect by the end.
The goal is to be better today.*

Simon Sinek

Table of contents

Acknowledgement	5
Table of contents	11
Abbreviations	15
0. Thesis Overview.....	19
1. General Introduction.....	23
1.1. Artificial Photosynthesis	23
1.1.1. From biological to artificial photosynthesis.....	23
1.1.2. Global Warming crisis and Solar Energy	25
1.1.3. Photosystem II : Oxygen Evolving Center and Water Splitting	27
1.2. Photoinduced activation of water	28
1.2.1. Water Oxidation, O ₂ evolution.....	28
1.2.2. Ruthenium-based Photosensitizers	33
1.2.3. Study of Water Oxidation using Copper Catalysts	35
1.3. Ion Pair Formation	38
2. Electrochemical Water Oxidation	43
2.1. Introduction	43
2.2. Experimental methods.....	48
2.2.1. Synthesis of Copper complex.....	48
2.2.2. Electron acceptors	48
2.3. Characterizations of Cu ^{II} OPBI.....	52
2.3.1. Cyclic Voltammetry (CV)	52
2.4. Electrochemical water oxidation	54
2.5. EPR spectro-electrochemical experiments	58
2.6. Other Copper complex, Cu ^{II} OBBZ.....	64
2.6.1. CV of Cu ^{II} OBBZ.....	65
2.6.2. Electrochemical water oxidation by Cu ^{II} OBBZ	66
2.7. Photochemical water oxidation	71
2.7.1. Photophysical studies between [Ru(bpy) ₃] ²⁺ and Copper complex	71
2.7.2. Oxygen measurement by Clark Electrode.....	73
2.8. Conclusions & Perspectives	75

3.	Ion pair formation	79
3.1.	Introduction	79
3.2.	Synthesis and Characterizations	83
3.2.1.	Synthesis	83
3.2.2.	Characterizations	84
	A) ^1H NMR analysis of Ligand	84
	B) MS analysis of $\text{CuL}(\text{TMA})_2$	85
	C) IR analysis (MVCl_2 , $[\text{Cu}^{\text{II}}\text{OPBI}](\text{TMA})_2$ and $[\text{Cu}^{\text{II}}\text{OPBI}]\text{MV}$)	85
	D) Crystal structures : $[\text{Cu}^{\text{II}}\text{OPBI}](\text{TMA})_2$ and $[\text{Cu}^{\text{II}}\text{OPBI}]\text{MV}$	86
3.3.	Electrochemical Study	88
3.3.1.	Cyclic Voltammetry (CV)	88
	A) $[\text{Cu}^{\text{II}}\text{OPBI}](\text{TMA})_2$ vs. $[\text{Cu}^{\text{II}}\text{OPBI}]\text{MV}$	88
3.4.	UV-Vis spectroscopy	91
3.4.1.	$[\text{Cu}^{\text{II}}\text{OPBI}](\text{TMA})_2$	91
3.4.2.	Ion pair formation between $[\text{Cu}^{\text{II}}\text{OPBI}](\text{TMA})_2$ and $\text{MV}(\text{PF}_6)_2$	91
3.4.3.	Effect of dielectric constant	95
3.5.	EPR measurements	96
3.6.	$\text{Ni}^{\text{II}}\text{OPBI}$ ($[\text{Ni}^{\text{II}}\text{OPBI}]^{2-}$) and $\text{Cu}^{\text{II}}\text{OBBZ}$ ($[\text{Cu}^{\text{II}}\text{OBBZ}]^{2-}$)	100
3.6.1.	$\text{Ni}^{\text{II}}\text{OPBI}$ ($[\text{Ni}^{\text{II}}\text{OPBI}]^{2-}$)	100
3.6.2.	$\text{Cu}^{\text{II}}\text{OBBZ}$ ($[\text{Cu}^{\text{II}}\text{OBBZ}]^{2-}$)	102
3.7.	Conclusions & Perspectives	104
4.	Intramolecular Electron Transfer	107
4.1.	Introduction	107
4.2.	Synthesis and Characterizations	109
4.2.1.	Synthesis of $\text{Ru}^{\text{II}}\text{LMn}^{\text{III}}$	109
4.2.2.	Characterizations	111
	A) Cyclic Voltammetry (CV)	111
	B) Absorption spectra of complexes and their emission properties	112
4.2.3.	Photophysical Studies : Laser Flash Photolysis	113
	A) $\text{Ru}^{\text{II}}\text{L}$	113
	B) $\text{Ru}^{\text{II}}\text{LMn}^{\text{III}}$	114
	C) $\text{Ru}^{\text{II}}\text{LZn}^{\text{II}}$	116
4.3.	Conclusions & Perspectives	118

References	119
Annex	125
(A) Experimental part.....	125
A.1. Electrochemistry	125
A.2. UV-Visible Spectrophotometry	128
A.3. Infrared (IR) Spectroscopy	130
A.4. Nuclear magnetic resonance (NMR) Spectroscopy	131
A.5. Electron Paramagnetic Resonance (EPR).....	133
A.6. Mass Spectrometry (MS)	136
A.7. Transient Absorption (TA) / Laser Flash photolysis (LFP)	137
A.8. Clark Electrode.....	138
A.9. Glove box system.....	140
(B) Synthesis and Characterizations.....	141
B.1. [Ni ^{II} OPBI](TMA) ₂	141
B.2. Ru ^{II} LMn ^{III}	141
(C) X-ray Crystal Structure.....	143
C.1. [Cu ^{II} OPBI](TMA) ₂ and [Cu ^{II} OPBI]MV	144
C.2. [Cu ^{II} OPBI]MV (in glove box, Oxygen-free condition)	145
C.3. [Ni ^{II} OPBI](TMA) ₂	145
C.4. [Cu ^{II} OBBZ](TBA) ₂	147
References	148
Résumé (en français)	149

Abbreviations

ACN	acetonitrile
ATP	adenosine triphosphate
BE	bulk electrolysis
CA	chronoamperometry
CE	counter electrode
CEEC	chemical-electrochemical-electrochemical-chemical
ClO_4	perchlorate
$[\text{Co}^{\text{III}}(\text{NH}_3)_5\text{Cl}]^{2+}$	chloropentammincobalt chloride
CPE	controlled potential electrolysis
$\text{Cu}^{\text{II}}\text{OBBZ}$	copper (II) N,N-oxamido bis(benzoato)
$[\text{Cu}^{\text{II}}\text{OBBZ}]^{2-}$	copper (II) N,N-oxamido bis(benzoato) dianion
$\text{Cu}^{\text{II}}\text{OPBI}$	copper (II) bisoxamidate
$[\text{Cu}^{\text{II}}\text{OPBI}]^{2-}$	copper (II) bisoxamidate dianion
$[\text{Cu}^{\text{II}}\text{OPBI}] \text{MV}$	isolated $[\text{Cu}^{\text{II}}\text{OPBI}]^{2-} \text{MV}^{2+}$ compound via metathesis
CV	cyclic voltammetry
DMSO	dimethyl sulfoxide
DPV	differential pulse voltammetry
ECEC	electrochemical-chemical-electrochemical-chemical
EE	electrochemical-electrochemical
EECC	electrochemical-electrochemical-chemical-chemical
EtOH	ethanol
FE	faradic efficiency
FOWA	foot-of-the-wave analysis
GCE	glassy carbon electrode
HOMO	highest occupied molecular orbital
ISC	intersystem crossing
k_{obs}	rate constant
LFP	laser flash photolysis
LUMO	lowest unoccupied molecular orbital
MeOH	methanol
MLCT	metal-to-ligand charge-transfer band
$\text{MV}^{\cdot+}$	methylviologen cation radical
MV^0	methylviologen neutral
MV^{2+}	methylviologen dication
NBD	4-nitrobenzenediazonium tetrafluoroborate
NHE	normal hydrogen electrode

Ni^{II}OPBI	nickel (II) bisoxamidate
[Ni^{II}OPBI]²⁻	nickel (II) bisoxamidate dianion
OEC	oxygen evolving complex
OER	oxygen evolution reaction
Pers	persulfate (S₂O₈²⁻)
Ph	phenyl group
PSII	photosystem II
PV	photovoltaics
RDS	rate-determining step
RH³⁺	ruthenium Hexamine, [Ru(NH₃)₆]³⁺
[Ru(bpy)₃]²⁺	tris(bipyridine)ruthenium(II)
[Ru(bpy)₃]^{2+*}	excited state of Tris(bipyridine)ruthenium(II)
[Ru^{II}TMP(CO)]	tetra (2,4,6-trimethyl)phenylporphyrinoruthenium(II)
SCE	saturated calomel electrode
SET-WNA	single electron transfer-water nucleophilic attack
Species_{ox}	oxidized species
TBAP	tetra butyl ammonium perchlorate
TBAPF₆	tetrabutylammonium hexafluorophosphate
TGG	triglycylglycine macrocyclic ligand
TMA	tetramethylammonium
TMAOH	tetramethylammonium hydroxide
TOF	turnover frequency
TON	turnover number
WE	working electrode
WOC	water oxidation catalyst
WOR	water oxidation reaction

0. Thesis Overview

As a preamble, I would like to point out that the present work has been performed only since May 2018. I have carried my research project in the group of 'Artificial photosynthesis' for 17 months only. Given the time constraints, I was not in a position to complete my targeted tasks. In this manuscript, I have gathered my results and in parts I have been able to bring new perspectives and comprehension while in others further studies will be needed to bring more insights.

My thesis work articulates around the theme of Artificial photosynthesis.

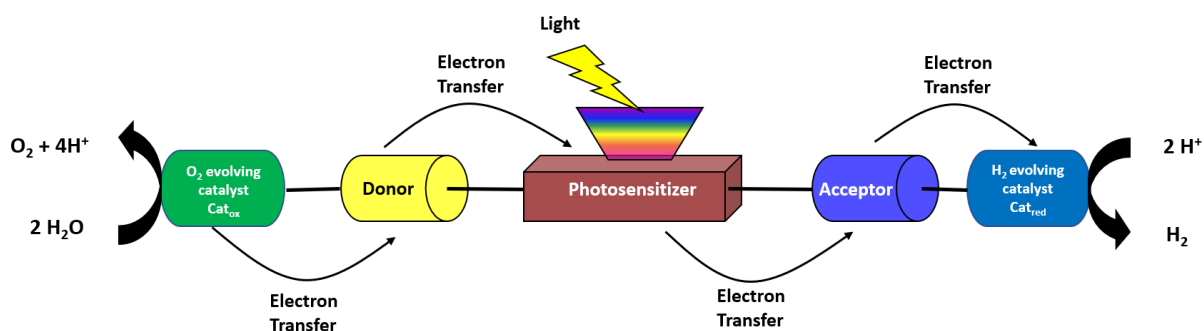


Figure 0-1 Modular supramolecular systems of artificial photosynthesis.

Artificial photosynthesis aims to extract the main principles from natural photosynthesis and put them in 'artificial' device to convert solar energy into chemical energy. It undertakes three main steps : Capture light energy by photosensitizer, transfer this energy in form of charge separated states and generate chemical fuel source in redox reactions (Fig. 0-1).

In this study, first, we approached to the electrochemical water oxidation using copper complex as a catalyst. We then investigated a photocatalytic system using a photosensitizer and a reversible electron acceptor to light activate the copper catalyst. The reversible electron acceptor was used to follow the copper intermediate by electron transfer in transient absorption. To do this, we have investigated the interaction between $[\text{Ru}(\text{bpy})_3]^{2+}$ as a photosensitizer and Cu catalyst. We found that in the light-driven system, $[\text{Ru}(\text{bpy})_3]^{2+}$ was quenched by Cu catalyst in a bimolecular mixture. Surprisingly, we discovered that the color of mixture of the electron acceptor and the copper complex changed to a blue color, typical to the formation of

methylviologen radical ($MV^{\cdot+}$). Thermodynamically, MV^{2+} cannot oxidize Cu complex based on the electrochemical properties. Moreover, the mixture between $[Ru(bpy)_3]^{2+}$ and MV^{2+} nothing had happened in the dark. That is, the crucial trigger for studying ion pair formation based on the puzzling observation when the Cu complex was mixed with methyl viologen (MV^{2+}) in ACN, under anaerobic conditions. The color of the mixture was visibly changed, and the blue color suggested formation of $MV^{\cdot+}$. We reasoned that ion pair formation between the two oppositely charged species could play a role. Finally, light-induced intramolecular oxidation in Ru-Mn supramolecular complexes, which consists of chromophore and catalyst linked di-nuclear molecule were studied to understand the direction of electron transfer steps and to generate oxidized Mn states by exciting the photosensitizer with visible light in the presence of an electron acceptor.

In summary, Chapter 1. General Introduction gives energy issues and artificial photosynthesis in terms of electrochemical and photochemical study of water oxidation. In addition, basic concept of electron transfer and ion pair formation are mentioned. The end of the chapter explains our objectives of this work.

Chapter 2. Electrochemical Water Oxidation gives the characterization of the Cu complexes and their electrocatalysis properties. The high efficiency copper complexes for water oxidation catalysis in electrochemical was revealed. The Cu complexes includes N atoms and O atoms which gives key factor for water oxidation. With the results, we tried to investigate the electron transfer mechanism in photocatalytic system. However, using in photocatalytic system was not successful and it gave another study as following in **Chapter 3**.

In Chapter 3. Ion Pair Formation, we investigated the phenomenon between the oppositely double charged species of Cu complex catalyst and electron acceptor. The electron transfer pathway is the main target of this study.

In Chapter 4. Intramolecular Electron Transfer, we synthesized modular photocatalytic assemblies by using different metal catalysts and Ru-photosensitizers. We have studied the intramolecular electron transfer processes and photophysical characterizations. All detail experimental principles, characterizations and crystal structures of the complexes are described in **Annex**.

Chapter I.

General Introduction

1. General Introduction

1.1. Artificial Photosynthesis

1.1.1. From biological to artificial photosynthesis

Photosynthesis is the process to transform energy from sunlight into chemical energy and it is the most important solar energy conversion system on earth. Photosynthetic products offer fuel by splitting water and converting atmospheric CO₂ into carbohydrates ([CH₂O]_n).^[1,2] However, the efficiency of biological photosynthesis is less than 1 % in most cases so, finding ways to improve the efficiency is crucial point to utilize the nature source.^[3] The process of photosynthesis is well known in terms of biochemically, structurally and functionally.^[4] It consists of two reactions : the light reaction and dark reaction.^[5] In the light reaction, the solar energy is used to split water and then produce electrons. In the dark reaction, by using this chemical energy, CO₂ turn into biomolecules. Overall, in these reactions, diverse complexes catalytic processes are involved with chlorophylls and carotenoids for light absorption and energy transform.^[1]

Based on the concept of biological photosynthesis system, there is another approach to mimic the individual molecular steps. These processes also require complex catalysts as nature does.^[6] It aims to design the system from natural photosynthesis and apply in 'artificial' device to convert solar energy into chemical energy. The point of the system is that it can be stored in material form. Fig. 1-1 ^[7] shows general concept of biological and artificial photosynthesis.

The huge solar energy is challenging for capture and usage point of view that the solution of the problem will bring the new era of energy. There are different approaches using solar energy currently. The possible role of artificial photosynthesis shown in Fig. 1-2.^[7]

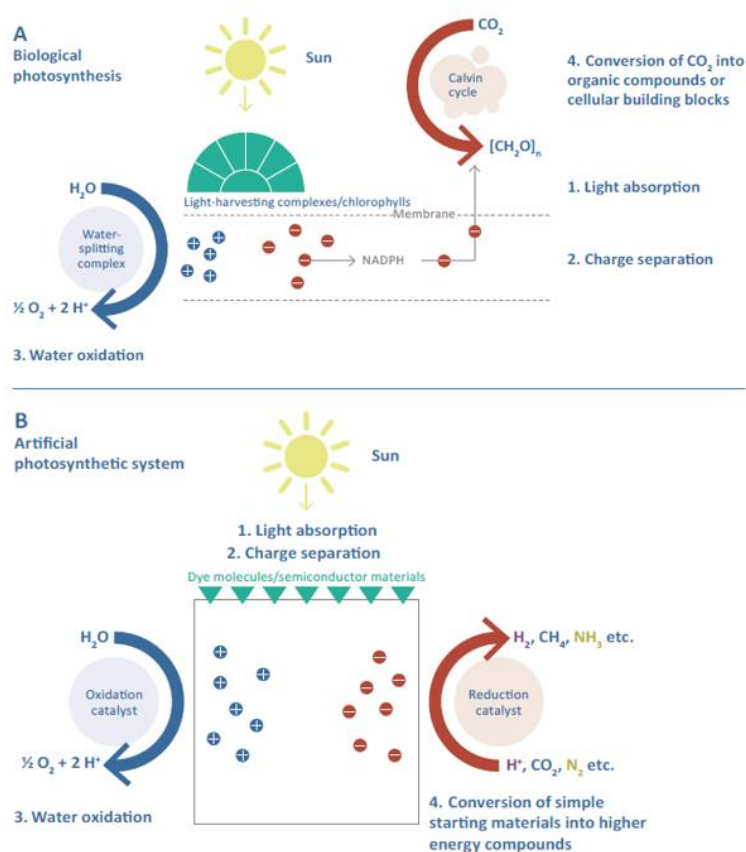


Figure 1-1 Biological photosynthesis (A) and artificial photosynthetic system (B). [7]

The diverse systems for storing solar energy in chemical form can be divided into two approaches : Direct approaches and multistage approaches. Direct approaches are the integration of light absorption, primary charge separation and chemical reactions in a single object.[7] On the other hands, multistage approaches are required the processes in the individual steps. Among the different types of utilization such as solar electricity, solar thermal energy and solar fuel etc., the most challenging task is design highly efficient man-made device to capture and drive the uphill reactions to produce a fuel.[7] In this purpose, research in artificial photosynthesis is focused on the capture and use solar energy to carry out multi-electron involved mechanism and catalytic reactions by using water and carbon dioxide which are renewable sources in nature.

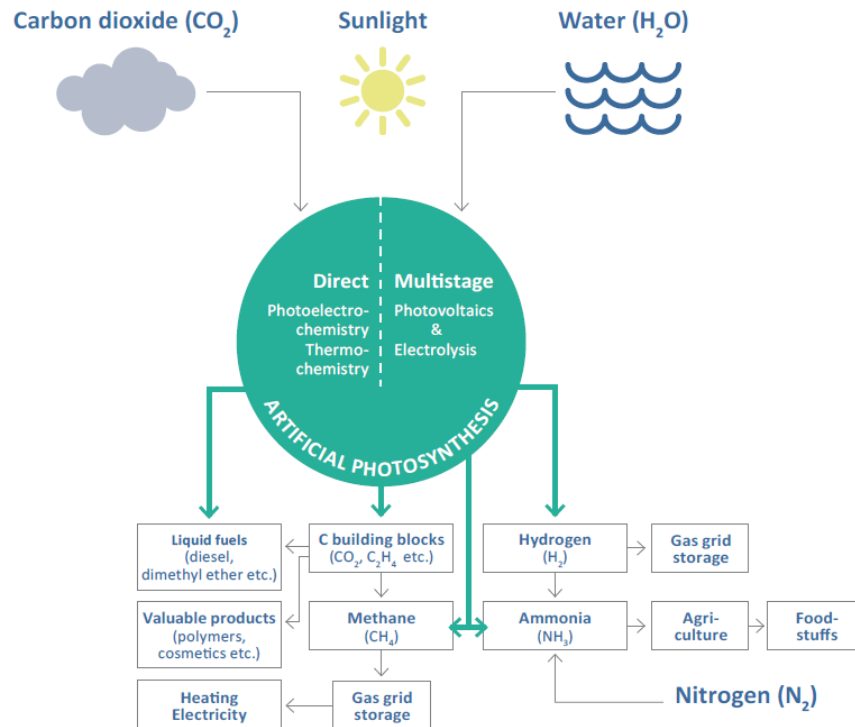


Figure 1-2 Possible role of artificial photosynthesis in the global energy and natural resource system. [7]

1.1.2. Global Warming crisis and Solar Energy

Many scientific experts and associations from countries all over the world made conclusion that more than 95 % of greenhouse effect is affected by human activities. They change the natural greenhouse, so the role of human activity is important to preserve the earth.^[8,9] There are many efforts to prevent both energy crisis and global warming. The energy, which is inexhaustible, clean and non-polluting, we called it 'renewable energy'.^[10] The sources of renewable energy are from nature for example, wind, geothermal, hydro and solar etc. Renewable energy has two important factors, first they do not produce greenhouse gases and are reliable for long-term. Even though they hold high potential for energy source, the efficiency and utilization are not yet at reach.^[11]

Solar power is the highest potential among the diverse renewable energy sources. Fig. 1-3 shows total amount of energy recoverable and the volume of each sphere represents their values in each.^[12,13] The biggest size is solar energy and according to the reference, the energy

consumption of the world has increased nearly 12% to 18.3 TW/yr in 2014. We estimate it will reach 28 TW/yr in 2050. That is, even in 2050, the amount of solar energy in a single day is still more than the entire world consumes in a year.

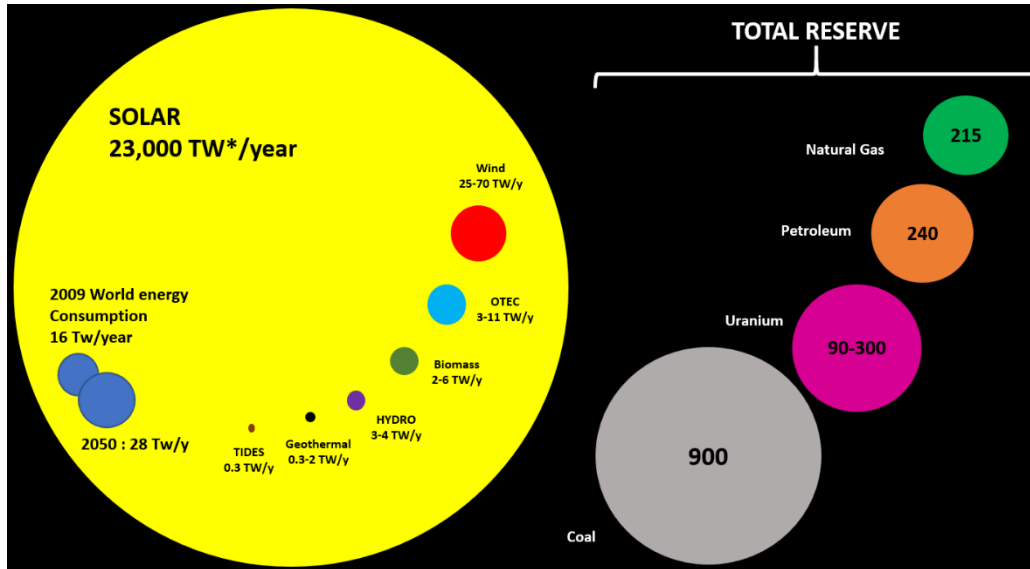


Figure 1-3 Estimate of finite and renewable planetary energy reserves (Terawatt-years). Total recoverable reserves are shown for the finite resources. Yearly potential is shown for the renewables. 2009 World energy consumption is comparing with the other energy resources. ^[13]

A large part of the problem is storage to valorize solar power. That is, it is necessary to find ways to efficiently store solar energy that can provide reliable power. The utilization of the solar energy mainly divided by 2 parts : solar to electricity and solar to fuel. Photovoltaics (PV), battery and thermal storage are included in case of the solar to electricity. The other case, for example, using water and carbon dioxide through the thermal or electrochemical processes finally produce oxygen, methane and hydrogen sorting in 'solar to fuel' part. The latter connects to 'artificial photosynthesis', which approaches to the sustainable solar energy-driven cycle attempting to use catalysts.

1.1.3. Photosystem II : Oxygen Evolving Center and Water Splitting

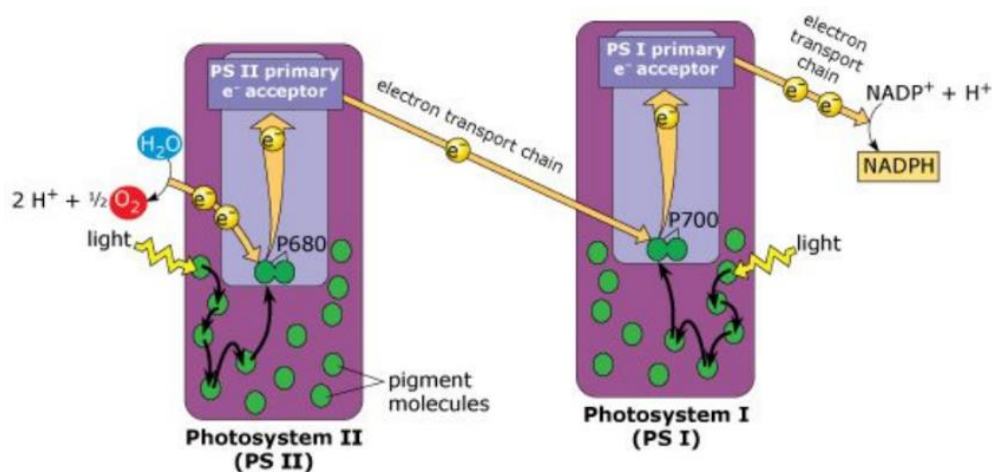


Figure 1-4 Photosystem I & II, copyright © Pearson Education, Inc.

Photosystem II (PSII) is the only enzyme that can use light to drive the water oxidation reaction, and it provides electrons and protons to fix carbon dioxide. The structure of photosystem II consists of two parts : i) A reductant and a strong oxidant species on opposite sides of the membrane is produced by a photochemical charge separating system, and ii) a catalytic module accumulates oxidizing power at a manganese cluster to oxidize water. As shown in Fig. 1-4, the PSII involves the pigment molecules which are called P₆₈₀ capture photons. Then electrons which released by water splitting transfer via various coenzymes and cofactors. In addition, the protons which generated by the oxidation of water have a role to produce ATP and the transferred electrons reduce NADP⁺ to NADPH.^[1,14]

The oxygen evolving center is a Mn₄Ca complex cluster which is the catalytic site for H₂O oxidation.^[15] It is able to oxidize water involving four electrons to oxygen. The different redox states can be described by S-states (S₀–S₄) and the proposed mechanism of four electrons and proton oxidation process suggested by Batista et al.^[16] In Fig. 1-5, it proposes that in the cubane structure, three different manganese ions are connected in each sharing oxidizing property. The water activation occurs then the oxygen-oxygen bond on the manganese ion bring the oxidation process.^[17]

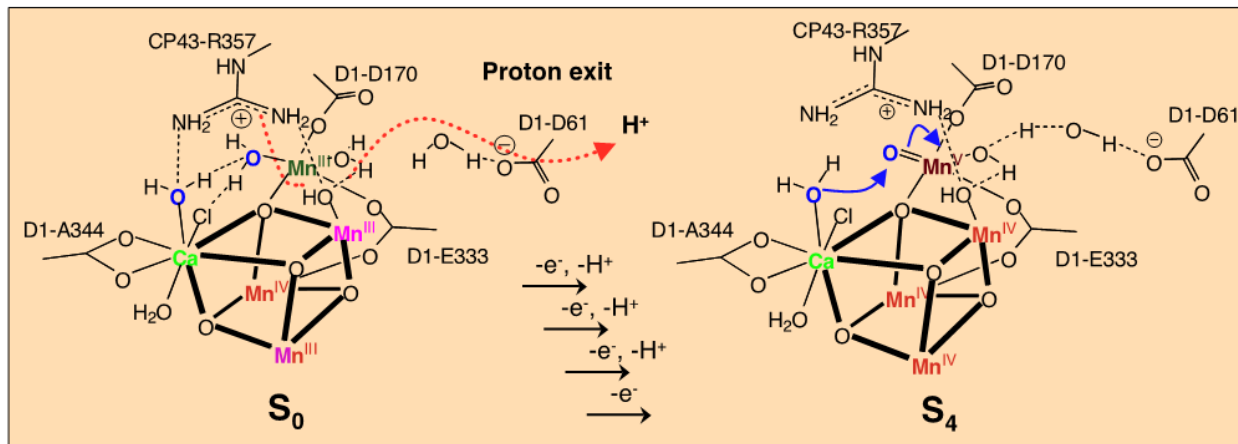


Figure 1-5 Mechanistic proposal for the functioning of the OEC by Batista et al. [16]

1.2. Photoinduced activation of water

1.2.1. Water Oxidation, O₂ evolution

As mentioned in the previous section, water oxidation is a key process in biological photosynthesis. For artificial photosynthesis, the process of water splitting is same as nature, producing four electrons, four protons and oxygen from water as following reaction equation.



At the moment chemists are focusing independently on both reactions i.e. photooxidation of water and the production of H₂. In molecular chemistry, the minimalist system to perform the light driven oxidation of water consists of a photosensitizer (chromophore), a catalyst and an electron acceptor. The photosensitizer is used for light-absorption, the catalyst, in this case, it is for water oxidation catalyst (WOC) and the sacrificial electron acceptor capture the electrons issued from the oxidation of water. A scheme of the functioning of such a system is represented in Fig. 1-6 and the photochemical processes between the photosensitizer and the sacrificial electron acceptor are gathered in scheme 1-1. [18,19]

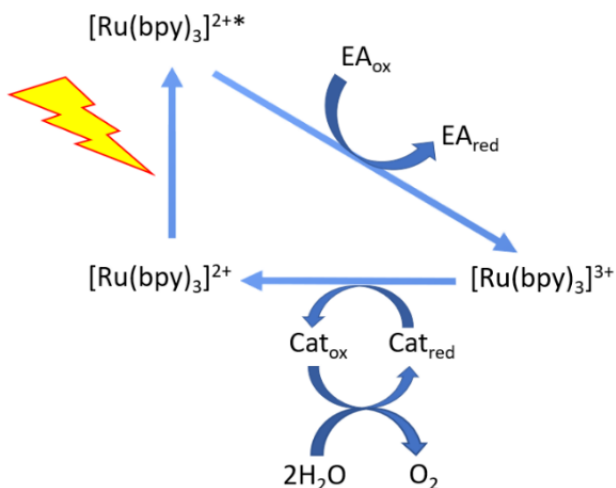
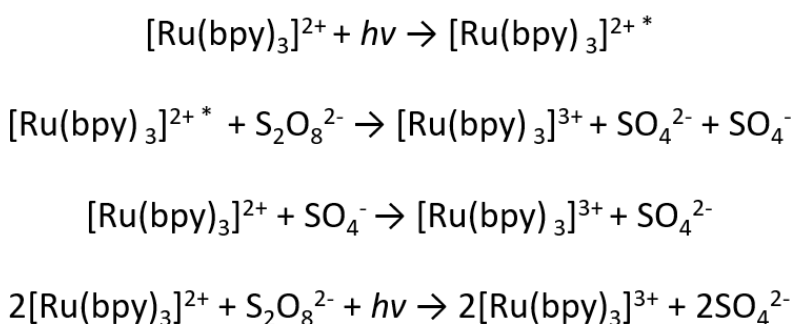


Figure 1-6 Three-component system for light-driven water oxidation consisting of a catalyst, $[\text{Ru}(\text{bpy})_3]^{2+}$ photosensitizer and electron acceptor.



Scheme 1-1 The processes involved in the light-driven persulfate system.^[18,19]

There are three different types of molecular systems depending on the function of the molecules and direct/indirect connection between molecules.^[20]

i) Chromophore/catalyst systems

In these systems, monometallic ruthenium complexes act both as the chromophore and the catalyst. Inoue's lab is the pioneer to report this field.^[21,22] They used tetra (2,4,6-trimethyl)phenylporphyrinoruthenium(II) $[\text{Ru}^{\text{II}}\text{TMP}(\text{CO})]$ as both chromophore and catalyst in the presence of a platinum salt $(\text{Pt}^{\text{IV}}\text{Cl}_2)^{2-}$ as a sacrificial electron acceptor. The light driven epoxidation of alkenes using water gives 60% of quantum yield and 95% of product selectivity.

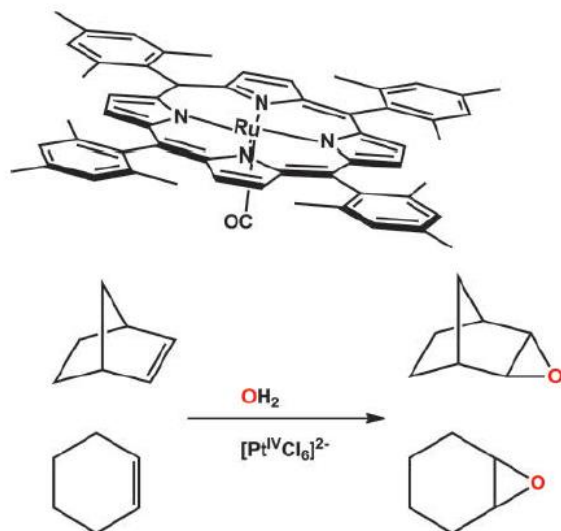


Figure 1-7 Inoue's light driven oxidation of alkenes using water (hydroxide ion) as both oxygen atom and electron donor. [21]

ii) Bimolecular chromophore-catalyst systems

The light capture property and catalysis are being shared by independent photoactive chromophore and a molecular catalyst, respectively. It is a more common method for photochemical multi-electron redox processes. For example, Fukuzumi et al. [23] studied Highly efficient photocatalytic oxygenation reactions using water as an oxygen source. In this study, they reported photocatalytic oxygenation of organic substrates such as sodium p-styrene sulfonate using $[\text{Ru}(\text{bpy})_3]^{2+}$ as a chromophore, sulfonate manganese (III) porphyrin derivatives as photocatalytic oxygenation catalysts and $[\text{Co}(\text{NH}_3)_5\text{Cl}]^{2+}$ as the electron acceptor.

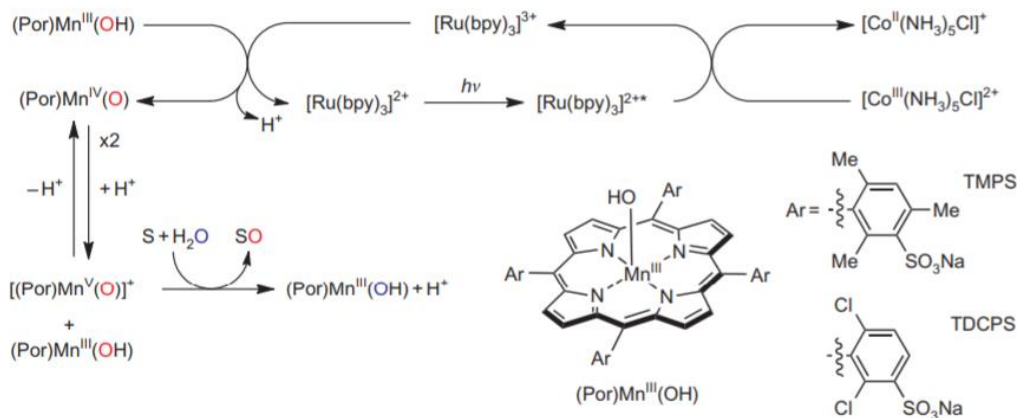


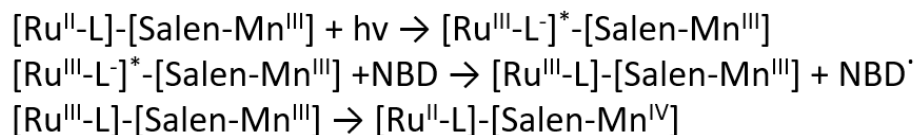
Figure 1-8 Proposed mechanistic pathway for the photocatalytic oxygenation in the Fukuzumi system. [23]

iii) Chromophore–catalyst assembly

In recent years, the field of visible-light-driven catalysis has been developed for oxidation and their electron transfer mechanism.^[24,25] Supramolecular dyads where chromophore and catalyst unit are covalently linked are one of molecular systems in light-driven processes and these assemblies can be integrated in solid electrode surfaces.^[26] They have difficulties for their synthesis with linking a chromophore to a catalyst and the energy quenching mechanisms can bother the desirable role of the sensitizer. However, the strong points of these assemblies are clear that they have stable properties of visible light absorption and provide suitable direction of the electron transfer steps. For example, the design of a proper linker is necessary since supramolecular dyads might be difficult in fast return electron transfer from the excited chromophore to the oxidized water oxidation catalyst.^[27] To mimic the electron-transfer from the nature photosystem, the manganese cluster in photosystem II have been constructed as model of the WOCs.^[28] Applying in supramolecular system, diverse formations of Ru-Mn, where Ru is photosensitizer and Mn act as catalysts have studied.^[29,30]

In 1998, Hammarstrom et al. investigated kinetic analysis of intramolecular, Mn^{II}-Ru^{II} system by flash photolysis experiments in the presence of methyl viologen as reversible electron acceptor. The electron-transfer processes from Mn^{II} to photooxidized Ru^{III} which was quenched by MV²⁺ were reported. EPR measurements were performed that the signal of Ru^{III} and Mn^{II} disappeared rapidly due to the silent properties of Ru^{II} and Mn^{III}.^[31]

Aukauloo et al. have worked light-induced intramolecular oxidation of Ru-Mn supramolecular complexes. Heteroleptic [Ru(bpy)₂L]²⁺ chromophore covalently linked to a Mn^{III}-Salen unit was performed to generate high-valent Mn states by exciting the photosensitizer with visible light in the presence of an electron acceptor. Scheme 1-2. gives the light-induced reactions of the Ru^{II}-Salen-Mn^{III} in the presence of irreversible electron acceptor, 4-nitrobenzenediazonium tetrafluoroborate (NBD). The oxidation states were proved by transient absorption and EPR techniques which correspond to the conversion from Mn^{III} to Mn^{IV}. This study provides the way to control light-induced activation of catalysts in terms of the electron transfer and identity of the oxidized intermediates component.^[32]



Scheme 1-2 Light-induced reactions of the Ru^{II}-Salen-Mn^{III} photosensitizer-catalyst in the presence of irreversible electron acceptor, NBD.^[32]

The promising results obtained with the [Ru^{II}(tpy)(bpy)(OH₂)]²⁺ complex in visible light-driven water oxidation in the three-component component system using ruthenium hexamine ([Ru^{III}(NH₃)₆]³⁺) as reversible electron acceptor. Two different modified Ru-based photosensitizers were coupled to the Ru catalyst and depending on the electronic properties of the chromophores, they work as antenna system by activating the catalyst via energy transfer or direct electron transfer. (Fig. 1-9^[33].)

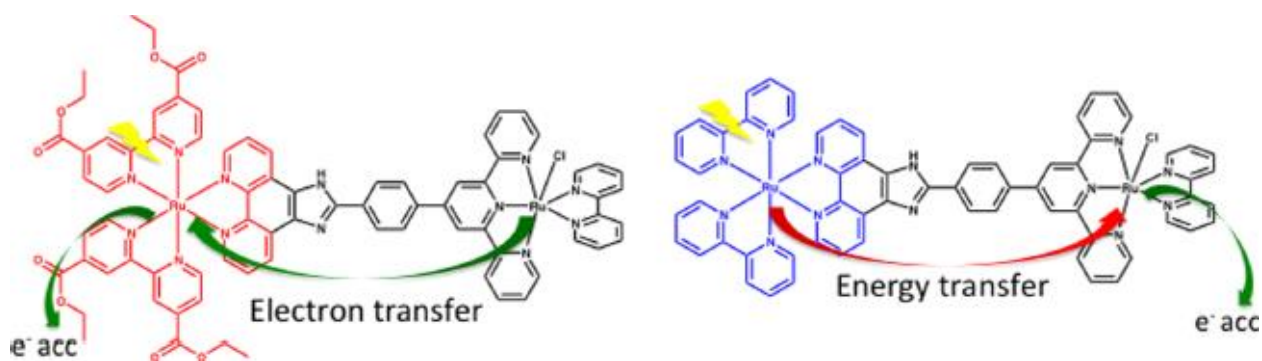


Figure 1-9 Catalyst activation in different photosensitizer upon visible light absorption. ^[33]

1.2.2. Ruthenium-based Photosensitizers

The photosensitizer module is an essential part in the research for the photooxidation of water. Actually, it is the core that will inject the required energy to perform energetically demanding reactions. It absorbs light (ultraviolet or visible region) and produces a charge separated state where after a cascade of electron transfers lead to charge accumulation to perform multielectronic catalysis. Different families of photosensitizers are currently being investigated such as semiconductor quantum dots, inorganic molecular complexes, or organic chromophores.

$[\text{Ru}(\text{bpy})_3]^{2+}$ -type complexes have been widely studied and well known as excellent photo-redox metal-based photosensitizers. They have several advantages that are used in artificial photosynthesis. They are quenched by electron acceptors or donors efficiently. The excited state, $[\text{Ru}(\text{bpy})_3]^{2+*}$ has a longer lifetime than chemical reactions allow to occur: a single-electron oxidation or a single-electron reduction in the presence of an acceptor or a donor, respectively. The photostability is another desirable property. In a large pH range, they perform compatibly and the broad absorption of visible light is an attractive point. Modification of the ancillary ligands controls their photophysical and electrochemical properties in terms of the absorption of light region extension and redox potential. Fig. 1-11 shows the photophysical features of $[\text{Ru}(\text{bpy})_3]^{2+}$.^[34] The potential of oxidation species, $[\text{Ru}(\text{bpy})_3]^{3+}$ is around 1.33 V vs. SCE and it is close to the primary donor of PSII, P_{680}^+ . That is, it can be a good candidate to reproduce the oxidation reactions.^[35,36] The light absorption at $\lambda_{\text{max}} = 450 \text{ nm}$ which is investigated by flash photolysis is the typical property of $[\text{Ru}(\text{bpy})_3]^{2+}$, and it makes excitation of an electron in a metal-centered orbital to a π^* orbital located on the ancillary polypyridyl ligand. It is called 'metal-to-ligand charge transfer (MLCT)'. That is, a singlet excited state $^1[\text{Ru}(\text{bpy})_3]^{2+*}$ goes to intersystem crossing (ISC), affording a triplet state, $^3[\text{Ru}(\text{bpy})_3]^{2+*}$ which is relatively long lived.^[37-39]

To modify the bipyridine ligands, synthetic handles are possible to change substituted ligands with electron donating or withdrawing groups. The modification of the ligand changes the photophysical properties of the complex such as the emission lifetimes and bathochromic shifts. The addition of ester or carboxylate groups was shown around 50 nm of bathochromic shifts due to the energy level of $d\pi$ and p^* orbital.^[40,41] Depending on the properties of substitutions,

their oxidation potentials are in the range from 1.0 to 1.54 V vs. NHE. Fig 1-10 gives examples of ruthenium-based complexes such as $[\text{Ru}(\text{bpy})_3]^{2+}$, $[\text{Ru}(\text{bpy})_2(\text{deeb})]^{2+}$ and $[\text{Ru}(\text{bpy})(\text{deeb})_2]^{2+}$. In this part, we focus on the derivatives of the $[\text{Ru}(\text{bpy})_3]^{2+}$ complex as the photoactive chromophore unit.

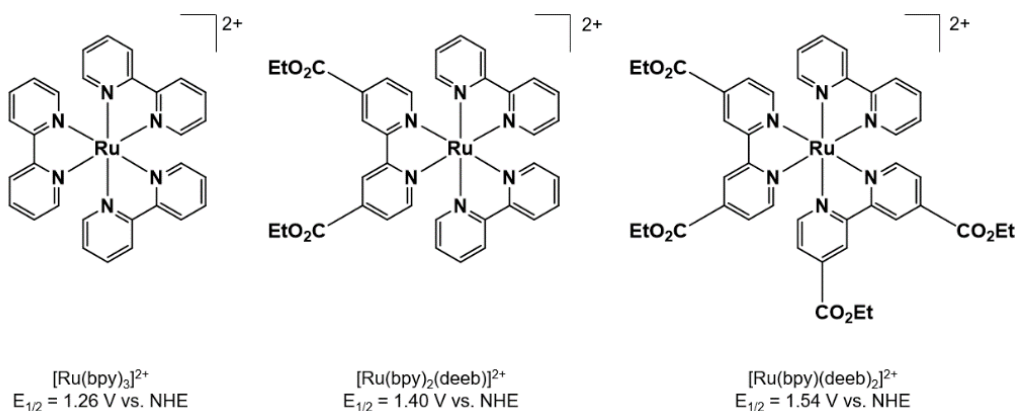


Figure 1-9 Examples of $[\text{Ru}(\text{bpy})_3]^{2+}$ -derivative photosensitizers.

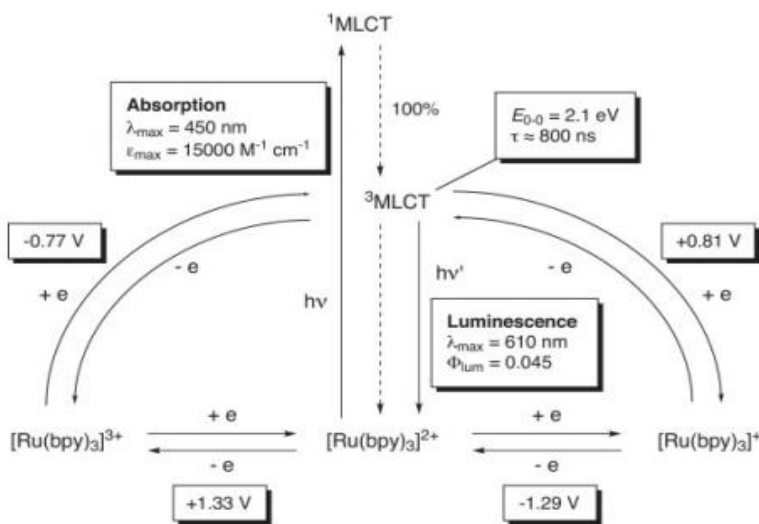


Figure 1-10 One electron excitation and redox behavior of $[\text{Ru}(\text{bpy})_3]^{2+}$ ($E / \text{V vs. SCE}$).^[34]

1.2.3. Study of Water Oxidation using Copper Catalysts

One of the main challenges to water splitting is the development of robust WOCs with high efficiency, low overpotentials, good stability and high turnover rates.^[42] Water oxidation catalysts divided by heterogeneous and homogeneous catalysts.^[43] The heterogeneous catalysts such as transition-metal oxides or hydroxides are the active species and they have high durability and activity.^[44,45] On the other hands, homogeneous catalysts which assisted by molecular complex design, have active metal centers coupled with functional ligand that offer merits for mechanistic studies.^[46] In order to obtain low toxicity and earth abundant metals, recently the first-row transition metals such as Fe, Cu, Co, Mn and Ni have been identified.^[47-49] Homogeneous copper molecular catalysts for water oxidation have been remarkable developed due to their relatively high reactivity and stability under the highly oxidative conditions of the catalysis.^[50,51] Besides, they have emerged with well-defined redox properties and coordination chemistry.^[52,53] For water oxidation, the high thermodynamic potential required (1.23 V vs NHE at pH 0.0), means that having the lower potential which can be applied in commercial applications is important factor and it can be modulated by using oxidatively rugged ligands in homogenous catalysts system. Therefore, this chapter summarizes the recent advances that have been made in designing copper based WOCs for water oxidation.

The first report of homogeneous copper catalysts has been reported since 2012 by Mayer and co-workers.^[54] The examples of copper-based water oxidation catalysts (Fig. 1-11) contain N-donor ligand which has capability of stabilizing the metal-oxo intermediates in transition metal-catalyzed oxidations were recently studied as OEC by giving key catalytic properties (Table 1-1). To evaluate the performance of catalysts, the typical characterizations such as working overpotential, catalytic activity, turnover number (TON), turnover frequency (TOF) and faradic efficiency are the electrocatalytic parameters. Table 1-1. shows a set of electrochemical parameters and kinetic data for Cu complexes described previously in the literature. Most of the experiments have been explored under the basic electrolyte conditions rather than mild conditions. The lowest overpotential value is 0.17 V (**E 2**) mentioned by Llobet.^[55]

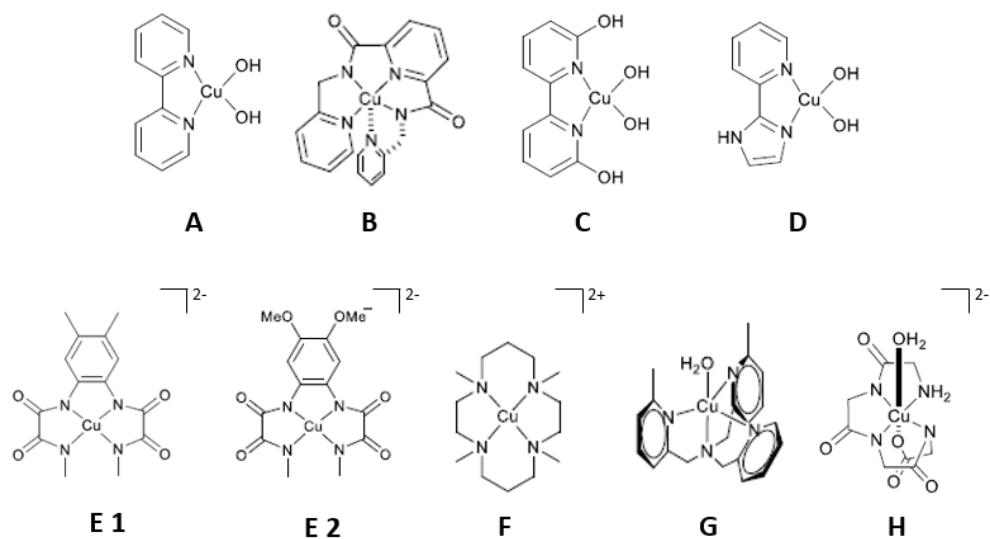


Figure 1-11 Examples of copper-based water oxidation catalysts.

Table 1-1 . Kinetic and Electrochemical data of copper-based complexes water oxidation catalysts

Catalyst	pH	η / V	k_{cat} / s^{-1}	TON
A ^[54]	12.5	0.75	100	30
B ^[56]	8.0	0.64	20	19
C ^[57]	12.4	0.64	0.4	1
D ^[58]	12.0	0.30	35	N/A
E1 ^[55]	11.5	0.40	3.6	0.5
E2 ^[55]	11.5	0.17	0.16	0.5
F ^[59]	7.0	0.88	7	N/A
G ^[60]	12.5	1.00	33	1.43
H ^[51]	11.0	0.52	33	13

The complexes **E** series have been studied as function of the strength of the electron-donation group. In addition, the equatorial N donor ligand-set complexes show the oxidatively stable. In the recent studies of Cu complexes for water oxidation '**E 2**' has the lowest overpotential value.^[55] The fastest complex **A** has quite higher rate constant 100 s^{-1} at pH 12.5 and overpotential is 750 mV.^[54] The Other complexes (**B**, **G**, **D** and **H**) of rate constants are between $20 - 35 \text{ s}^{-1}$. In 2013, Mayer et al., provided Cu^{II} complex with triglycylglycine macrocyclic ligand (TGG⁴⁻) for electrolytic water oxidation, [(TGG⁴⁻)Cu^{II}-OH₂]²⁻ (Figure 1-12, **H**).^[51] The potentials which were measured by CV happened at $E_{1/2} = 0.58 \text{ V}$ and 1.32 V vs NHE. The first reversible peak potential corresponds to oxidation of Cu²⁺ to Cu³⁺ and the irreversible 2nd oxidation current peak appears remarkable which occurs the onset potential for water oxidation at around 1.10 V vs. NHE that overpotential is 0.52 V . The highlight part of this study is that they proposed the mechanism for electrocatalytic water oxidation providing intermediate states. Fig. 1-12 Indicates that the first stage starts Cu^{II} oxidation, Cu^{II/III} then appear Cu^{IV} peroxide intermediate, Cu^{IV}=O, losing one proton and one electron. This propose attribute to bring new idea to improve ligand system catalysts.^[51]

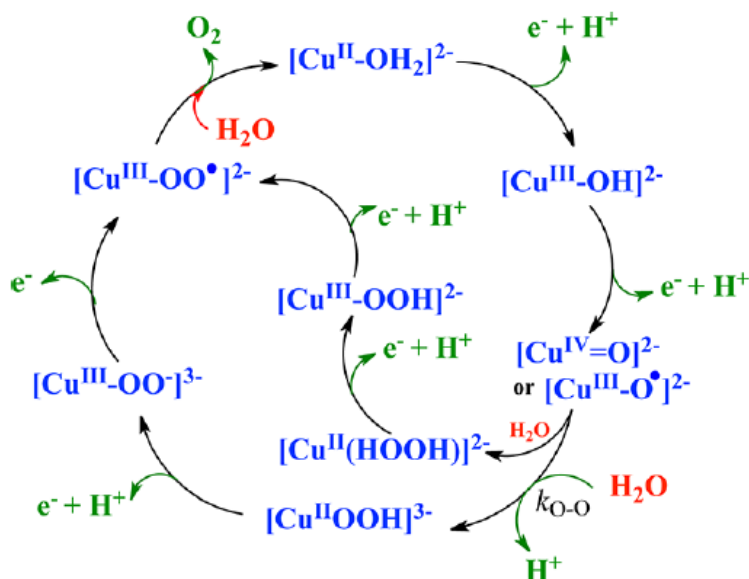


Figure 1-12 Proposed mechanism for water oxidation by 'H' in phosphate buffer solutions at pH 11. ^[51]

1.3. Ion Pair Formation

The presence of photosensitizer, electron donor (or acceptor) and catalyst are typical conditions in the study of photocatalytic activity. Depending on their properties such as potentials, electrical charge numbers, absorption wavelength and competition reactions etc., choosing carefully suitable combinations is necessary. A possible phenomenon to occur is ion pair formation between these elements which might affect the bimolecular electron transfer. For the ion pair formation charge number of anion and cation is the main factor to consider together with the dielectric constant of the solvent.

Ion pair formation is an association between positive ion and negative ion temporarily by coulomb attraction (electrostatic force) without formation of a covalent bond. The two opposite charge ions bond together and dissociation are followed by electron transfer.^[61]

Based on the theory of 'Bjerrum ion pair^[62]', when the oppositely charged ions are closer than its centers distance, it formed an ion pair.

$$q = \frac{8.36 \times 10^6 Z^+ Z^-}{\epsilon_r T} \text{ pm}$$

Z^+, Z^- : charge numbers of the ions

ϵ_r : relative permittivity (dielectric constant)

T: Temperature

It consists of Contact (intimated or tight) Ion Pair, Solvent Shared Ion Pair and Solvent Separated (loose) Ion Pair.

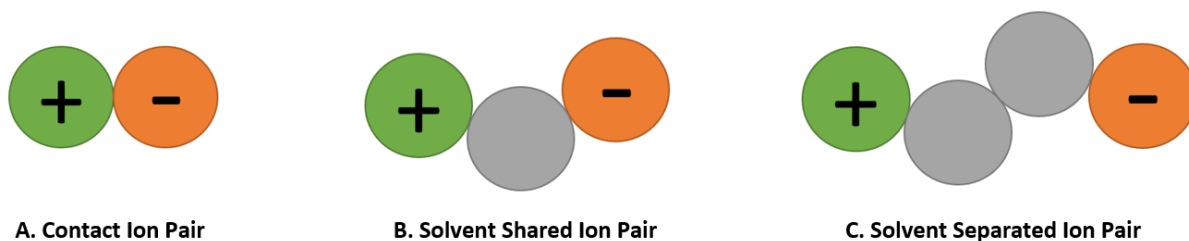


Figure 1-13 Diverse Ion-Pair formations

Contact ion pair (intimate or tight ion pair) is formed in direct contact between oppositely charged ions. The other ion pairs are separated by solvent or neutral molecules so they can be described as 'solvent shared ion pair' which is separated by one single solvent molecule and 'solvent separated ion pair' which involves more than one solvent molecule, we called it 'loose ion pair'. In case of loose ion pair, it is possible to interchange with other ions and it can be verified by analytical techniques. That is, by using diverse experiments the different of tight and loose ion pairs can be detectable. For example, the contact ion pair affect to the optical absorption spectrum due to their tight contact between the cation and anion.^[63-65] That is, the coordinated shell from the tight pair vs. the free formed pair make high entropy in this case so temperature may influence to be more tight ion pair. The other cases, in the solvent separated ion pair has less effect on the spectrum.^[63-65]

This part is a brief definition of ion pair formation to understand why it considered in this study. Even though there are many studies of ion pair formation, the association of oppositely charged ions which results in bimolecular electron transfer is surprisingly discovered in this study. It can be the extended subject in 'artificial photosynthesis' in the electron transfer point of view. We will explain the experimental evidence and describe the effect of diverse factors such as dielectric constant of solvent, counter ions and temperature etc.

Charter II.
Electrochemical
Water Oxidation

2. Electrochemical Water Oxidation

This chapter is about the water oxidation using copper complexes as catalysts. The Cu (II) complex, Cu^{II}OPBI has been investigated for electrochemical water oxidation in 2015 by Llobet. Recently, our lab collaborated with Prof. Abhishek Dey to extend the study of the Cu (II) complex, having different electron donating and withdrawing substituent. In EPR spectro-electrochemical point of view, the studies helped to sequence the elementary electrochemical and chemical events leading towards the O₂ formation selectively at the copper center. Therefore, the study of OER and mechanism of water oxidation using Cu^{II}OPBI has been submitted for publication (Title : Ligand Radical Mediated Water Oxidation by a family of Copper o-Phenylene Bis-Oxamidate Complexes)

Here, I summarized the paper which I contributed as a 3rd author. In addition, I put some trials which we applied in a photocatalytic system using a photosensitizer and a reversible electron acceptor to light activate the copper catalyst. Even though the photocatalytic system was not successful, it led us to a new finding that we discuss in Chapter 3.

2.1. Introduction

Water oxidation reaction (WOR) is indisputably one of the main hurdles in developing sustainable ways to store solar energy.^[66–68] This half reaction provides the electrons and protons for further synthesis of H₂ or reduction of CO₂ in energy rich compounds.^[69,70] In Nature, a Mn₄Ca cluster, known as the Oxygen Evolving Complex, located at the heart of Photosystem II, is the locus where this reaction takes place.^[1,71] Both the advancement on the functioning of this enzyme and effort of chemists to develop robust catalysts are bringing this target closer to reality.^[2,72] If much success has been achieved with ruthenium and iridium complexes in this quest, there is still an urgent need to elaborate cost-efficient catalysts based on more abundant metal.^[73–76]

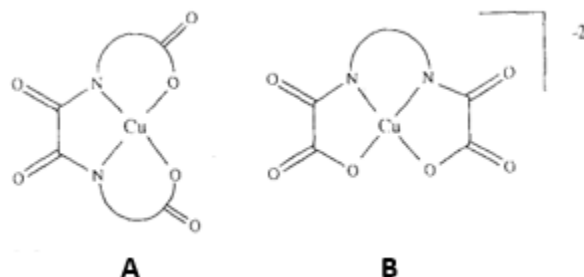
While, close structural mimics of the OEC have been achieved however their catalytic reactivities have not met our expectations yet.^[77,78] On the contrary, significant progress in catalytic water oxidation has been made with iron, cobalt, and manganese complexes in the homogeneous medium by the addition of chemical oxidants such as Cerium (IV) or Ruthenium (III) salts.^[47–49]

Recently, copper complexes have joined the short list of molecular catalysts for the WOR.^[54,79] Reasons behind this stem probably from the copper oxygenases functions where O₂ activation leads to the cleavage of the O-O bond leading to highly oxidized copper species.^[80] Hence reversing the activation steps from H₂O to form O-O bond is an attractive perspective. Mayer and coworkers, first exemplified such strategy in the electrocatalytic OER with a dinuclear bipyridine Cu^{II} di- μ -hydroxo.^[54] While, Meyer and coll. discovered that single site copper complexes with the particularity of having deprotonated amido functions in the coordination sphere were effective electrocatalysts for O₂ release.^[79] Mechanistically, a Cu (III) intermediate was clearly depicted. However, no clear spectroscopic signature has yet been unraveled for the formal Cu (IV) active catalytic species.^[79] An alternate electronic structure proposed for this intermediate is a Cu (III)-ligand radical species. More recently Llobet and coworkers have reported on the electrocatalytic water oxidation with a copper (II) bis-oxamidate complex.^[55,81] Here too, a Cu (III)-radical species has been invoked in the oxygen-oxygen bond formation. The authors put forward an original mechanism for the O-O bond formation tagged as SET-WNA (Single Electron Transfer - Water Nucleophilic Attack), where no direct Cu-O intermediate is pertained during the catalytic cycle.^[55] Such a proposal has caught our attention and we have been interested to use electrochemical techniques coupled to EPR spectroscopy to gain insights in the mechanistic routes for the O₂ formation in the SET-WNA scenario.^[55]

Polyanionic chelating ligands were found to stabilize the unusual Cu (III) oxidation state as evidenced with *o*-phenylene-bisamidate ligands.^[82,83] Further studies also evidenced that these families of ligands could be the siege for competitive ligand vs. metal centered redox behavior depending on the substitution pattern on the aromatic ring.^[53,84] The recent findings that in basic medium the single site copper (II) bisoxamidate (OPBI) complexes were potential candidates for the WOR have prompted us to interrogate the electronic properties of the activated forms.

The oxamate dianion can be used to make mono and polynuclear complexes by formation of either a bidentate or a bis-bidentate metal coordination. It is well known that the transition metal ions are stable in high oxidation states due to the deprotonation of amide nitrogen atoms which are strong sigma and pi donating ligands. Cu (II) and Ni (II) complexes with oxamide-based ligand are examples for the stabilized high oxidation states of the metal ions.^[85] Scheme 2.1. shows the

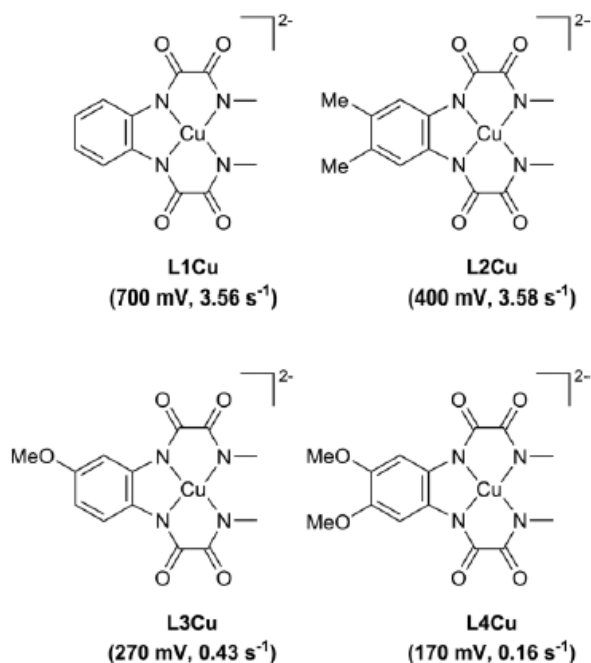
mononuclear oxamato-copper (II) complexes which coordinate to divalent to copper via carboxylate (A) and N-amido (B) groups.^[86]



Scheme 2-1 Mononuclear oxamato-copper(II) complexes : via (A) carbonyl and carboxylate and (B) carbonyl oxygen atoms.

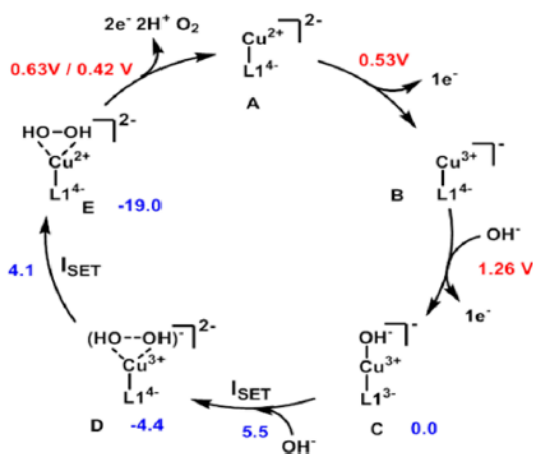
Unfortunately, some limitations have been mentioned that such as the easy hydrolysis of oxamato groups.^[86,87] To solve these problems, N,N'-bis(coordinating group-substituted) oxamides are desirable since they are more stable towards hydrolysis. Polar pendant arms can help to improve solubility. Moreover, the Cu (II) complexes, which include substituted oxamide having five- or six-membered chelate rings, the dissociation and coordination of the amide group might be occurring simultaneously in low pH range.^[87-89]

The Cu (II) complex, Cu^{II}OPBI has been investigated recently for electrochemical water oxidation. In 2015, Llobet and co-workers reported the tetraamidate copper complex **L1Cu** (where L1 is the ligand N1,N1'-(1,2-phenylene)bis(N2-methyloxalamidate)) as WOC.^[55]



Scheme 2-2 Copper complexes with different ligand structures together with their overpotential and turnover frequency for electrocatalytic water oxidation.

The modified ligands which incorporate more electron donating substituents on the phenyl ring play a crucial role in the catalytic performance. The results show that the overpotential decreased from 700 mV to 170 mV when the ligand is substituted with strong electron donating groups. (L1 → L4, scheme 2-2). A catalytic mechanism was proposed based on free energy calculation and determined ligand oxidation as important step as shown in scheme 2-3.^[55]



Scheme 2-3 Calculated catalytic cycle. Free energy changes for reaction steps occurring at the electrode are indicated explicitly in volts (red) and for steps in solution are indicated in kcal/mol (blue).^[55]

In this study, we focus on the development of such catalysts based on earth-abundant copper complexes. The synthesis and characterization of a monomeric Cu (II) complex with tetraanionic chelating ligands N,N'-o-phenylenebis(methylamide) are described. The electrochemical behavior of this complex was investigated by cyclic voltammetry (CV) and electrocatalytic activity for water oxidation was observed. The study of OER and mechanism of water oxidation using Cu^{II}OPBI was investigated by EPR spectro-electrochemistry. In addition, considering its properties as electrocatalyst, it was studied in a photocatalytic assay for water oxidation comprising of Ru-based photosensitizer and diverse electron acceptors to find out whether dioxygen can be evolved or not. The measurement of the dioxygen gas was performed by a Clark Electrode.

2.2. Experimental methods

2.2.1. Synthesis of Copper complex

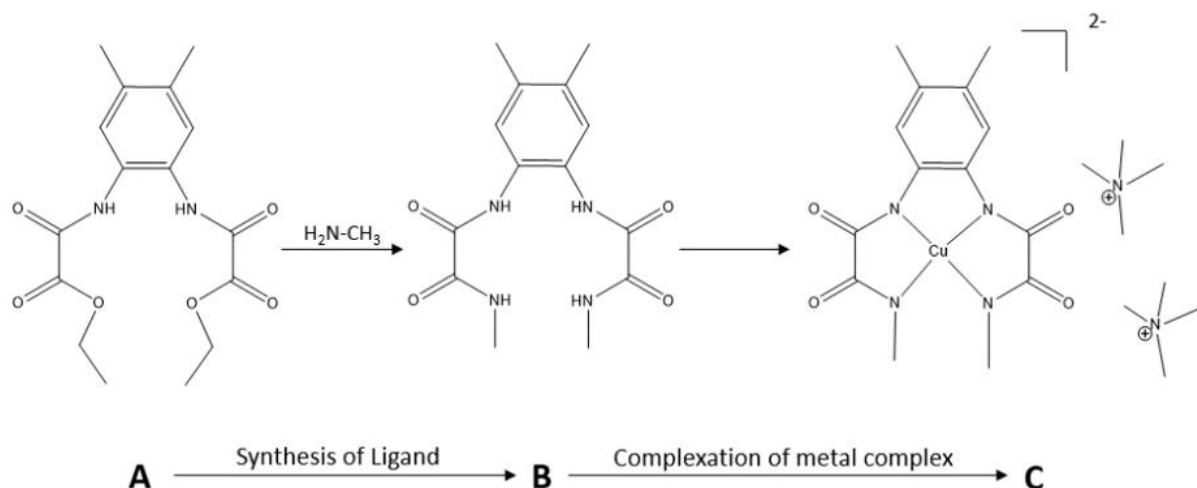


Figure 2-1 Synthesis procedure, A \rightarrow B. Synthesis of Ligand, B \rightarrow C. Complexation of Cu (II) Complex (Cu^{II}OPBI).

The synthesis was performed in 2 steps : Synthesis of ligand (A \rightarrow B), complexation of metal and ligand (B \rightarrow C). In the synthesis procedure B \rightarrow C, the metal complexes, Cu (II) was prepared by treating the dissolved proligand in MeOH with a base (tetramethylammonium hydroxide, TMAOH) followed by the addition of the corresponding metal salt ($\text{Cu}(\text{ClO}_4)_2 \cdot 6\text{H}_2\text{O}$).^[82]

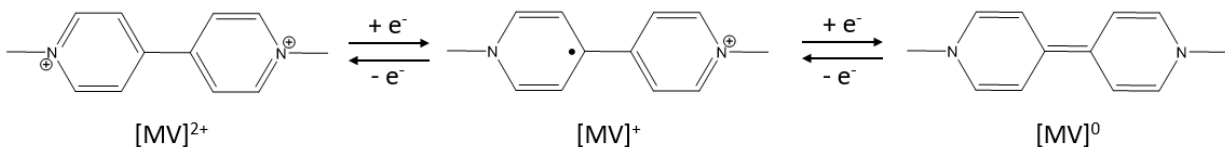
2.2.2. Electron acceptors

Sacrificial electron acceptors were used to oxidatively quenched the triplet state of the photosensitizer generating thereby a highly oxidizing species. The following examples are several typical electron acceptors that I used in photosystem studies by taking account the solvent effect and verifying the electron transfer using diverse techniques.

i) Methylviologen (MV^{2+})

Methylviologen (N,N'-dimethyl-4,4'-bipyridinium dichloride, the dication notated as MV^{2+}) is and widely used as a reversible electron-acceptor. In the electrochemical behavior of methylviologen, MV^{2+} reduce by a reversible one-electron reaction to a strongly colored blue radical cations ($\text{MV}^{\cdot+}$,

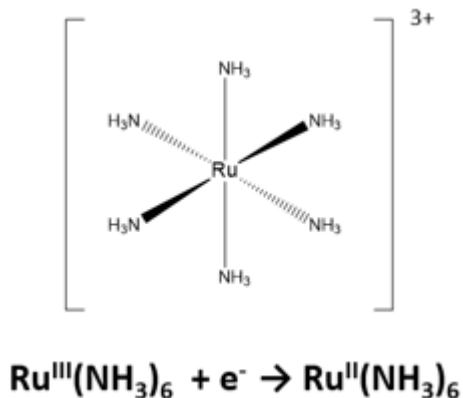
$\lambda_{\max} = 600 \text{ nm}$, $\epsilon = 14000 \text{ M}^{-1}\text{cm}^{-1}$) then it reduces further to the neutral, which is fully reduced form (MV⁰).^[90,91] (Scheme 1-1.) MV²⁺ has been widely used in photoinduced electron transfer studies.^[92]



Scheme 2-4 Accessible charge state of methylviologen.

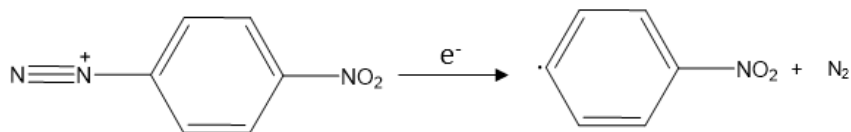
ii) Ruthenium Hexamine (RH³⁺), [Ru(NH₃)₆]³⁺

Ruthenium hexamine (RH³⁺), [Ru(NH₃)₆]Cl₃ is also using as an electron acceptor and it is useful to study transient absorption. In the visible region, RH does not present any marked absorption bands in the visible region in both its oxidized and reduced forms.^[93] As shown in Scheme 1-2, upon excitation of [Ru(bpy)₃]^{*2+} as chromophore, it reversibly accepts and an electron to generate [Ru(bpy)₃]³⁺.



Scheme 2-5 Chemical structure of [Ru(NH₃)₆]³⁺ (above) and the redox chemical equation (bottom).

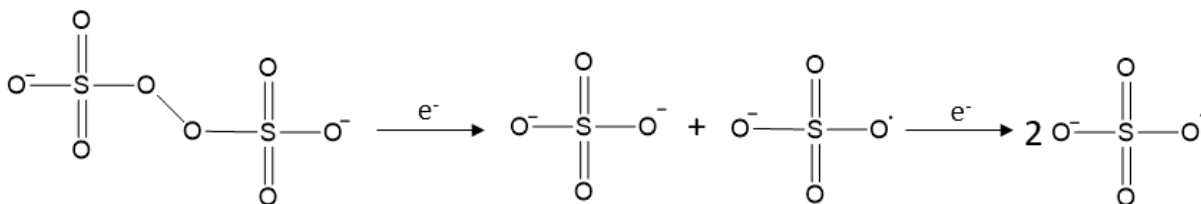
iii) 4-nitrobenzenediazonium tetrafluoroborate (NBD)



Scheme 2-6 Chemical structure and its reduced form of 4-nitrobenzenediazonium tetrafluoroborate.

The reduced form of diazonium (Dediazotation) leads to aryl radical and dinitrogen. The aryl radical is highly reactive and recently in photochemistry the transfer photo-induced charge to the diazonium that produce radical form has been studied.^[94] It is used as an irreversible electron acceptor. Indeed, upon accepting an electron from the excited state of the photosensitizer it forms a radical that ultimately degrades.

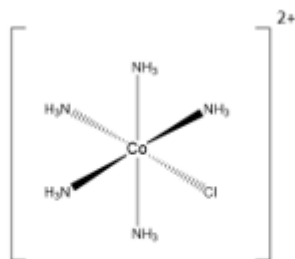
iv) Persulfate (Pers)



Scheme 2-7 Reduced form of persulfate.

Persulfate (Pers, $S_2O_8^{2-}$) is used as a sacrificial electron acceptor. It accepts a first electron to form the sulfate radical ($SO_4^{\cdot-}$). The latter is highly oxidizing and can act as an electron acceptor.^[95,96] It has been studied to be employed in promoting light-driven water oxidation system because as an irreversible electron acceptor, without the recombination or reverse electron transfer, it is useful to investigate the kinetic study of series steps in the catalytic process.^[18]

v) Chloropentamminecobalt chloride, $[\text{Co}^{\text{III}}(\text{NH}_3)_5\text{Cl}]^{2+}$



Scheme 2-8 Chemical structure of $[\text{Co}^{\text{III}}(\text{NH}_3)_5\text{Cl}]^{2+}$ (above) and the chemical reaction equation in presence of photosensitizer, $[\text{Ru}(\text{bpy})_3]^{2+}$ (bottom)

Chloropentamminecobalt chloride, $[\text{Co}^{\text{III}}(\text{NH}_3)_5\text{Cl}]^{2+}$ is well known as irreversible electron acceptor. Lehn et al., were the first to employ Co(III) complexes in water oxidation system.^[97] As shown by the equation, electron transfer to the Co^{III} complex is reduced to Co^{II} complex and it is much less stable than Co^{III} parent. Finally, it is converted to $[\text{Co}(\text{H}_2\text{O})_6]^{2+}$ cation which is an irreversible decomposition process (Scheme 2-8).^[97]

2.3. Characterizations of Cu^{II}OPBI

2.3.1. Cyclic Voltammetry (CV)

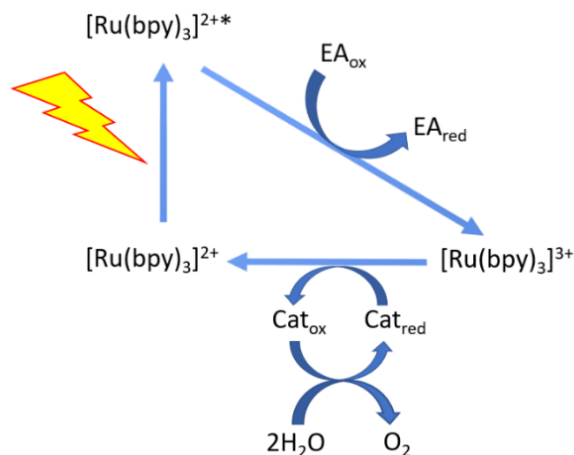


Figure 2-2 Three-component system for light-driven water oxidation consisting of a catalyst, $[\text{Ru}(\text{bpy})_3]^{2+}$ photosensitizer and sacrificial electron acceptor.

Before trying photocatalytic experiments with the Cu catalyst complex, it is useful to verify the potential needed for catalysis by electrochemical characterization. The light-driven water oxidation is based on the electron transfer processes occurring between photosensitizer, catalyst and electron acceptor. As shown in Fig. 2-2, $[\text{Ru}(\text{bpy})_3]^{2+}$ is brought into the excited state, $[\text{Ru}(\text{bpy})_3]^{2+*}$ after light. The excited state transfers an electron to the electron acceptor creating the strongly oxidizing state $[\text{Ru}(\text{bpy})_3]^{3+}$, which in turn oxidizes the catalyst. In this reaction sequence, the crucial point is the thermodynamic driving force for the different electron transfer reactions which should be negative for the reaction to occur spontaneously. That is, the oxidation potential of electron acceptor should be higher than the potential of excited state. On the other hand, the potential of the catalyst should be lower than the oxidation potential of $[\text{Ru}(\text{bpy})_3]^{3+}$.^[37–39] Therefore, it is important to determine the potential of the catalyst. Cyclic Voltammetry (CV) is the simplest tool to measure the potential of the compound. It is affected by electrolyte and solvent conditions. The solubility check depending on the solvent is necessary and the voltage range of electrochemical solvent window is an important characteristic to be considered. Fig. 2-3 is the influence factors such as electrolyte, solvent and nature of the working electrode on the potential window.^[98–100] Acetonitrile (ACN) is a typical organic solvent used to

investigate water oxidation catalysis which has large anodic potential limitation. Alternatively, aqueous buffer using different pH has been used in the electrocatalytic water oxidation process. In these experiments, we considered diverse factors including solubility and electrolyte potential limitations and finally, we performed experiments both in ACN and aqueous high pH phosphate buffer.

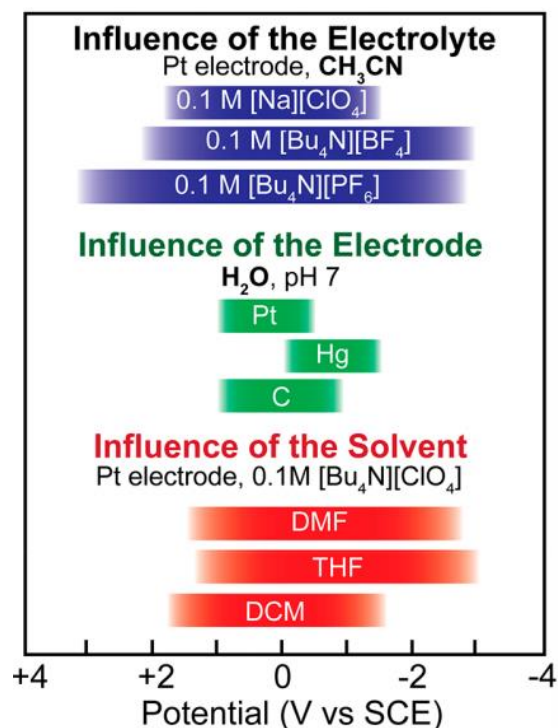


Figure 2-3 Electrochemical solvent windows as function of potential.^[100]

Fig. 2-4 is the CV of Cu^{II}OPBI in ACN using tetrabutylammonium hexafluorophosphate (TBAPF₆) as supporting electrolyte. The first peak potential around $E_{1/2} = -0.05$ V, corresponds to Cu^{II/III} and the further peaks belong to oxidation of the ligand.^[82] In the next, the electroactivity towards water as substrate was performed upon addition of small amount of water to the solution.

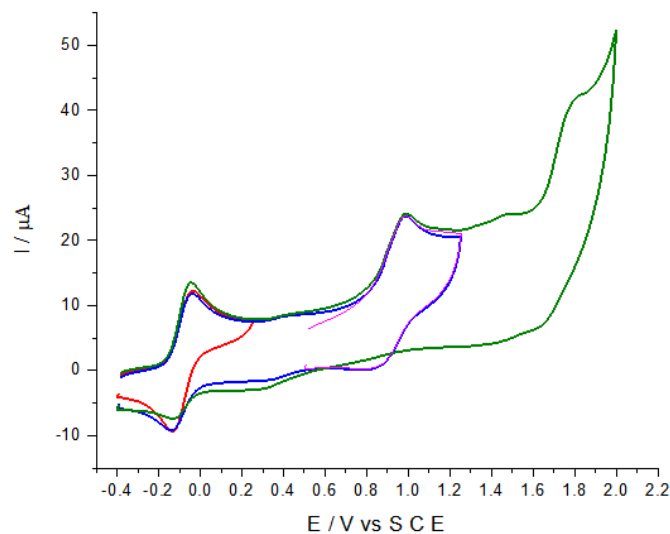


Figure 2-4 CV of 1 mM solutions of $\text{Cu}^{\text{II}}\text{OPBI}$ complex in ACN containing 0.1 M TBAPF_6 as supporting electrolyte. GCE (WE), Pt (CE), E / V vs. SCE. $v=100 \text{ mVs}^{-1}$

2.4. Electrochemical water oxidation

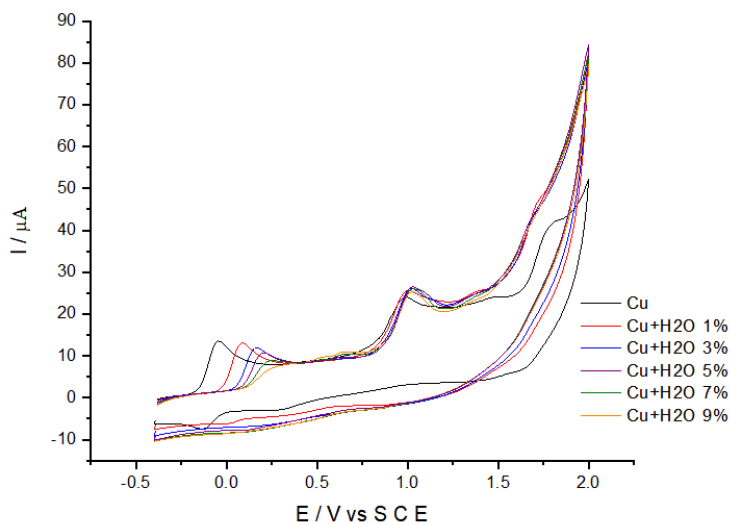


Figure 2-5 CV of 1 mM solutions of $\text{Cu}^{\text{II}}\text{OPBI}$ complex at different water concentration 1, 3, 5, 7 and 9 % in ACN containing 0.1 M TBAPF_6 as supporting electrolyte. GCE (WE), Pt (CE), E / V vs. SCE. $v=100 \text{ mVs}^{-1}$

Fig. 2-5 shows the CV of $\text{Cu}^{\text{II}}\text{OPBI}$ in presence of water. The concentration of water was increased from 1 % to 9 % which correspond to max. 4.95 M concentration based on Table 2-1. The $\text{Cu}^{\text{II/III}}$ peak shifts positive potential with decreasing current peak, which can be explained oxygen atoms

on the ligand might have hydrogen bonding by water molecules. Thus, the stability of $\text{Cu}^{\text{II/III}}$ with ligand decreases as increasing the water concentration.

Table 2-1 Converted % concentration to M concentration

%	1	2	3	4	5	6	7	8	9
H ₂ O (M)	0.55	1.10	1.65	2.20	2.75	3.30	3.85	4.40	4.95

The current peak increasing at potentials over 1.5 V vs. SCE that can be attributed to water oxidation process. However, upon increasing the water concentration we noticed that intensity of the observed current quickly reached a plateau. The results show that Cu^{II} OPBI has modest activity as electrochemical water oxidation catalyst in acetonitrile as solvent. Furthermore, the potential at which water oxidation occurred in this ACN organic solvent condition was around 1.5 V vs. SCE, which is not available to be oxidized by the oxidized photosensitizer ($[\text{Ru}(\text{bpy})_3]^{3+}$). In order to verify whether water oxidation occurs at lower potential in aqueous buffer at high pH, the CV was measured in high pH phosphate buffer as shown Fig. 2-6.^[55]

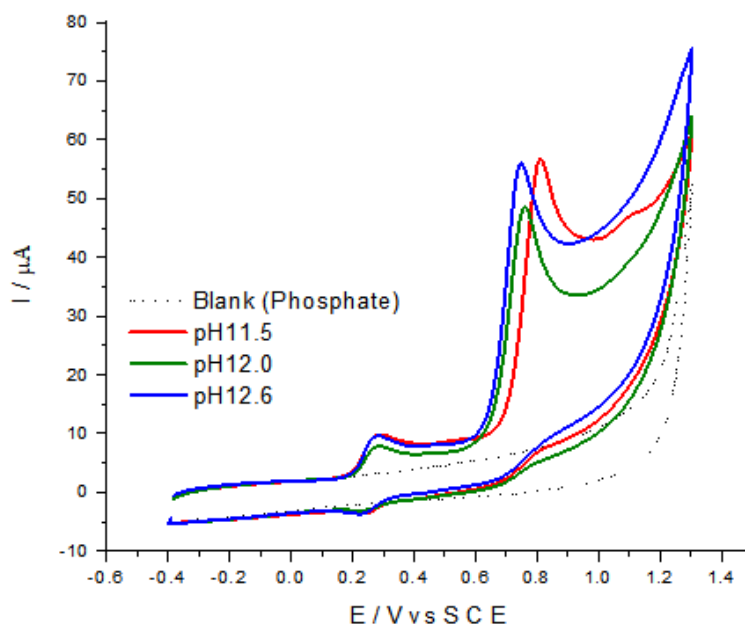


Figure 2-6 CV of 1 mM solutions of Cu^{II} OPBI complex in 0.1 M phosphate buffer pH 11.5, 12.0 and 12.5. GCE (WE), Pt (CE), E / V vs. SCE. $v=100 \text{ mVs}^{-1}$

In acidic buffer condition, the complex decomposed and the Cu^{II/III} oxidation peak potential changed. However, in high pH buffer, the complex was stable, and the CV was measured in high pH phosphate buffer in the pH range 11.5 - 12.6. The Cu^{II/III} potentials $E_{1/2} = 0.25$ V vs. SCE are pH-independent with electrochemically quasi-reversible wave. It is explained by the formation of a d⁸ Cu (III) square planar environment with low reorganizational energy, indicating both small differences in their respective geometries and low potential from the tetraanionic nature of the ligand.^[55] The second oxidation peak potentials were pH-dependent shifting towards lower values as function of pH, around 59 mV/pH. In addition, the amplitude of the second redox waves indicate a large electrocatalytic activity for water oxidation to dioxygen. The proposed ligand-based oxidation has been mentioned before in electrochemical point of view and the phenyl substituents support further as the strong inductive effects influence on the complexes. Theoretically, DFT calculations also confirm the ligand-based oxidation proposed.^[55,81,101]

A foot-of-the-wave analysis (FOWA) was used to get kinetic information of the catalytic process.^[102,103] Calculation of the rate constant k_{obs} was carried out based on the literature, as refer the rate-determining step (RDS) is the last electron-transfer step coupled to a chemical reaction.^[103] Fig. 2-7. shows the results of FOWA methodology, using LSV measured at different scan rates. from the average k_{cat} value, the value $k_{obs} = 2.9$ s⁻¹ was determined, which was independent of the scan rate and it was verified with the literature.^[55]

$$\frac{i_{cat}}{i_d} = \frac{n \cdot 2.24 \cdot \sqrt{\frac{R \cdot T}{F \cdot \nu}} \cdot k_{obs}}{1 + \exp\left[\frac{F}{R \cdot T}(E_{cat}^0 - E)\right]}$$

E_{cat}^0 : standard potential for the catalysis-initiating redox couple

i_{cat} : current intensity in the presence of substrate

i_d : current intensity in the absence of substrate

(approximate this current to the current associated with the $Cu^{III/II}$ couple)

n : number of electrons involved in the catalytic cycle (4 e- in water oxidation)

F : faraday constant

ν : scan rate

k_{obs} : defined as " $k_{cat} \cdot C_{O}A$ " ($C_{O}A$: concentration of substrate, 55.56 M for water)

R : $8.314 \text{ J} \cdot \text{mol}^{-1} \cdot \text{K}^{-1}$.

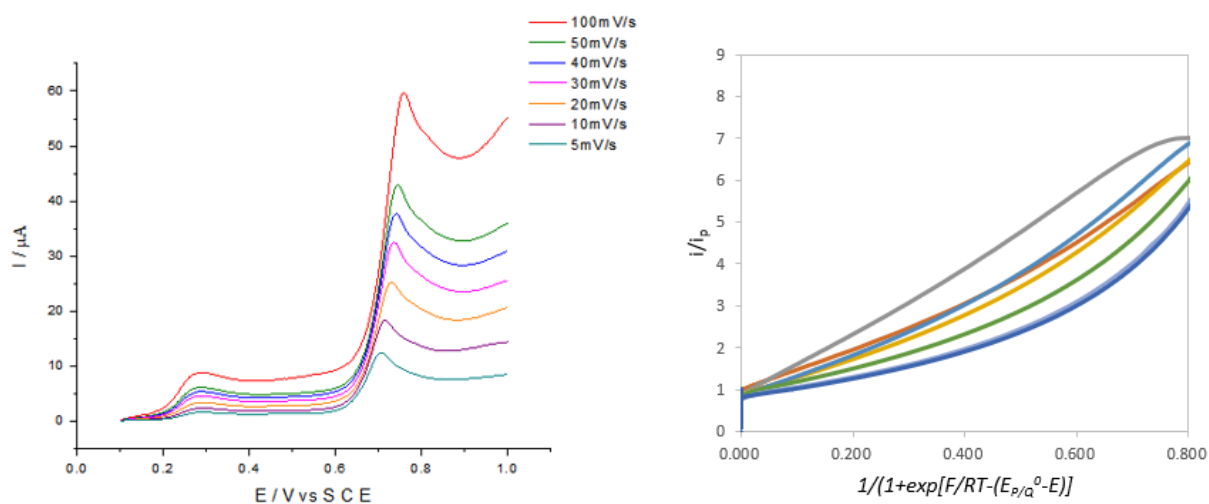


Figure 2-7 Linear Sweep Voltammeties (LSV) of 1.0 mM $Cu^{II}OPBI$ at 0.1 M Phosphate buffer pH 11.5, at several scan rates : 5, 10, 20, 30, 40, 50 and 100 mVs^{-1} , respectively (left). Foot of the wave analysis (FOWA) plotting i_{cat}/i_d vs. $1/(1+\exp[F/RT](E_{p/Q}-E))$ at each scan rate (right).

2.5. EPR spectro-electrochemical experiments

In collaboration with Prof. Abhishek Dey, we have been interested in investigating the mechanistic routes towards the formation of O₂ with a series of Cu^{II}OPBI complexes. The chemical structure of Cu^{II}OPBI compounds with different substituent are shown in Fig. 2-8. All three compounds exhibit two redox processes and are function of the electron donating and withdrawing nature of the -X substituents. An anodic shift was occurred with electron withdrawing -NO₂ group **2**, while a cathodic shift was observed with electron donating methyl (-Me) substituent complex **3**.

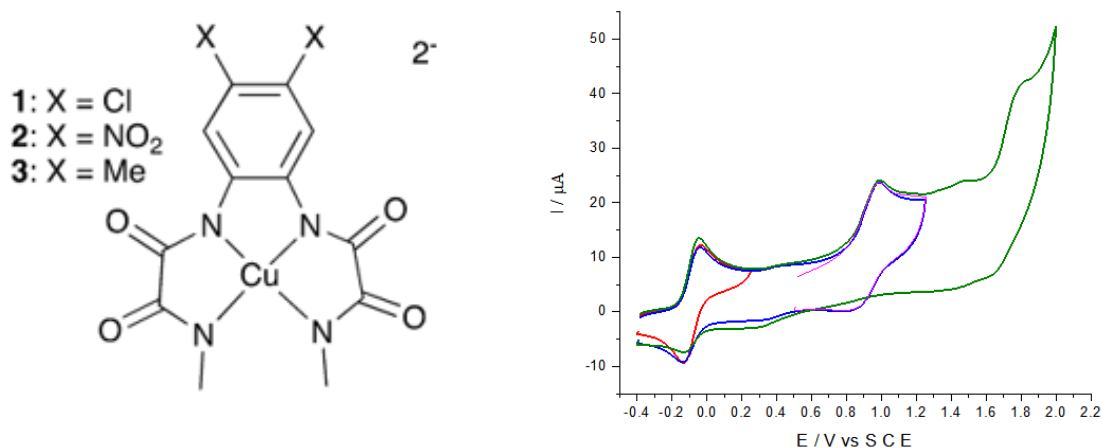


Figure 2-8 Chemical structure of the compounds. **1**, **2** and **3** contain -Cl, -NO₂ and -Me respectively in the position of X in the structure (left). CV of the compound **3** in ACN containing 0.1 M TBAPF₆ as supporting electrolyte. E / V vs. SCE. $v=100 \text{ mVs}^{-1}$ (right). Here, the catalyst present in 1 mM concentration. GCE, Pt and SCE are used as working, counter and reference electrode respectively.

EPR spectro-electrochemistry was performed to describe the locus of the oxidation processes under our experimental conditions. For the monoxidized forms of **1** and **3**, the ESR spectra show the presence of both Cu (II) and a ligand based radical, that can be best formulated as a [Cu²⁺L^{3•}] state. Interestingly, the intensity of the radical signal decreases upon electrolysis after the second oxidation wave at 1.2 V while the signals of Cu²⁺ are maintained intact (Fig. 2-9, left). The loss of intensity of the radical signal reflects the formation of a di-radical species from the Cu (II)- mono-radical species where the two radicals are anti-ferromagnetically coupled to each other. These parameters were almost unaffected for the mono-oxidized forms of **1** and **3** supporting the fact that the coordination scheme around the metal center is unaltered (Table 2-2). In contrast,

compound **2** forms solvent bound mono-radical when electrochemically oxidized at 0.9V (Fig. 2-9, right). This was evidenced by a shift of the $A_{||}$ (Cu^{2+}) value from 206 gauss (with a $g_{||} = 2.14$) in the initial copper (II) state to ~ 228 gauss (with a $g_{||} = 2.11$) in the ligand mono-radical state (Table 2-2). The second ligand based oxidation did not affect the Cu^{2+} signals and resulted in the loss of the ligand radical signal.

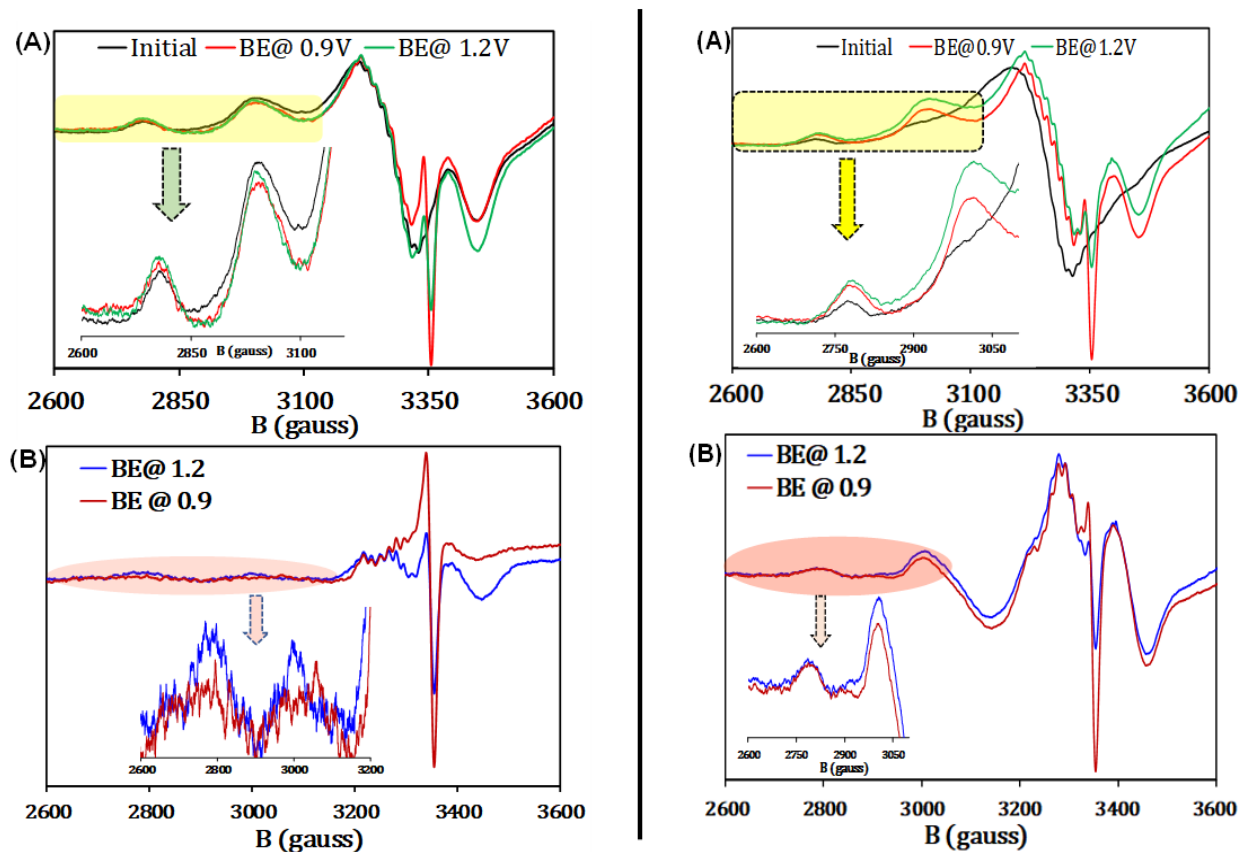


Figure 2-9 (A) ESR spectra of compound 1 (left) and 2 (right) in ACN having 100 mM TBAP (black- initial, red- after controlled potential electrolysis at 0.9 V and light green- after control potential electrolysis at 1.2 V). (B) ESR difference spectra (difference of the samples after respective oxidation from the initial without bulk electrolysis) of the same.

The catalytic oxygen evolution by compound **1** was investigated in acetonitrile by adding different amounts of an organic base (tetra butyl ammonium hydroxide, TBAOH) and the electro-catalytic process was observed (Fig. 2-10). With the central goal to capture the electronic signatures of the reactive intermediates under our homogeneous experimental conditions and furthermore to decrypt the catalytic species responsible for the rate determining steps, we monitored the control potential electrolysis the catalysts at two different oxidizing potentials (0.9 V and 1.2 V vs. Ag/AgCl) using the ESR spectroscopy.

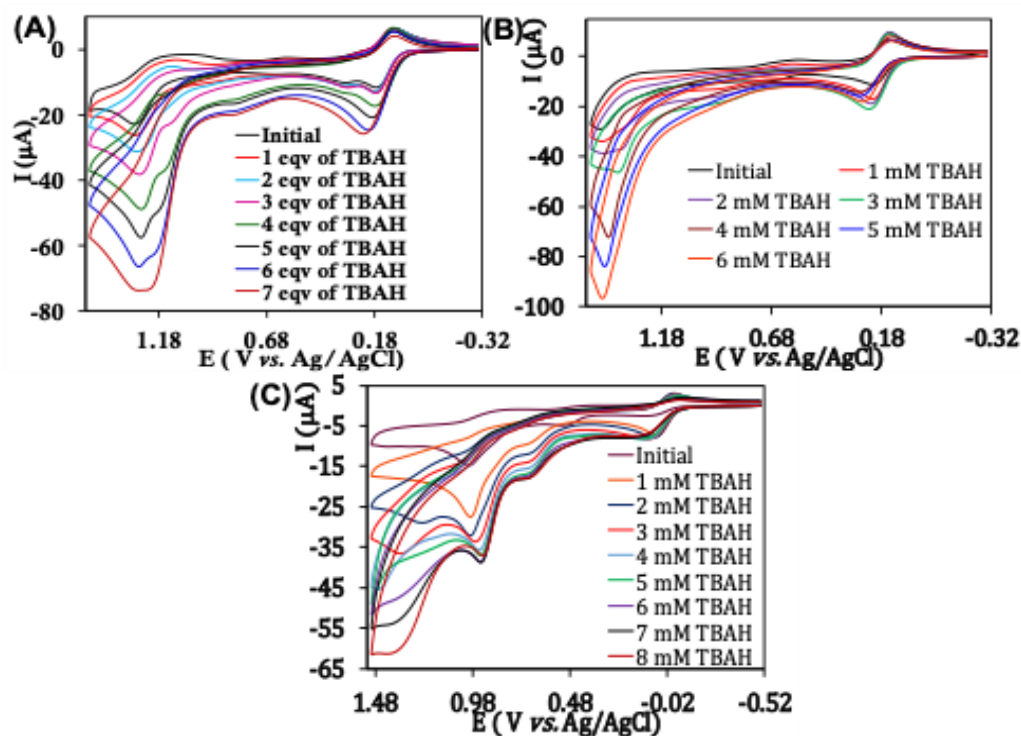


Figure 2-10 : Cyclic voltammograms of (A) **1**, (B) **2** and (C) **3** (1 mM in acetonitrile containing 100 mM TBAP as electrolyte showing the homogeneous catalytic oxygen evolution with increasing amounts of TBAH). Glassy carbon (GC), platinum and a sealed aqueous Ag/AgCl (saturated KCl) are used as working, counter and reference electrode, respectively.

Indeed, as we have seen above ESR provides a clear picture of the electronic states of the oxidized copper species together with the coordination scheme at the copper center. A common observation for the follow up of the doubly oxidized solution was the persistent observation of a copper(II) signal (Fig. 2-11). The EPR characteristics for compound **1** after 0.9 V and 1.2 V electrolysis indicate that the signals from the Cu^{2+} center are altered from the initial state with $g_{\parallel} = 2.11$ and $A_{\parallel}(\text{Cu}^{2+}) = 230$ gauss to $g_{\parallel} = 2.13$ and $A_{\parallel}(\text{Cu}^{2+}) = 220$ gauss (Fig. 2-11 and Table 2-2). There is no marked difference between the 0.9 V data (non-catalytic) and 1.2 V data (catalytic) providing support that a $\text{Cu}^{2+}(\text{OH})$ -ligand mono-radical species is accumulated under catalytic steady state. Hence, these electronic snapshots, provide an ECEC mechanistic scenario for **1**, where after the first the oxidation (E, generation of the ligand radical in the ESR), a hydroxide binds to the Cu (II)-ligand mono-radical, (C, change in $A_{\parallel}(\text{Cu}^{2+})$ and g_{\parallel} values) then a 2nd oxidation

to a Cu (II)-ligand di-radical state leading to the formation of the O-O bond like with a concerted attack of an OH⁻.

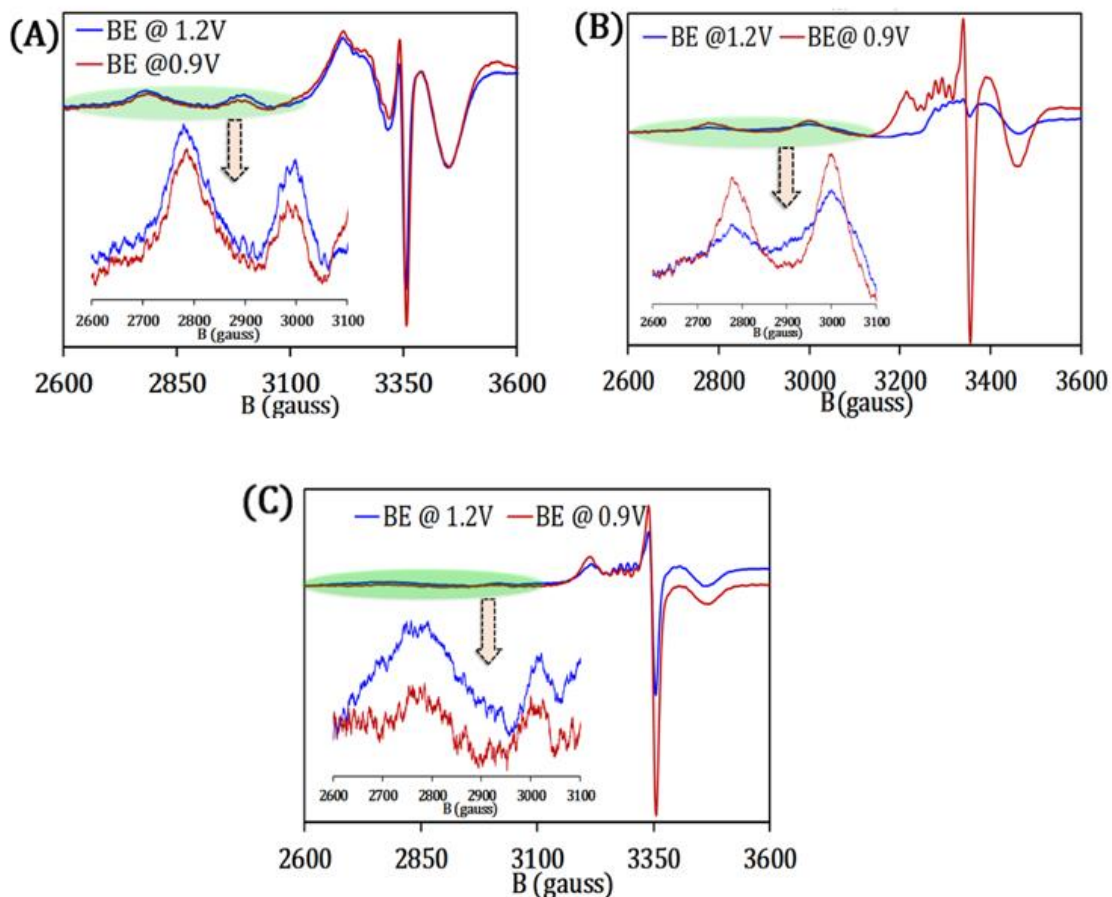


Figure 2-11 ESR spectrum (difference spectrum from initial with 7 mM TBAOH) of (A) compound 1, (B) compound 2, (C) compound 3 in presence of 7 mM TBAOH after bulk electrolysis has been done in two different potential (0.9 V and 1.2 V) using Hg-pool electrode as working electrode, sealed Ag/AgCl (aqueous, saturated KCl) and Pt electrode as reference and counter electrode respectively

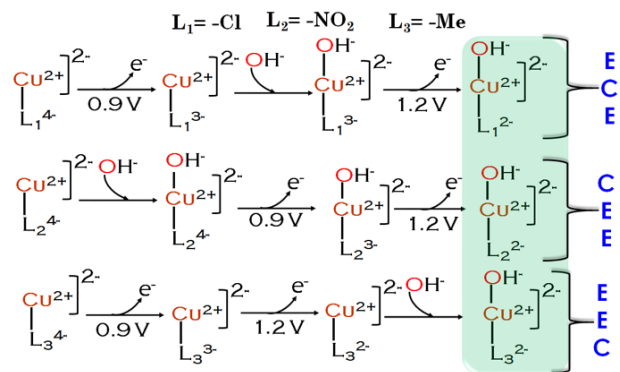
In the case of **2**, an initial C step occurs with the binding of OH⁻ at the resting Cu (II) state as detected by the shift of the g values from 2.14 to 2.12 upon addition of TBAH in the acetonitrile solution (Table 2-2). The two consecutive oxidations (EE) matched with the formation mono-radical and di-radical at 0.9 V and 1.2 V respectively. The consecutive hydroxide attack on the hydroxide bound di-radical concludes to a CEEC mechanism as evidenced by the accumulation of the Cu (II)(OH)-ligand di-radical state under steady state.

Note that, any variation in the Cu (II) ligation (eg.-OOH) could have resulted in the shift of its ESR signal. Two electrochemical oxidation sequences proceed for compound **3** forming the di-radical where upon hydroxide ion bound to the resultant Cu (II)- ligand di-radical as detected by a shift in the g_{II} and A_{II} (Cu^{2+}) values. (Fig. 2-11, (C)) and Table 2-2). The O-O bond then completes an EECC mechanism. The in-situ spectroelectrochemical investigations reveal that the mechanism can vary substantially depending on the electronic structure of the ligand. The strong electron withdrawing $-NO_2$ substituents, entail the substrate $-OH-$ binding in the resting state. The $-Cl$ substituents, a lesser electron withdrawing group, direct the substrate $-OH-$ to bind in the Cu (II)-ligand mono-radical species while the electron donating $-Me$ substituents allow the substrate binding only after two consecutive ligand oxidations.

Table 2-2 A_{II} and g_{II} values of the compounds in the absence and presence of TBAH and in initial and under catalytic conditions.

Species	Compound 1				Compound 2				Compound 3			
	Without TBAOH		With TBAOH		Without TBAOH		With TBAOH		Without TBAOH		With TBAOH	
	A_{II}	g_{II}	A_{II}	g_{II}	A_{II}	g_{II}	A_{II}	g_{II}	A_{II}	g_{II}	A_{II}	g_{II}
Initial	223	2.12	230	2.11	206	2.14	226	2.12	219	2.13	216	2.13
BE@0.9V	227	2.12	220	2.13	227	2.11	222	2.12	221	2.12	228	2.12
BE@1.2V	227	2.12	219	2.13	230	2.11	226	2.12	220	2.12	235	2.11

The mechanism of water oxidation in organic medium is investigated using spectro-electrochemistry. The results show that the catalytic species involved in water oxidation are $Cu^{2+}L^{2-}$ ligand-diradical species. Furthermore, the mechanism shifts from CEEC to ECEC to EECC as the substitution on the phenyl ring are made more electron donating (Scheme 2-9).



Scheme 2-9 Schematic representation of the formation of the hydroxide bound Cu(II) di-radical (responsible for water oxidation by the above-mentioned complexes, marked by green area).

2.6. Other Copper complex, Cu^{II}OBBZ

Another approach in terms of catalyst design was tried by using oxamido bis(benzoate), OBBZ ligand. The idea here was to investigate on tetra-anionic ligands again. We added a carboxylate group on the ligand and the target was to investigate how the chemical functions in the coordination sphere of copper would modulate the reactivity pattern of the copper complexes.

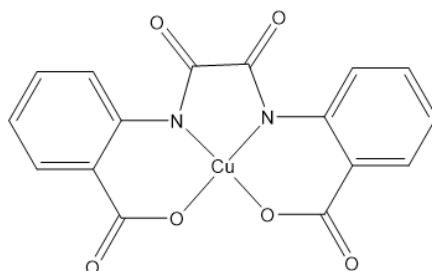


Figure 2-12 Chemical structure of copper complex : oxamido bis(*N,N'*-benzoate) Cu(II), Cu^{II}OBBZ

Lloret and co-workers have studied the effect of electron donating or electron-withdrawing substituents on the [Cu(OBBZ)]- with steric effects. In addition, the influence of solvent (protic or aprotic) concerning the stability of amido-carboxylato copper (III) complexes has been investigated.^[86]

However, no other studies of Cu^{II}OBBZ catalyst for water oxidation have been reported till now. We were assuming that the surrounding which consists of nitrogens and oxygens may have a role in water oxidation catalysis. In this part, we focus on the electrochemical properties of the compound and further studies for photocatalytic activation. The fundamental properties such as solubility of the compound , pH effect and solvent potential wall were taken into account for the experiments which were performed both in ACN and aqueous high pH phosphate buffer, as was shown before for Cu^{II}OPBI.

2.6.1. CV of Cu^{II}OBBZ

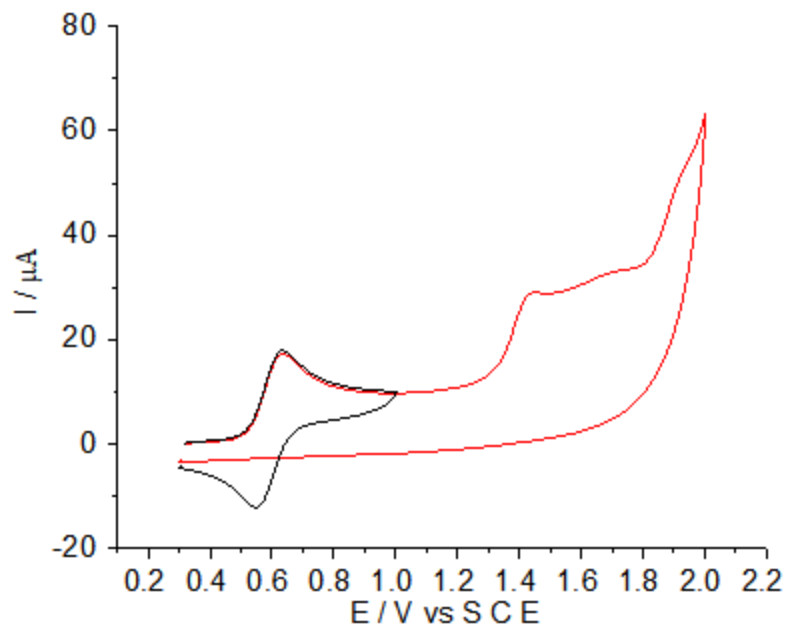


Figure 2-13 CV of 1 mM solutions of Cu^{II}OBBZ complex in ACN containing 0.1 M TBAPF₆ as supporting electrolyte. GCE (WE), Pt (CE), E / V vs. SCE. $\nu=100 \text{ mVs}^{-1}$

The electrochemical behavior of Cu^{II}OBBZ was investigated by CV in ACN using tetrabutylammonium hexafluorophosphate (TBAPF₆) as supporting electrolyte (Fig. 2-13). The first reversible oxidation occurs around $E_{1/2} = 0.62 \text{ V vs. SCE}$ and it corresponds to a Cu^{II/III} couple. The further oxidation peak, $E_{1/2} = 1.4 \text{ V vs. SCE}$ was explored for water oxidation. At low potential values of copper (II) complex oxidation peak, Cu (III) species is explained due to the high basicity of the deprotonated amide nitrogen and the oxygen atoms from the carboxylate groups in the chemical structure.^[86] Electron donating group substituent on the phenyl ring provides donor character which influence the oxidation potential. Thus, the amide nitrogen and carboxylate oxygen atoms in the structure lead to lower oxidation potentials.^[86]

2.6.2. Electrochemical water oxidation by Cu^{II}OBBZ

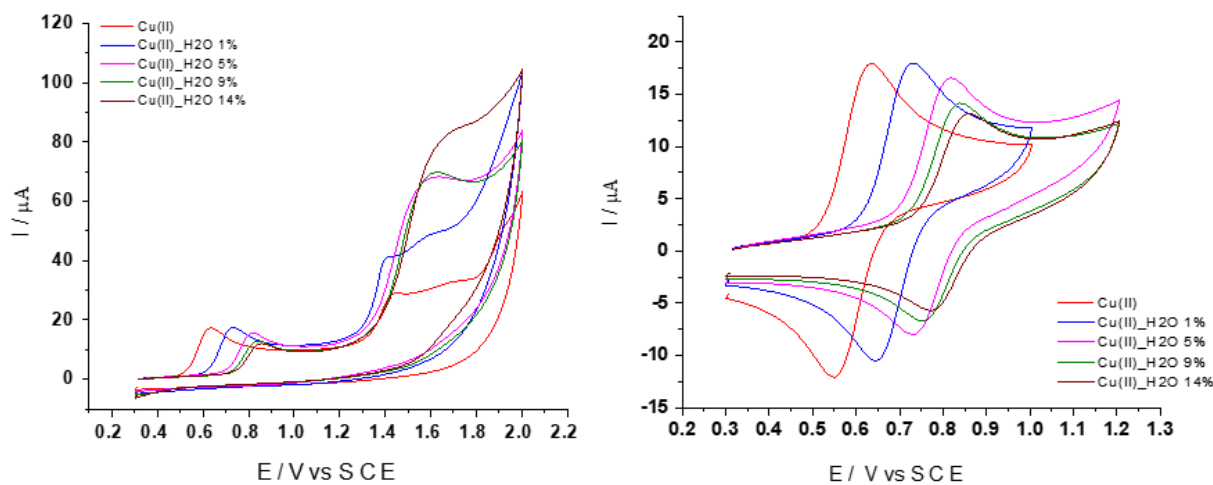


Figure 2-14 CV of 1 mM solutions of Cu^{II}OBBZ (TMA)₂ complexes adding water concentration 1 % to 14 % in ACN containing 0.1 M TBAPF₆ as supporting electrolyte. Potential range [0.3, 2.0 V] (right) and potential range [0.3, 1.2 V] (left). GCE (WE), Pt (CE), E / V vs. SCE. v=100 mVs⁻¹.

The second oxidation peak started at the potential over 1.4 V and the current kept increasing with the concentration of water. It indicates that the catalytic wave could indeed indicate water oxidation since the addition of water led to an oxidation process with pronounced wave.

By changing the electrolyte condition, 0.1 M phosphate buffer, in this case, the electrochemical water oxidation was studied in different pH conditions. The pH conditions were restrained to high pH range since at low pH (< pH 8) the compound precipitated (Fig. 2-15). This had been investigated in previous research which showed that at pH > 9 the complex is stable but lower pH causes ligand protonation which renders the complex highly insoluble in aqueous solution.^[86] Thus, the CV was performed in the high pH range 9 < pH < 12 (Fig. 2-16). Under basic conditions, at pH 9, a catalytic wave was observed at applied potentials above 1.2 V. This cannot be attributed to deposition on the electrode as the electrode was polished after each CV scan. However, unlike in ACN, oxidation peak was not reversible which could be explained with a fast chemical reaction being coupled to the electrochemical process.^[86]

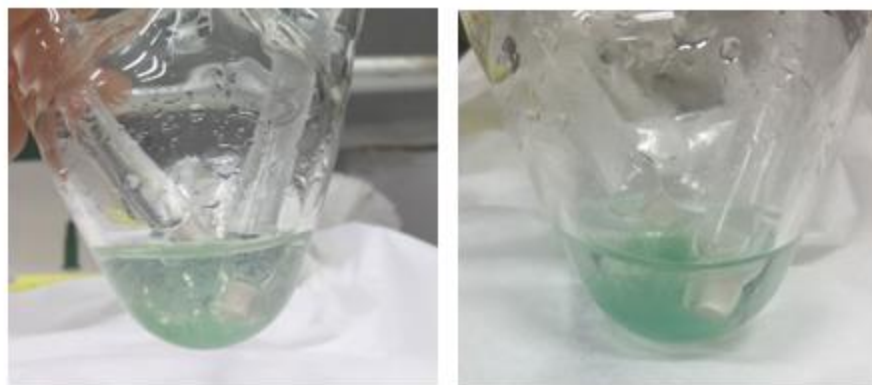


Figure 2-15 Decomposition and precipitation in low pH of the solution, pH < 8.

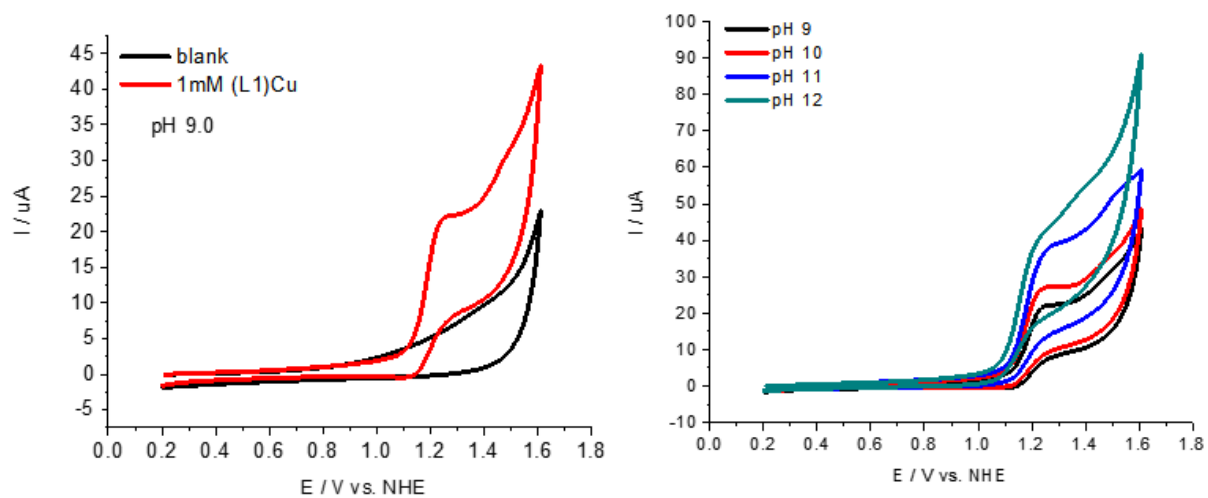


Figure 2-16 CV of $\text{Cu}^{\text{II}}\text{OBBZ}$ in 0.1 M phosphate buffer at pH 9, 10, 11 and 12. GCE (WE), Pt (CE), E / V vs. SCE. $v=100 \text{ mVs}^{-1}$.

Fig. 2-17 shows CV of plot of the current at $E = 1.377 \text{ V}$ in dependence of the pH 9 - 12.5, which corresponds the Fig. 2-16. By subtracting current values between blank and $\text{Cu}^{\text{II}}\text{OBBZ}$, the potential was determined which corresponding to the maximum current value at pH 9. A plot of the catalytic current vs. solution pH indicates a current increase over the whole basic conditions.

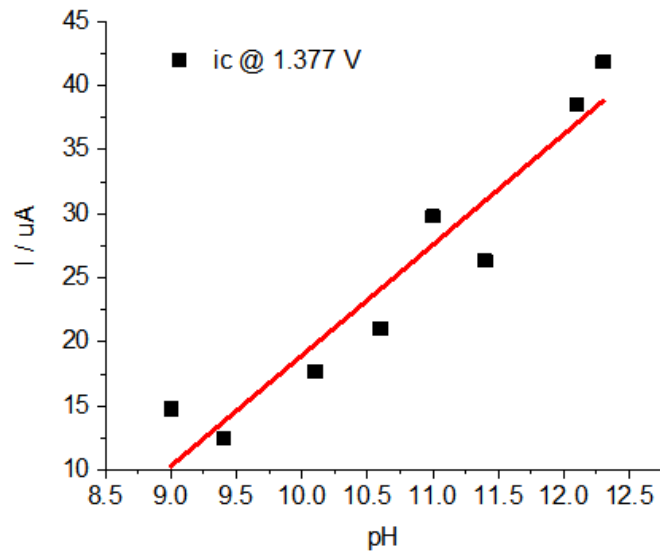


Figure 2-17. CV of Plot of the current i_{pc} at $E = 1.377$ V in dependence of the pH. (The data from Fig. 2-16.).

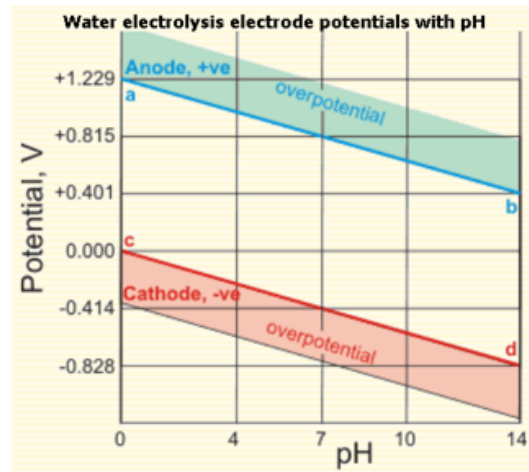
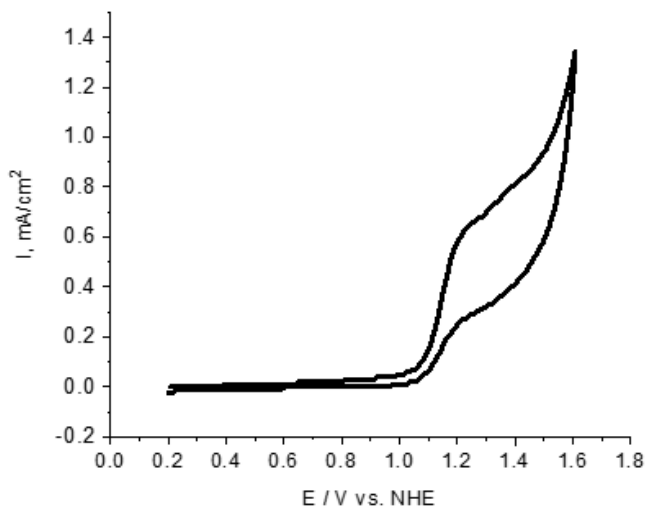


Figure 2-18 Overpotential at pH 12.3 ($\eta = 1.528 - 0.51 = 1.018$ V) (left), water electrolysis electrode potentials with pH (right).

The overpotential at pH 12.3 was calculated to be 1.018 V, for a current density of 1 mAcm^{-2} (Fig. 2-18). This overpotential was not pronounced value among the Cu complexes which have been studied in terms of overpotential. (Table 1.1)

In order to distinguish the separated potential, $E_{1/2}$ values for the redox processes studied were estimated from the potential at the I_{max} in DPV measurements. As shown in Fig. 2-19, DPV gives the information that two clear peak potentials exist at 1.2 V and 1.35 V, respectively. The corresponding plot of the potential of the inflection points of the DPV data at different pH is shown in Fig. 2-19 (right). The first peak potentials in different pH were stable and pH-independent which indicate one electron involved in this oxidation, $\text{Cu}^{\text{II}} \rightarrow \text{Cu}^{\text{III}} + e^-$. On the other hands, the peak potential of the second oxidation process is pH dependent and it shifts by 59 mV/pH above pH 9, which is characteristic for a $1e^-/1H^+$ coupled redox process according to the Nernst equation.^[50]

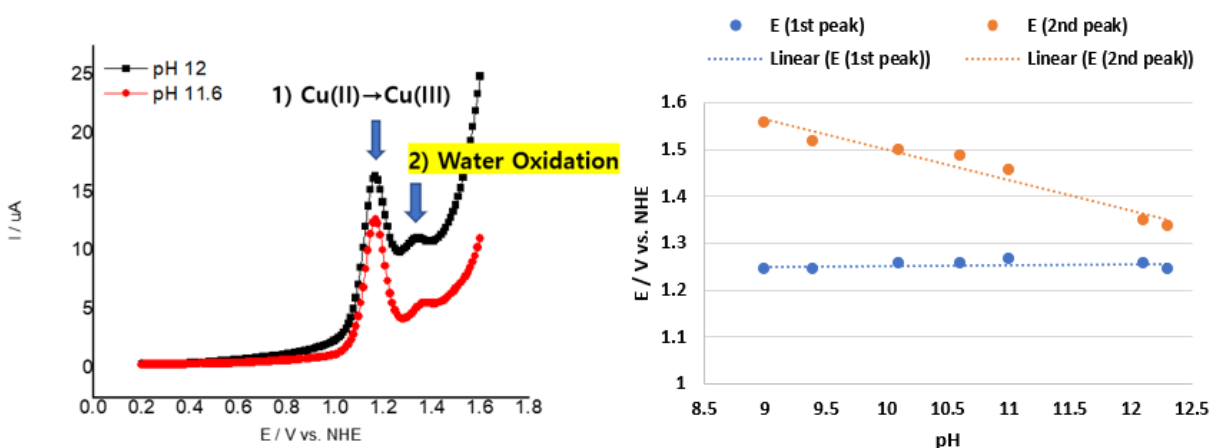


Figure 2-19 DPV data of $\text{Cu}^{\text{II}}\text{OBBZ}$ in 0.1M phosphate buffer in different pH (left), Plot of the potential of the 1st and 2nd inflection point of the DPV at different pH. (right)

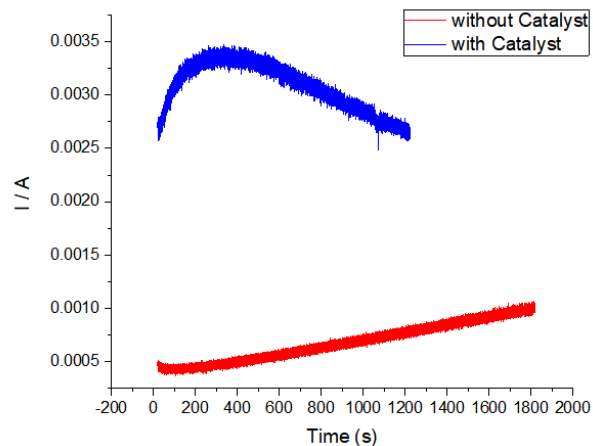


Figure 2-20 Electrolysis of 1.0 mM Cu^IOBBZ, Time (s) vs. Current (A). Carbon plate (WE), Pt (CE) and SCE (RE), respectively.

Controlled potential electrolysis experiment (CPE) at an applied potential of 1.4 V was performed using carbon plate working electrode at pH 11.3. However, as shown in Fig. 2-20, the current decreased as function of time. In addition, deposition on the working electrode was observed visually. These phenomena give a reasonable evidence that the catalyst is not stable to function as homogeneous catalyst during catalysis.

2.7. Photochemical water oxidation

2.7.1. Photophysical studies between $[\text{Ru}(\text{bpy})_3]^{2+}$ and Copper complex

We have examined issue relating to the behavior of the $\text{Cu}^{\text{II}}\text{OPBI}$ complex by laser flash photolysis. The effect of ion pairing between $[\text{Ru}(\text{bpy})_3]^{2+}$ sensitizer and the copper complex, $\text{Cu}^{\text{II}}\text{OPBI}$ was investigated to go toward the photocatalytic events. Emission kinetics at 610 nm of the mixture in different concentration of $\text{Cu}^{\text{II}}\text{OPBI}$ are shown in Fig. 2-21. Without an electron acceptor, the quenching of excited state ($[\text{Ru}(\text{bpy})_3]^{2+*}$) occurred in presence of the copper(II) complex. The quenching takes place in ion-paired species, which is not an oxidative quenching as the yield of Ru (I) is much lower than 2 % (Fig. 2-22). Note that, the mixture had no reaction in the dark.

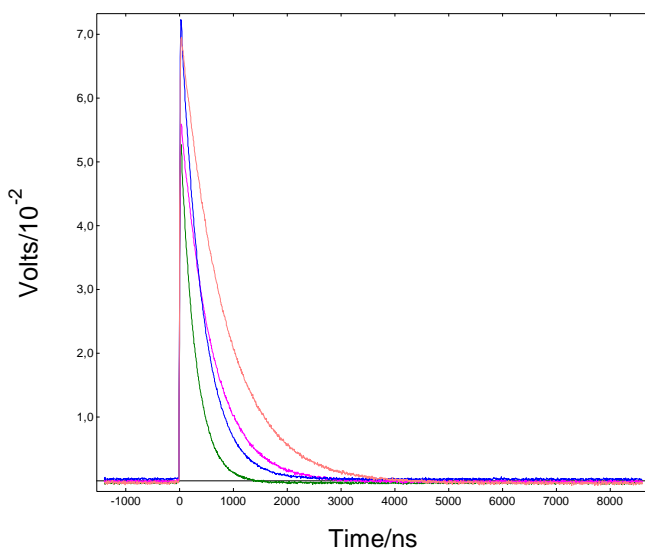
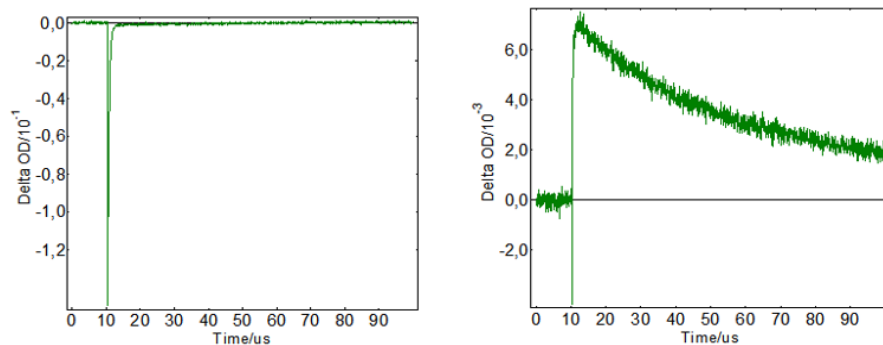


Figure 2-21 Emission kinetics at 610nm. 35uM of $[\text{Ru}(\text{bpy})_3]^{2+}$ with 10 (orange), 20 (pink), 30 (blue), 60 (green) uM of $\text{Cu}^{\text{II}}\text{OPBI}$ in ACN, degas conditions.; The life time get decreased as increasing the concentration of $\text{Cu}^{\text{II}}\text{OPBI}$.(800, 572, 405 and 277 ns, respectively.)



[Yield Calculation]

$$[\text{Ru}(\text{bpy})_3]^{2+} = 0.16 / 12000 = 13 \text{ } \mu\text{M}$$

$$\text{Ru (I)} = 0.007 / 20000 = 0.35 \text{ } \mu\text{M}$$

$$\text{Yield : } 0.35 \text{ } \mu\text{M} / 13 \text{ } \mu\text{M} \times 100 (\%) = 2\%$$

Figure 2-22 Absorption kinetics at 450 nm (left) and 510 nm (right) ; 35 μM of $[\text{Ru}(\text{bpy})_3]^{2+}$ with 30 μM of $\text{Cu}^{\text{II}}\text{OPBI}$. The yield of Ru (I) from $[\text{Ru}(\text{bpy})_3]^{2+}$ was calculate based on the value on the peak.

These results were already interesting to investigate further the photophysical events in presence of an electron acceptor. Interestingly, when I add 10 mM of methyl viologen as a reversible electron acceptor in the mixture, I notice that the mixture turns blue, a colour typical of the methylviologen radical. Fig. 2-23 shows absorption kinetics of the mixture in the presence of methyl viologen at 450 nm. The blue spectra, which consist of 35 μM of $[\text{Ru}(\text{bpy})_3]^{2+}$ with 20 μM of $\text{Cu}^{\text{II}}\text{OPBI}$ in the presence of 10 mM of methyl viologen. As we can see, we recover the band at 450 nm very rapidly with the formation of a small absorption peak. A plausible route for this light induced electron transfer process is represented in Fig. 2-23.

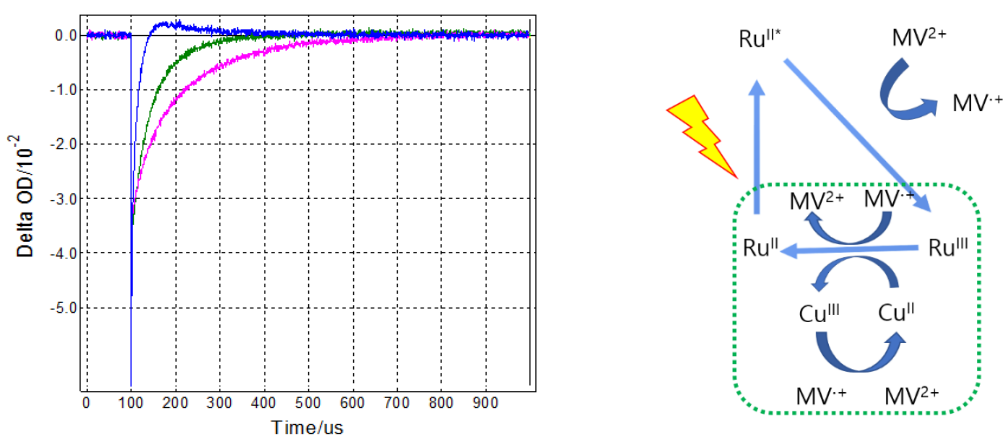


Figure 2-23 Absorption kinetics at 450 nm (left) and the possible scheme (right). 35 μM of $[\text{Ru}(\text{bpy})_3]^{2+}$ with 10 (green) and 20 (blue) μM of $\text{Cu}^{\text{II}}\text{OPBI}$ in the presence of 10 mM of methyl viologen.

2.7.2. Oxygen measurement by Clark Electrode

Based on the principle of photocatalysis presented in the previous part '2.3.1' and Fig. 2-2., a potential for oxidation of $\text{Cu}^{\text{II}}\text{OPBI}$ in 0.1 M phosphate buffer, of $> 0.8 \text{ V}$ vs. SCE was required which is compatible with using $[\text{Ru}(\text{bpy})_3]^{2+}$ as photosensitizer. The Clark Electrode as shown in the Fig. 2-24 was used to detect the formation if any of O_2 .



Figure 2-24 Experimental set-up : Clark Electrode before (left) and under illuminating (right)

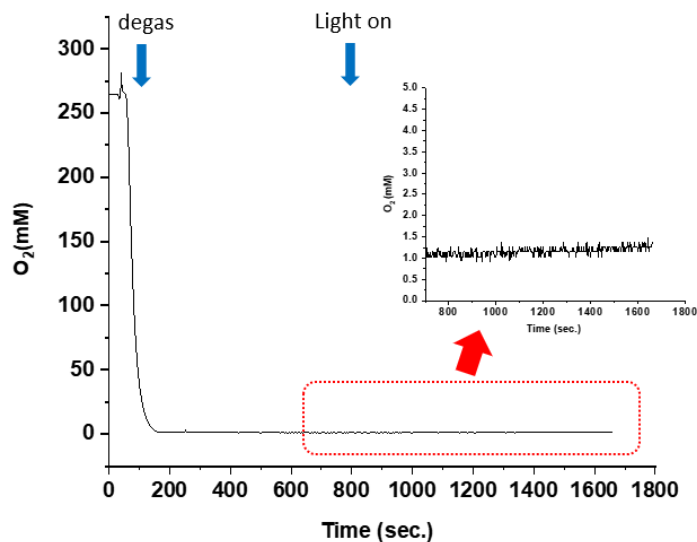


Figure 2-25 Oxygen measurement by Clark Electrode. $200 \mu\text{M}$ of $[\text{Ru}(\text{bpy})_3]^{2+}$ as photosensitizer, 10 mM NBD as electron acceptor and $100 \mu\text{M}$ of catalyst ($\text{Cu}^{\text{II}}\text{OPBI}$) in 0.1 M phosphate buffer pH 11.5. At the beginning, the solution was degassed until it reaches 'zero (0)' oxygen concentration then observes keeping stable for 5 min. then turn on the light at the time point '800 sec.'

For the different combinations of photosensitizers and electron acceptors and copper complexes no oxygen evolution was detected under irradiation. The summary of the results is gathered in Table 2-3 and Fig. 2-25 .

Table 2-3 The summary of Oxygen measurement by Clark Electrode, using Cu^{II}OPBI

Catalyst	Cu ^{II} OPBI			
Photosensitizer	[Ru(bpy) ₃] ²⁺	[Ru(bpy) ₃] ²⁺	[Ru(bpy) ₂ (4-4'-(PO ₃ H ₂) ₂ bpy)]	[Ru(bpy) ₂ (4-4'-(PO ₃ H ₂) ₂ bpy)]
Electron Acceptor	NBD	[Co ^{III} (NH ₃) ₅ Cl] ²⁺	[Co ^{III} (NH ₃) ₅ Cl] ²⁺	Pers
Electrolyte	0.1 M Phosphate buffer, pH 11.5			
Results	No evolution			

Another trial of photocatalysis using Cu^{II}OBBZ was performed in the diverse combinations of photosensitizers and electron acceptors. However, here too no oxygen evolution was evidenced. The summary of results is shown in Table 2-4.

Table 2-4 The summary of Oxygen measurement by Clark Electrode, using Cu^{II}OBBZ

Catalyst	Cu ^{II} OBBZ		
Photosensitizer	[Ru(bpy) ₃] ²⁺	[Ru(bpz) ₃] ²⁺	[Ru(bpy) ₂ (4-4'-(PO ₃ H ₂) ₂ bpy)]
Electron Acceptor	Pers	NBD	Pers
Electrolyte	0.1 M Phosphate buffer, pH 11.5		
Results	No evolution		

Although these two copper complexes didn't succeed to produce oxygen, surprisingly, we found that the color of mixture changed in the dark. The mixture between [Ru(bpy)₃]²⁺ sensitizer and the copper complex or between [Ru(bpy)₃]²⁺ and MV²⁺ nothing happened in the dark. We discovered that the color of mixture of the electron acceptor (methylviologen) and the copper complex changed to a blue color, typical to the formation of methylviologen radical. Such an intriguing observation will constitute the study of the next chapter.

2.8. Conclusions & Perspectives

In conclusion, we have observed the electrocatalytic water oxidation with a Cu^{II}OPBI in both organic solvent and aqueous medium. Other copper complex, Cu^{II}OBBZ was also studied for the electrochemical water oxidation catalysis. However, due to the deposition on the electrode during electrolysis, it couldn't be proved as homogeneous catalyst.

Concerning the Cu^{II}OPBI, a copper (II) bis-oxamidate complex having different electron donating and withdrawing substituent was investigated. The study of OER and mechanism of water oxidation in organic medium was studied using spectro-electrochemistry in collaboration with Prof. Abhishek Dey. The results show that the catalytic species involved in water oxidation are Cu²⁺L²⁻ ligand-diradical species. Furthermore, the mechanism shifts from CEEC to ECEC to EECC as the substitution on the phenyl ring are made more electron donating.

Furthermore, it was investigated the photochemical water oxidation catalysis by using Ru-based photosensitizers and diverse electron acceptors using laser flash photolysis and Clark electrode. Even though the oxygen evolution was not detected, we discovered that the color of mixture of the electron acceptor and the copper complex changed to a blue color, typical to the formation of methyl viologen radical. This will be carried out in the **Chapter 3**, 'ion pair formation'.

Chapter III.

Ion Pair Formation

3. Ion pair formation

In the previous Chapter 2, we discussed about Cu complexes as electrocatalyst. We found something very intriguing in the process of light activation of the molecular complex with a photosensitizer and an electron relay. First, the effect of ion pairing between $[Ru(bpy)_3]^{2+}$ sensitizer and the $[Cu^{II}OPBI]^{2-}$ complex was investigated without an electron acceptor. The quenching of excited state ($[Ru(bpy)_3]^{2+}$) occurred by the Cu complex while no electron transfer reaction took place in the dark. The addition of a reversible electron acceptor such as methylviologen (MV^{2+}) in the previous mixture led to a drastic color change to a blue solution in the dark. No perceptible color change was observed for the mixture between $[Ru(bpy)_3]^{2+}$ sensitizer and the Cu complex or between $[Ru(bpy)_3]^{2+}$ and MV^{2+} . This color change was reproduced when the Cu complex was mixed with methylviologen (MV^{2+}) in ACN, under anaerobic conditions. In this chapter, we investigated the ion pair formation phenomenon between the oppositely double charged species of Cu complex catalyst and an electron acceptor. The electron transfer pathway is the main target of this study.*

3.1. Introduction

The presence of sensitizer, electron donor (or acceptor) and catalyst are typical conditions in the study of photocatalytic activity. Depending on their properties such as potentials, electrical charge numbers, absorption wavelength and competition reactions etc., choosing carefully suitable combinations is necessary. A possible phenomenon to occur is ion pair formation between these elements which might affect the bimolecular electron transfer. For the ion pair formation, the charge number of the anion and the cation is a main factor to consider together with the dielectric constant of the solvent. In this study, the copper(II) complex, copper(II) N,N'-o-phenylenebis (methanamide) $[Cu^{II}OPBI]^{2-}$, and methylviologen (MV^{2+}) were used which are dianionic and dicationic, respectively.

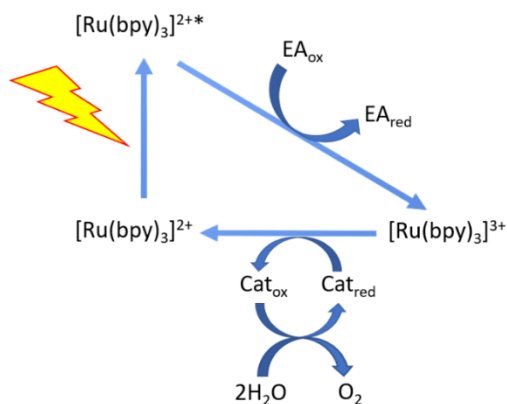


Figure 3-1 Three-component system for light-driven water oxidation consisting of a catalyst (Cat), $[\text{Ru}(\text{bpy})_3]^{2+}$ photosensitizer and electron acceptor (EA).

The *o*-phylene-bisoxamidate copper (II) complex was studied in terms of stabilization of Cu (III) complex by Ruiz and co-workers.^[52] Steggerd and co-workers also mentioned that in a bidentate ligand which consists of oxamide dianion $\text{C}_2\text{O}_2\text{N}_2\text{H}_2^{2-}$, amide nitrogen atoms have a role as strong electron-donating groups, stabilizing the high oxidation state of copper(III) and nickel (III).^[85]

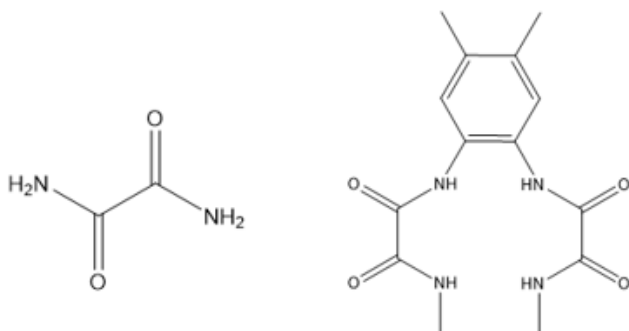
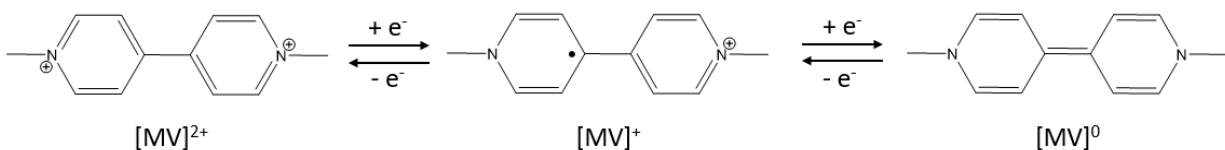


Figure 3-2 Oxamide dianion ($\text{C}_2\text{O}_2\text{N}_2\text{H}_2^{2-}$) (left) and its bidentate ligand (right)

Methylviologen (N,N'-dimethyl-4,4'-bipyridinium dichloride, the dication notated as MV^{2+}) is well known as an electron-acceptor which can be reduced twice. In a first reversible one-electron reaction methyl viologen, MV^{2+} is reduced at - 0.5 V (vs. SCE) to a strongly colored blue radical cation (MV^+ , $\lambda_{\text{max}} = 600 \text{ nm}$, $\epsilon = 14000 \text{ M}^{-1}\text{cm}^{-1}$). The second reduction occurs at - 0.95 V (vs. SCE) and forms the neutral, fully reduced form (MV^0) (Scheme 3-1).^[90,91]



Scheme 3-1 Accessible redox and charge states of methylviologen.

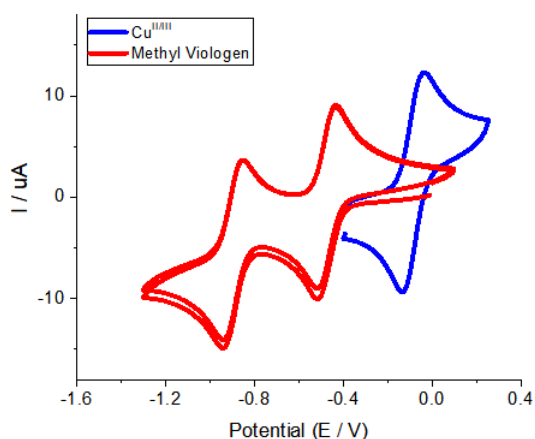


Figure 3-3 CV of Methyl Viologen (red) and $\text{Cu}^{\text{II/III}}$ of $\text{Cu}^{\text{I}}\text{OPBI}$ (blue).

As shown in Fig. 3-3, the first reduction potential of $\text{MV}^{+/2+}$, $E_{1/2, \text{MV}^{+/2+}}$ is lower than the potential of $\text{Cu}^{\text{II/III}}$. Thermodynamically, MV^{2+} cannot oxidize Cu^{I} and these compounds were considered good candidates as electron-acceptor for charge shifts studies in photocatalysis system. However, upon mixture of all the ingredients to do photocatalysis we observed the formation of a MV^+ . We tried to discover how this phenomenon occurs by investigating the photophysical study between the Ru photosensitizer and the copper complex then the study of mixture MV^{2+} and the Cu complex. The mixture of MV^{2+} and $[\text{Cu}^{\text{I}}\text{OPBI}]^{2-}$ under argon condition in ACN, leads to radical cation (MV^+) formation as evidenced by the blue color and by UV-Vis spectra.

3.2. Synthesis and Characterizations

3.2.1. Synthesis

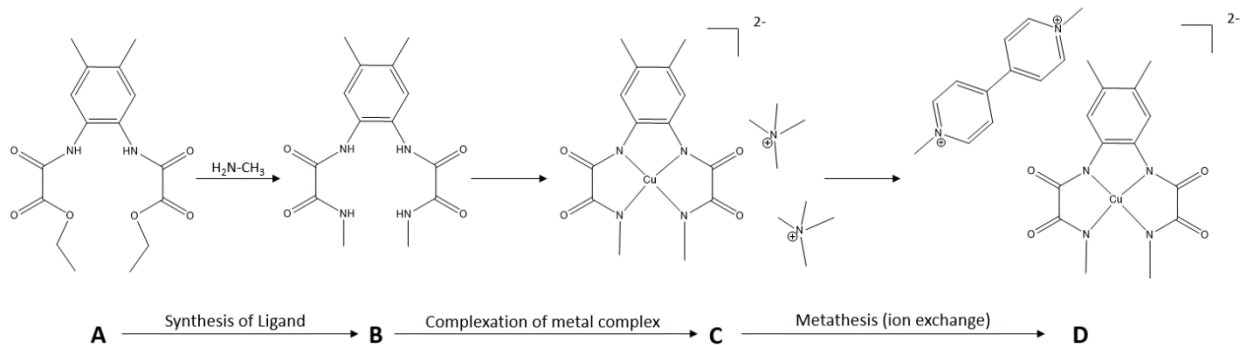
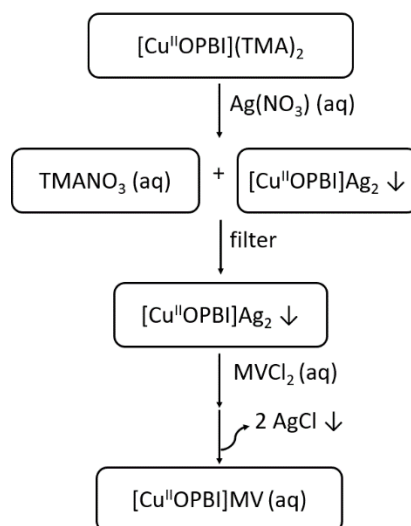


Figure 3-4 Synthesis procedure, A \rightarrow B. Synthesis of Ligand, B \rightarrow C. Complexation of Cu Complex, C \rightarrow D. Metathesis (ion exchange)

The synthesis was performed in 3 steps. As already mentioned in the **Chapter 2**, $[\text{Cu}^{\text{II}}\text{OPBI}]^{2-}$ was used as a continuous study. In the complexation of metal and ligand (B \rightarrow C), the metal complexes, Cu (II) and Ni (II) were prepared by treating the dissolved proligand in MeOH with a base (tetramethylammonium hydroxide, TMAOH) followed by the addition of the corresponding metal salt ($\text{X}(\text{ClO}_4)_2 \cdot 6\text{H}_2\text{O}$, X = Cu and Ni). We added metathesis procedure between $[\text{Cu}^{\text{II}}\text{OPBI}](\text{TMA})_2$ and Methylviologen (MVCl_2) (C \rightarrow D). The following describes the procedure of ion exchange (C \rightarrow D).

Metathesis (ion exchange) (C \rightarrow D)



Scheme 3-3 Protocol of Metathesis between $[\text{Cu}^{\text{II}}\text{OPBI}](\text{TMA})_2$ and Methyl Viologen (MVCl_2).

To simplify the system ions exchange via metathesis was performed to obtain the isolated $[\text{Cu}^{\text{II}}\text{OPBI}]\text{MV}$ compound, which has no more counter ions was compared with the mixture of $[\text{Cu}^{\text{II}}\text{OPBI}](\text{TMA})_2$ and $\text{MV}(\text{PF}_6)_2$ which includes counter ions, in this case TMA^+ and PF_6^- , respectively.

$[\text{Cu}^{\text{II}}\text{OPBI}](\text{TMA})_2$ (309 mg, 0.6 mmol, 1.00 eq) was dissolved in water (20 mL). After addition of AgNO_3 (204 mg, 1.2 mmol, 2 eq.) the solution was stirred at room temperature for 10 min. A precipitate was formed which is $[\text{Cu}^{\text{II}}\text{OPBI}]\text{Ag}_2$. After centrifugation, the brownish solid was recovered and then dispersed in water. MVCl_2 (154.2mg, 1 eq.) was used for the chemical reaction to produce $[\text{Cu}^{\text{II}}\text{OPBI}]\text{MV}$ and the solid state AgCl was removed. The filtered solution was treated by acetone for the slow vapor diffusion. The final product was obtained as black solid precipitate and dried.

3.2.2. Characterizations

A) ^1H NMR analysis of Ligand

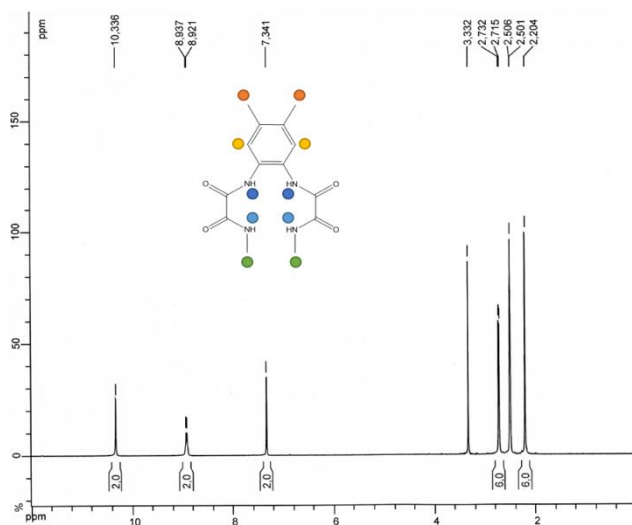


Figure 3-5 NMR spectra of ligand OPBI in DMSO solvent

Fig. 3-5 shows ^1H -NMR spectrum of the ligand obtained in deuterated DMSO solvent. Each color represents a set of protons as depicted on the figure. The signal assignment at δ 10.34 is attributed to the two hydrogen (blue, H-Nph). The quadruplet signal assignment at δ 8.93 is

attributed to the N-protons of the tetradentate ligand (sky blue, H-NMe) for two hydrogen. The presence of signal assignment at δ 7.34 associated with the m-proton of the benzene ring (yellow). The doublet signal at δ 2.73 is attributed to the N-methyl protons of the tetradentate ligand (green) and δ 2.20 belong to six hydrogens on the methyl protons of the benzene ring.^[52]

B) MS analysis of $\text{CuL}(\text{TMA})_2$

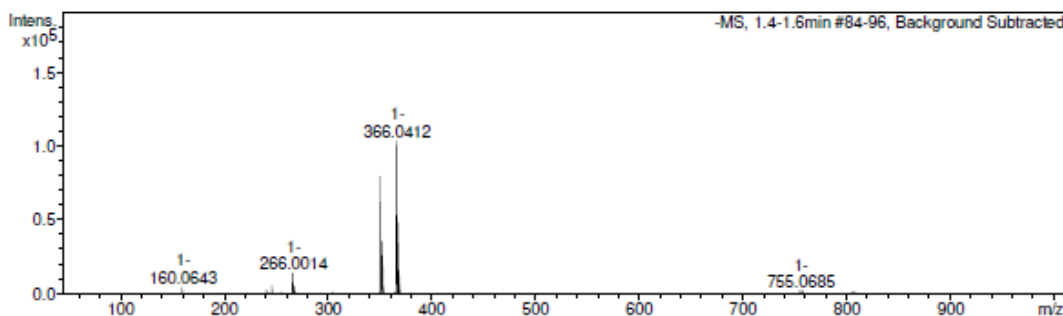


Figure 3-6 ESI-MS (negative mode) of the complex $[\text{Cu OPBI}]^{2-}$ anion, $[\text{CuL}^+\text{H}]^-$ ($m/z = 366.04$)

For the MS analysis of $[\text{Cu}^{\text{II}}\text{OPBI}](\text{TMA})_2$, measured in negative mode, the fraction $[\text{Cu}^{\text{II}}\text{OPBI}^+\text{H}]^-$ was observed with the value $m/z = 366.04$. However, for analysis MS of $[\text{Cu}^{\text{II}}\text{OPBI}]\text{MV}$, it was not possible to get the clear fraction value of m/z .

C) IR analysis (MVCl_2 , $[\text{Cu}^{\text{II}}\text{OPBI}](\text{TMA})_2$ and $[\text{Cu}^{\text{II}}\text{OPBI}]\text{MV}$)

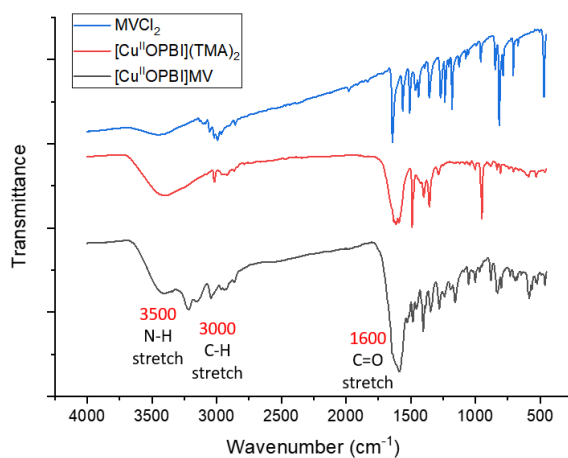


Figure 3-7 IR spectra of MVCl_2 , $[\text{Cu}^{\text{II}}\text{OPBI}](\text{TMA})_2$ and $[\text{Cu}^{\text{II}}\text{OPBI}]\text{MV}$.

IR analysis of $[\text{Cu}^{\text{II}}\text{OPBI}]\text{MV}$ was a suitable method to follow the metathesis reaction sequence. The metathesis was performed via eliminating counter ions in aqueous solution and then the compound produced by slow vapor diffusion.

At 3000 cm^{-1} a band corresponding to the stretching vibration of the C-H bond from MV^{2+} is observed. At around 1600 cm^{-1} for MV^{2+} were overlapped by stretching vibration of the C=O bond and π delocalization of the carbonyl double bond of NCO amido group was observed at around 1600 cm^{-1} from Cu complex and $[\text{Cu}^{\text{II}}\text{OPBI}]\text{MV}$.^[104] The band at 3500 cm^{-1} was observed both for $[\text{Cu}^{\text{II}}\text{OPBI}](\text{TMA})_2$ and $[\text{Cu}^{\text{II}}\text{OPBI}]\text{MV}$.^[52]

D) Crystal structures : $[\text{Cu}^{\text{II}}\text{OPBI}](\text{TMA})_2$ and $[\text{Cu}^{\text{II}}\text{OPBI}]\text{MV}$

Crystals of $[\text{Cu}^{\text{II}}\text{OPBI}](\text{TMA})_2$ were obtained by slow diffusion of ether in DMF solution of the complexes. A view of the structure of the $[\text{Cu}^{\text{II}}\text{OPBI}](\text{TMA})_2$ is shown in Fig. 3-8 (above). The coordination sphere of the copper ion can be described as a square planar geometry with four nitrogen atoms from the deprotonated oxamidate functions that can be viewed as a $[\text{Cu}^{\text{II}}\text{N}_4]^{2-}$ motif. The Cu-N bond distances lie in the range of 1.85 - 1.90 Å. Two tetramethyl ammonium cation counterbalance the dianionic charge of the copper complex.

Recrystallisation of the $[\text{Cu}^{\text{II}}\text{OPBI}]\text{MV}$ was realized in an aqueous solution with slow diffusion of acetone. Yellow crystals were obtained together with the formation of a dark crystalline powder and were analyzed by X-ray diffraction technique. To our surprise, we noticed that the chemical formulation of the yellow crystals can be formulated as $2[\text{Cu}^{\text{II}}\text{OPBI}]$ for 1 MV^{2+} in the unit cell. A closer inspection of the copper complex coordination sphere reveals that only three deprotonated amido functions are bound to the copper(II) ion while the fourth amido function is in the protonated form and is twisted to bring the oxygen atom from the carbonyl fragment in the coordination sphere (Fig. 3-8 (bottom)). Hence, the copper complex is conferred with only one negative charge thereby leading to the observed chemical formulation $2[\text{Cu}^{\text{II}}\text{N}_3\text{O}]^-$ for 1 MV^{2+} . The Cu-N (amide) bond distances lie in the range 1.90 - 1.92 Å, being longer than those of the analogous bonds in $[\text{Cu}^{\text{II}}\text{N}_4]^{2-}$ while the oxygen atom from the protonated amide function distance lies at 2.01 Å from the copper ion.

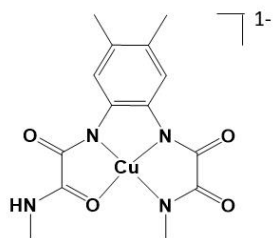
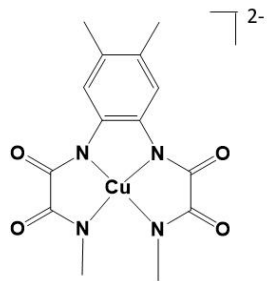


Figure 3-8 Microscopy image of Crystals of $[Cu^{II}OPBI](TMA)_2$ (above) and $[Cu^{II}OPBI]MV$ (bottom).

3.3. Electrochemical Study

3.3.1. Cyclic Voltammetry (CV)

A) [Cu^{II}OPBI](TMA)₂ vs. [Cu^{II}OPBI]MV

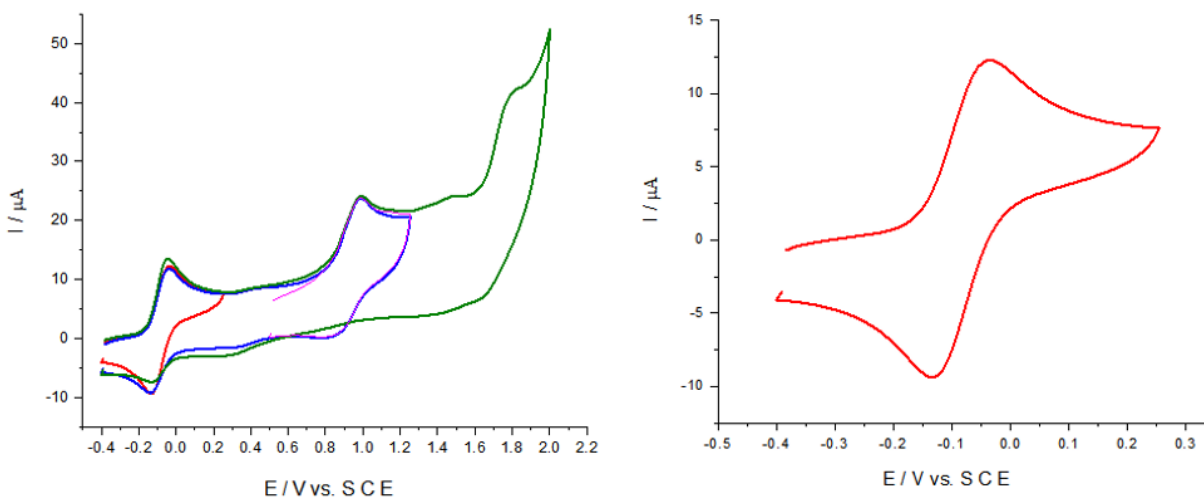


Figure 3-9 CVs of 1.0 mM [Cu^{II}OPBI](TMA)₂ in ACN, 0.1 M TBAPF₆ with different potential range. The red CV corresponds to Cu^{II/III}. Scan rate: 100 mVs⁻¹; working electrode: GCE; reference electrode: SCE.

Fig. 3-9. shows the CVs of the compound [Cu^{II}OPBI](TMA)₂ recorded under the experimental conditions (see figure caption). The OCP (Open circuit potential) was around -0.1 V and the first reversible redox wave (red), corresponding to Cu^{II/III} occurs at a potential, $E_{1/2} = -0.04$ V. The second redox wave around 0.9 V and other peaks represent ligand oxidation.^[52] No cathodic feature was observed even when scanning to negative potential ruling out the formation of Cu^{II/I}. Despite of the clear CV of the [Cu^{II}OPBI](TMA)₂, the solubility in ACN was limited in concentration. Since only low concentration of [Cu^{II}OPBI](TMA)₂ dissolved in ACN, we choose alternative solvent and MeOH was good candidate to dissolve [Cu^{II}OPBI](TMA)₂. Finally, the mixture of ACN and MeOH (50:50) was used. Depending on the solvent, the potential peak can be shifted based on the compound structure.

Fig. 3-10. shows the CVs of the compound [Cu^{II}OPBI](TMA)₂ in mixed solvent condition (ACN:MeOH=50:50). The slightly different of redox potential of Cu^{II/III} indicates the solvent effect.

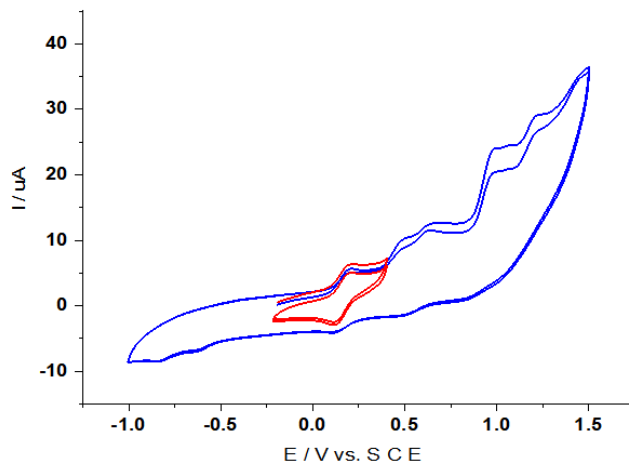


Figure 3-10 CVs of 1.0 mM $[\text{Cu}^{\text{II}}\text{OPBI}](\text{TMA})_2$ in a 0.1 M TBAPF_6 in $\text{ACN}:\text{MeOH}$ (50:50). The red CV corresponds to $\text{Cu}^{\text{II/III}}$. Scan rate: 100 mVs^{-1} ; working electrode: GCE; reference electrode: SCE.

The redox potential of $\text{Cu}^{\text{II/III}}$ shifted positively ($E_{1/2} = 0.2 \text{ V}$) and it might be affected by hydrogen (H) bonding. The observed shift towards more positive potentials can be due to hydrogen bonding effect between methanol and the external oxygen atoms of the oxamate groups.

The mixture solvent condition ($\text{ACN}:\text{MeOH}=50:50$) was used for electrochemical study of $[\text{Cu}^{\text{II}}\text{OPBI}]\text{MV}$. Running the cyclic voltammogram of $[\text{Cu}^{\text{II}}\text{N}_3\text{O}]_2\text{MV}$, we observed a redox process with an $E_{1/2} = 0.6 \text{ V}$ vs. SCE. This wave is attributed to the $\text{Cu}^{\text{III/II}}$ couple as no redox feature is expected for the MV^{2+} in the anodic part of the CV. This positive shift ca. 400 mV with respect to the $[\text{CuN}_4]^{2-}$ coordinating scheme, support the stronger ligand field strength provided by the four deprotonated amido groups in comparison with the three ones in the case of $[\text{Cu}^{\text{II}}\text{N}_3\text{O}]_2\text{MV}$. With the goal to investigate on the change in redox potential with the protonic state of the amido function, we added one equivalent of tetramethylammonium hydroxide (TMAOH). Interestingly, we found that the redox wave shifted $E = 0.2 \text{ V}$ vs. SCE, the same redox potential we already observed in the case for a $[\text{CuN}_4]^{2-}$ coordination site. Not only the potential shift, but also the visible change was occurred in the presence of TMAOH. Upon mixing TMAOH, the color of solution became blue which it seems MV^+ . It can be explained that MV^{2+} is reduced to MV^+ in alkaline aqueous and methanolic solution under anaerobic condition.^[105]

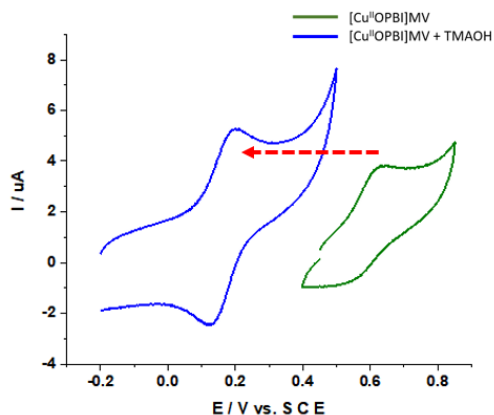


Figure 3-11 CVs of 1.0 mM $[\text{Cu}^{\text{II}}\text{OPBI}]\text{MV}$ with 1 eq. of base (TMAOH, blue) and without base (green) in ACN:MeOH (50:50)

Further insight in the coupled proton transfer electron transfer process with the $[\text{CuN}_4]^{2-}$ complex was gained by running the CV upon addition of one equivalent of a weak acid .^[106]

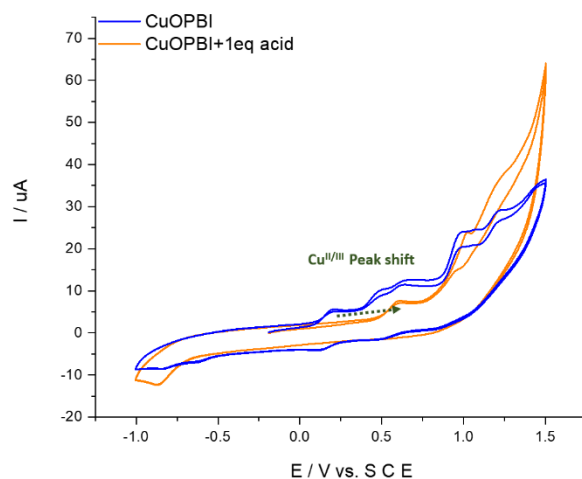


Figure 3-12 CVs of 1.0 mM $[\text{Cu}^{\text{II}}\text{OPBI}](\text{TMA})_2$ adding 1 eq. of (acetic acid) in ACN:MeOH (50:50)

Fig. 3-12. shows the CV of $[\text{CuN}_4]^{2-}$ and upon addition of 1 eq. of acetic acid. Interestingly, the same redox behavior is observed, that is to say, the initial wave for the $\text{Cu}^{\text{III/II}}$ couple for the complex $[\text{CuN}_4]^{2-}$ is shifted to a wave peaking at $E_{1/2} = 0.6$ V vs SCE as the one observed with $[\text{Cu}^{\text{II}}\text{OPBI}]\text{MV}$. This result matches the proposal that upon protonation there is a subsequent anodic shift of the $\text{Cu}^{\text{III/II}}$ couple.

3.4. UV-Vis spectroscopy

3.4.1. $[\text{Cu}^{\text{II}}\text{OPBI}](\text{TMA})_2$

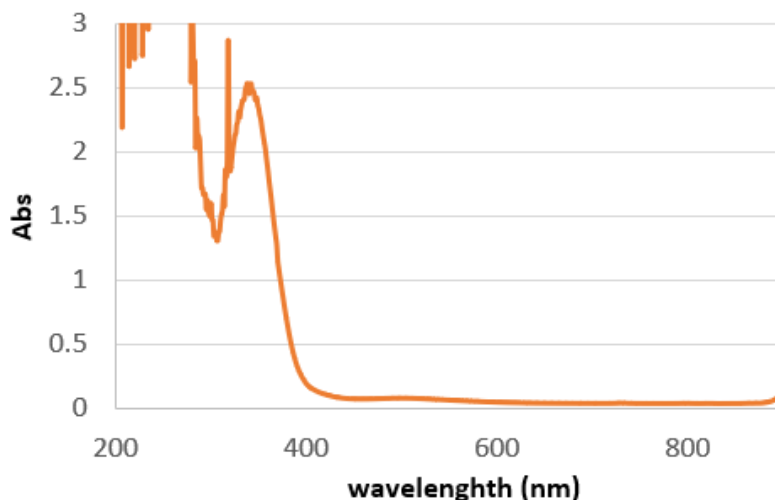


Figure 3-13 UV-Vis spectra of $100 \mu\text{M} [\text{Cu}^{\text{II}}\text{OPBI}](\text{TMA})_2$ in ACN.

The UV-Vis absorption spectrum of the $[\text{Cu}^{\text{II}}\text{OPBI}](\text{TMA})_2$ in ACN is shown in Fig. 3-13. The intense band in the UV region centered at 340 nm with second less intense small band in the visible region located the range 500 - 560 nm. The high-energy peak is corresponding to π - π^* transition including the aromatic ring of the ligand and the weak band is from d-d transition of Cu^{II} in square-planar geometry.^[52]

3.4.2. Ion pair formation between $[\text{Cu}^{\text{II}}\text{OPBI}](\text{TMA})_2$ and $\text{MV}(\text{PF}_6)_2$

As we mentioned above, we have been interested in understanding the puzzling observation of a blue solution when the Cu complex, $[\text{Cu}^{\text{II}}\text{OPBI}](\text{TMA})_2$ was mixed with methylviologen (MV^{2+}) in ACN, under anaerobic conditions. This blue color suggested formation of $\text{MV}^{\cdot+}$. We reasoned that ion pair formation between the two oppositely charged species could play a role. To support the occurrence of ion pair association, UV-Vis spectra as function of time (time resolved) were recorded to follow the formation of the $\text{MV}^{\cdot+}$ radical by monitoring its characteristic absorption bands at 400 nm and 605 nm. Fig. 3-14 shows the experimental set-up for time resolved UV-Vis

spectra. The temperature of the solution was controlled by a liquid nitrogen cryostat and kept under constant stirring. Different amount of methylviologen was introduced and the kinetics was studied as function of temperature from -10 to 60 °C. Anaerobic condition were established by bubbling with ACN-saturated nitrogen gas and were found to be necessary to avoid the reaction between $MV^{+•}$ and oxygen (O_2).

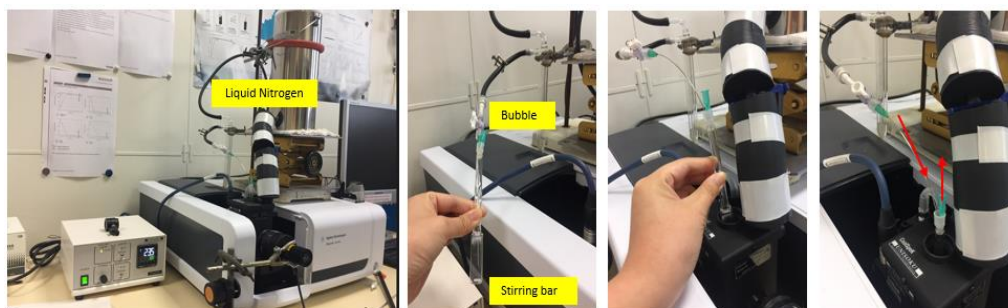


Figure 3-14 Experimental set-up for time resolved measurements.

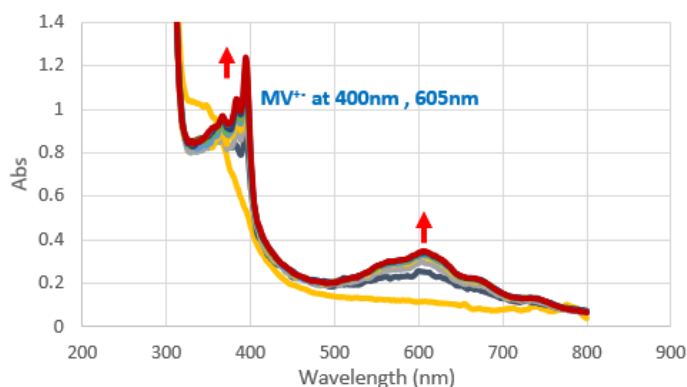


Figure 3-15 UV-Vis time resolved spectra after mixing of 100 μM $[Cu^{II}OPBI](TMA)_2$ and 10 mM of $MV(PF_6)_2$. The spectra were measured every 2 min. for 2 hours.

The evolution of the UV-Vis time-resolved spectra after mixing 100 μM $[Cu^{II}OPBI](TMA)_2$ and 10 mM of $MV(PF_6)_2$ is shown in Fig. 3-15. The spectra were measured every 2 min. for 2 hours and show absorption increase at 400 nm and 605 nm leading to clearly visible blue solution in the cuvette.

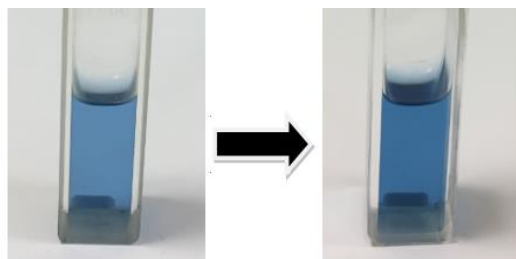


Figure 3-16 The color change of mixture of $100 \mu\text{M}$ $[\text{Cu}^{\text{II}}\text{OPBI}](\text{TMA})_2$ + 10 mM of $\text{MV}(\text{PF}_6)_2$. Left: after 40 min, Right: after 2 hrs.

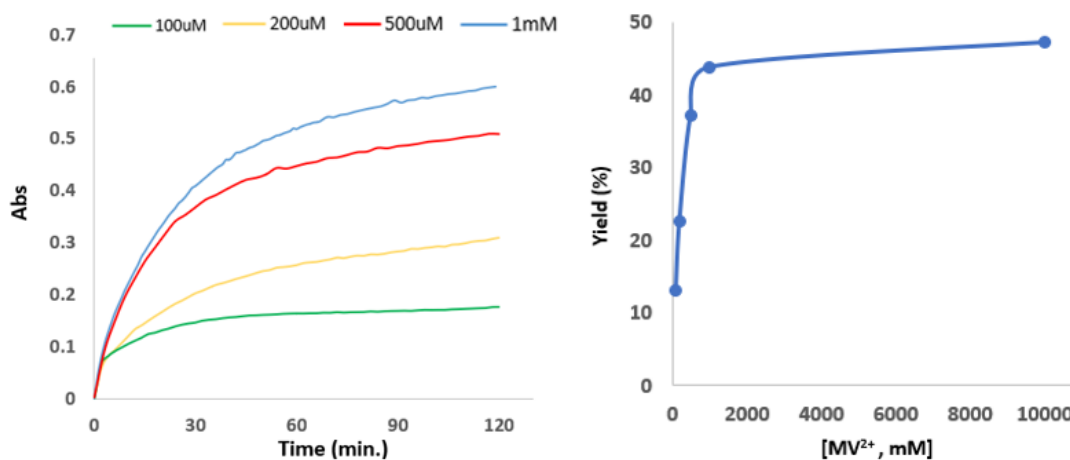


Figure 3-17 UV-Vis time resolved plot (left) Abs vs. Time (min.) at the wavelength 605 nm of the mixture between $100 \mu\text{M}$ $[\text{Cu}^{\text{II}}\text{OPBI}](\text{TMA})_2$ with different concentration of $\text{MV}(\text{PF}_6)_2$ (100, 200, 500, 1000 and 10000 μM). The yield of MV^+ was calculated by dividing with $[[\text{Cu}^{\text{II}}\text{OPBI}]^{2-}] = 100 \mu\text{M}$ and it plot as function of $[\text{MV}^{2+}]$. The data were taken after 2 hours.

The kinetic study of electron transfer leading to the formation of MV^+ was performed by UV-Vis time resolved plot Abs vs. Time (min.) at 605 nm which shows the evolution of the MV^+ . Fig 3-17 and Table 3-1 show the results of Abs and yield of MV^+ . The mixture between $100 \mu\text{M}$ $[\text{Cu}^{\text{II}}\text{OPBI}](\text{TMA})_2$ with different concentration of $\text{MV}(\text{PF}_6)_2$ (100, 200, 500, 1000 and 10000 μM) were used and the yield of $[\text{MV}^+]$ was calculated by using the $\epsilon = 14000$ of MV^+ . The percent (%) yield is $[\text{MV}^+]$ divided by concentration of Cu complex, $[[\text{Cu}^{\text{II}}\text{OPBI}]^{2-}] = 100 \mu\text{M}$ and it is plotted as function of $[\text{MV}^{2+}]$ in Fig. 3-17. The concentration of MV^{2+} , $[\text{MV}^{2+}]$ was varied from 100 μM , which is 1 eq of, $[[\text{Cu}^{\text{II}}\text{OPBI}]^{2-}] = 100 \mu\text{M}$ and to an excess amount, 100 eq. The initial slope in the plot increases with increasing eq. of MV^{2+} showing acceleration of the reaction with higher concentrations of MV^{2+} . The interesting thing is the yield of MV^+ after 2 hrs. The calculated yield after 2 hrs for different $[\text{MV}^{2+}]$ shows that the maximum yield reached was around 50 %, with an excess eq. of $[\text{MV}^{2+}]$. This result suggests that only 50 % of $[\text{Cu}^{\text{II}}\text{OPBI}]^{2-}$ are oxidized.

Table 3-1 The data summary from the Fig. 3-17. The Abs of MV⁺ after 2 hrs at the wavelength 605 nm as function of the [MV²⁺] in [[Cu^{II}OPBI]²⁻] = 100 μM. [MV⁺] was calculated by using the ε of MV⁺.

[MV ²⁺], μM	Abs @605 nm	[MV ⁺], μM	Yield (%) ([MV ⁺]/[[Cu ^{II} OPBI] ²⁻] x 100)
100	0.18	13.01	13.01
200	0.31	22.60	22.60
500	0.51	37.16	37.16
1000	0.60	43.86	43.86
10000	0.62	47.31	47.31

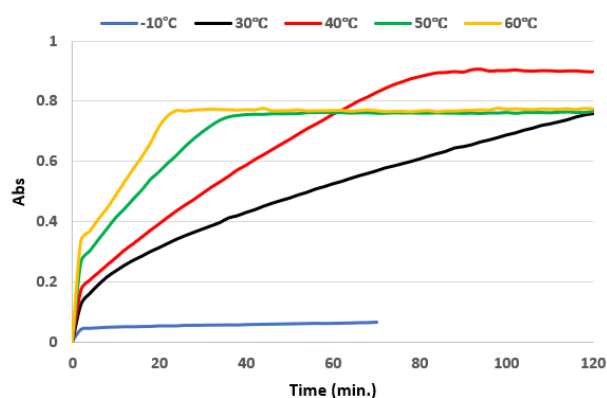


Figure 3-18 UV-Vis time resolved plot Abs vs. Time (min.) at the wavelength 605 nm of the mixture 100 μM [Cu^{II}OPBI](TMA)₂ with excess eq. of 100 mM MV(PF₆)₂ (100 eq.) for different temperatures (-10, 30, 40, 50 and 60 °C)

As we have noticed before, at room temperature (30°C) there was a gradual increase in the formation of methylviologen that did not reach a plateau after two hours (see Fig. 3-18). Hence, we performed a set of temperature control experiment fixing the concentration of MV²⁺ at 100 mM and the concentration of the copper complex at 100 μM with the target to evaluate the rate of formation of MV⁺ as a function of temperature. For this, a series of experiments from -10 °C to 60 °C were realized. Fig. 3-18 shows the results of time resolved plot at different temperature. At -10 °C, the kinetic was too slow and no marked changes in the optical spectra was evidenced. As discussed above, at 30 °C, a constant increase was found to reach a yield over 50 % (0.78/14000 = 57 %). Increasing the temperature to 40 °C, both kinetic and yield increased to attain plateau at 64 % yield. Experiments done at higher temperature than 40°C i.e. 50 and 60°C lead to an increase in the rate of formation of MV⁺.

3.4.3. Effect of dielectric constant

The mixture of 100 mM of MV^{2+} ($MVCl_2$, in this case) and 100 μM of $[Cu^{II}OPBI]^{2-}$ in water did not exhibit any formation of new peaks at 400 nm and 605 nm attributable to the methylviologen radical. Concerning the water which has high dielectric constant solvent, many studies of methyl viologen in water have investigated that the blue color of methyl viologen radical cation ($MV^{\cdot+}$) exists stable and can be detected by the UV-Vis spectra.^[107,108] We reasoned that the ion pair formation and electron transfer phenomenon is affected by the nature of the solvent.^[109] The effect of dielectric constant has investigated in terms of ion pair formation. Low dielectric constant organic solvents such as DMSO, DMF and DCM had similar phenomenon of ion pair formation and electron transfer as in ACN, which we already discovered in the previous part (Fig. 3-19 and Table 3-2).

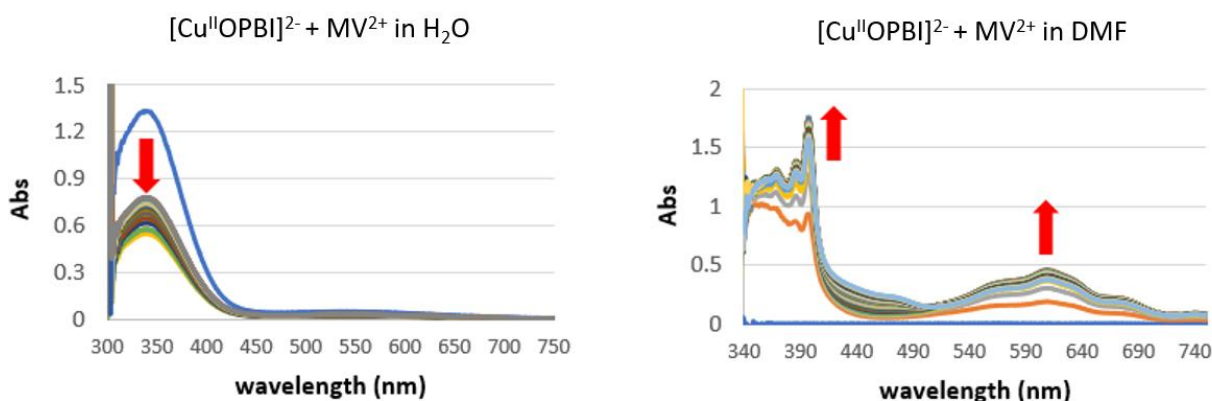


Figure 3-19 UV-Vis spectra of the mixture between 100 μM of $[Cu^{II}OPBI]^{2-}$ with 100 mM of MV^{2+} in different solvent : In water (left) and in DMF (right).

Table 3-2 Effect of dielectric constant of solvent for ion pair formation and electron transfer.

Solvent	Dielectric constant	Ion pair formation & electron transfer
ACN	38	Yes
DMF	37	Yes
DMSO	47	Yes
DCM	9	Yes
H ₂ O	80	No

3.5. EPR measurements

Given the paramagnetic nature of the initial copper (II), we used the EPR spectroscopy to monitor the electron transfer processes undergoing between the copper (II) complex and the methylviologen.

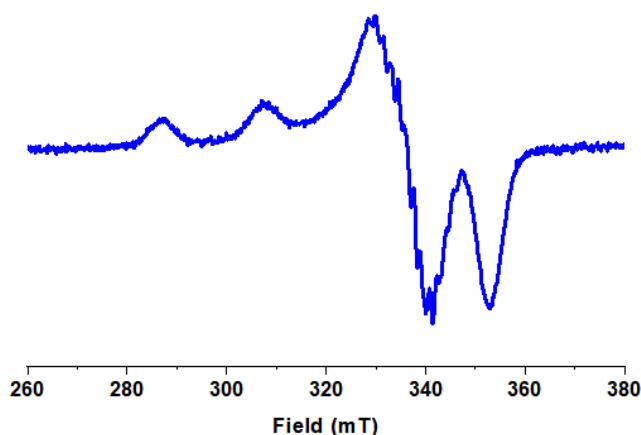


Figure 3-20 EPR spectra of $[\text{Cu}^{\text{II}}\text{OPBI}](\text{TMA})_2$ in DMSO+ACN (10:90) solution.

Fig. 3-20 shows the EPR spectra of paramagnetic $[\text{Cu}^{\text{II}}\text{OPBI}](\text{TMA})_2$, with g_{\parallel} and g_{\perp} values equal to 2.155 and 2.045. The X-band EPR spectrum indicates a typical square planar copper (II) complex. Peisach et al. described the g -values of tetragonal and square-planar-based geometries with $g_{\parallel} > g_{\perp} > 2$ and associated $I = 3/2$ hyperfine couplings of Cu nucleus split of g_{\parallel} resonance into four lines.^[110] The EPR spectra refers to $d_{x^2-y^2}$ ground state paramagnetic orbital.^[111] Moreover, the mixing of the d_{z^2} orbital into the paramagnetic orbital may affect to the distortion of tetragonal geometry.^[111]

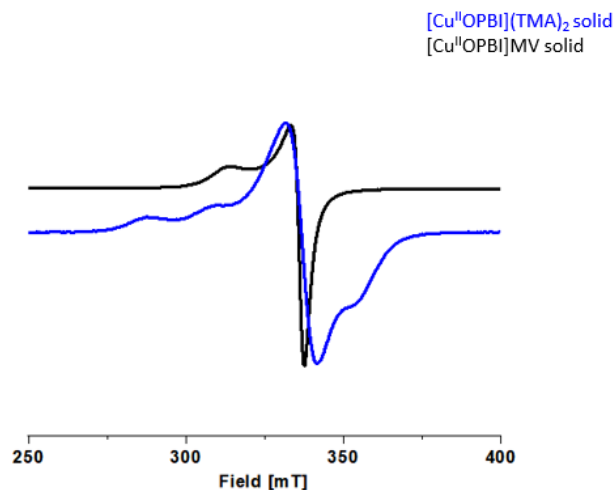


Figure 3-21 X-band EPR spectra of $[\text{Cu}^{\text{II}}\text{OPBI}](\text{TMA})_2$ (blue) and $[\text{Cu}^{\text{II}}\text{OPBI}]\text{MV}$ (black) in solid state.

Fig. 3-21 is represented the spectrum of the copper complex superimposed with the metathesis compound $[\text{Cu}^{\text{II}}\text{OPBI}]\text{MV}$ in solid state. As it can be noticed there is a drastic change in the morphology of the EPR spectra. While the initial copper (II) complex presented a rhombic signal, the one obtained from the mixture of the copper complex and methylviologen is mostly axial with $g_{\parallel} = 2.19$ and $g_{\perp} = 2.04$. It indicates that $[\text{Cu}^{\text{II}}\text{OPBI}]\text{MV}$ which can be understood as Cu (II) ion formation, $[\text{Cu}^{\text{II}}\text{OPBI}]^{2-}\text{MV}^{2+}$ was not the case in solid state. The splitted g_{\parallel} resonance disappeared and the broad splitting into two lines in the downside became one sharp line.

The formation of such a paramagnetic species was quite surprising and lead us to perform a set of experiments in solution. With the target to decipher the locus of the lone electron for the paramagnetic species, we carried on the measurement in solution state. Fig. 3-23 shows $[\text{Cu}^{\text{II}}\text{OPBI}](\text{TMA})_2$ and mixture of $[\text{Cu}^{\text{II}}\text{OPBI}]\text{MV}$ in DMSO+ACN (10:90) solvent, respectively. Based on Scheme 3-2, we reasonable argued that under an aerobic condition the formation of the methylviologen radical, detected by its classic absorption bands at 400 and 605 nm, should be accompanied by the oxidation of the copper (II) complex to a Cu (III) species. This oxidized Cu (III) complex with a d^8 electronic configuration should be diamagnetic and EPR silent in nature. In Fig. 3-22, we depict the spectra of the copper (II) complex and the mixture of the copper complex with methylviologen under anaerobic condition. As we clearly noticed that upon addition of MV^{2+} , we evidenced a change from a metal center paramagnetic center ($g = 2.05$) to

a more metalloradical species with $g = 2.00$. A more in depth EPR study together with DFT calculations to support the assumption.

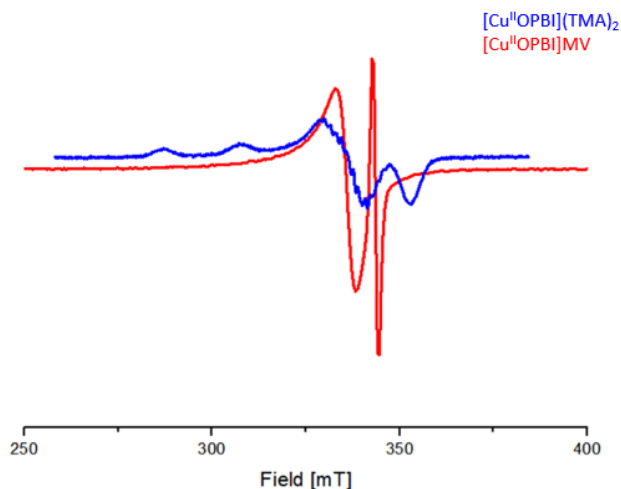


Figure 3-22 X-band EPR spectra of $[\text{Cu}^{\text{II}}\text{OPBI}]\text{MV}$ and $[\text{Cu}^{\text{II}}\text{OPBI}](\text{TMA})_2$ in DMSO+ACN (10:90) solution.

As we have witnessed in the study as a function of temperature that the generation of the $\text{MV}^{\cdot+}$ radical was not complete even in an excess of MV^{2+} . In order to delineate the nature of the paramagnetic species we have performed an EPR study as a function of temperature (Fig. 3-23). Interestingly, we found that at low temperature, the spectrum is dominated by the signal for the copper (II) center with g_{\parallel} and g_{\perp} values equal to 2.18 and 2.05 which are typical for the $[\text{Cu}^{\text{II}}\text{OPBI}](\text{TMA})_2$. We also noticed the presence of a radical species with a g value at 2.00. Increasing the temperature, we monitored the disappearance of the copper (II) signals at the expense of the radical species. Henceforth we can reasonably propose that there is a dynamic equilibrium of the locus of the spin from the metal to the methylviologen such as the one observed for a valence tautomeric phenomenon. The fact that the EPR signal shows a strong anisotropy raises the question on the coupling of the $\text{MV}^{\cdot+}$ and the copper ion. A more in depth spectroscopic and theoretical calculations are still needed to shine light on this original electron transfer process upon formation of an ion pair formation.

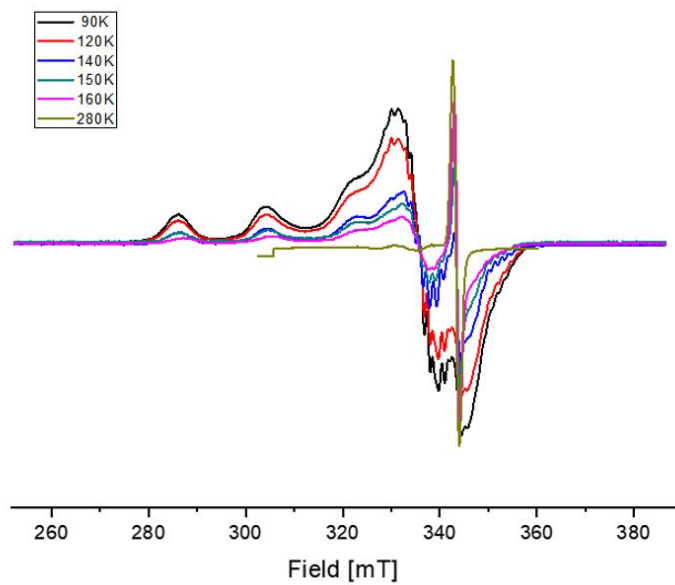


Figure 3-23 X-band EPR spectra of [Cu^{II}OPBI]MV in different temperature in the range 90 K - 280 K in DCM+MeOH (50:50) solution.

3.6. Ni^{II}OPBI ([Ni^{II}OPBI]²⁻) and Cu^{II}OBBZ ([Cu^{II}OBBZ]²⁻)

3.6.1. Ni OPBI ([Ni^{II}OPBI]²⁻)

Based on our observation with the [Cu^{II}OPBI]²⁻ we argued whether this electron transfer phenomenon would prevail with another metal complex holding the same bisoxamidate ligand. For this purpose, we have chosen the [Ni^{II}OPBI]²⁻ as a dianionic diamagnetic square planar complex. Ottenwaelder et al. studied a series of nickel (II) complexes and demonstrated that the ligand with large electron σ -donor could stabilize the trivalent and formally tetravalent nickel.^[53]

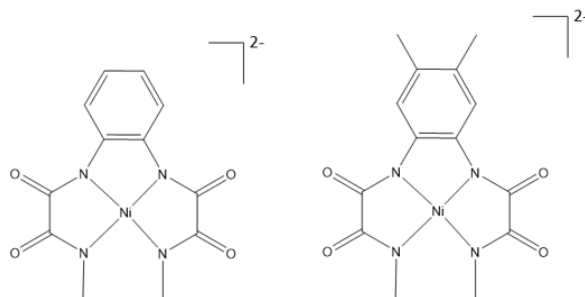


Figure 3-24 Structure of Ni(II) complexes : Ottenwaekder's work (left), in this work (right)

The CV of Ni (II) complex as shown in Fig. 3-25, the lower valent Ni (II) complex can undergo two one-electron oxidation, metal- and ligand-centered.^[53] The half wave potential of Ni^{II/III} is 0.1 V, which is higher than the potential of MV²⁺, $E_{1/2} = -0.45$ V. That gives same concept as Cu^{II}OPBI complex that thermodynamically MV²⁺ cannot oxidize Ni (II) complex.

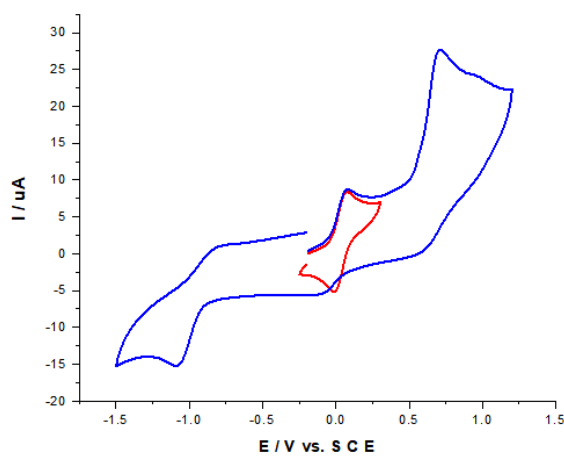


Figure 3-25 CVs of 1.0 mM of [Ni^{II}OPBI](TMA)₂ in a 0.1 M TBAPF₆ in ACN with different potential range. The red CV corresponds to Ni^{II/III}. Scan rate: 100 mVs⁻¹; working electrode: GCE; reference electrode: SCE.

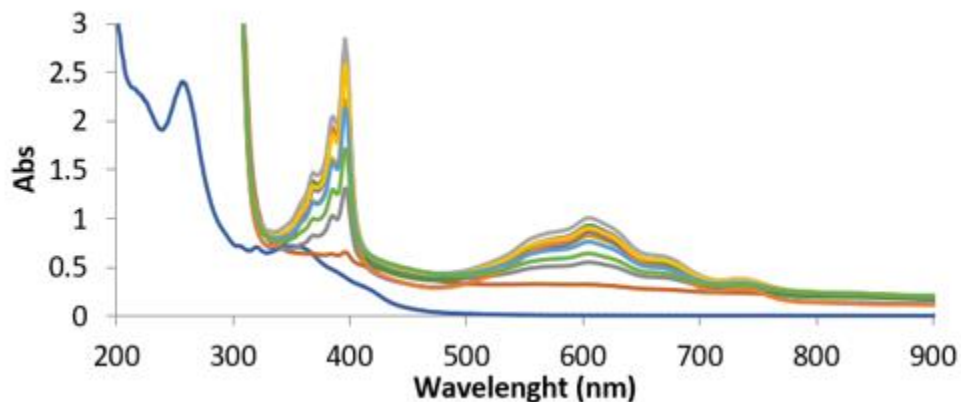


Figure 3-26 UV-Vis time resolved plot (left) Abs vs. Time (min.) at the wavelength 605 nm of the mixture between 100 μM $[\text{Ni}^{\text{II}}\text{OPBI}](\text{TMA})_2$ with 10 mM $\text{MV}(\text{PF}_6)_2$ in ACN.

The phenomenon of $[\text{Ni}^{\text{II}}\text{OPBI}]^{2-}$ with MV^{2+} was monitored by UV-Vis in Fig. 3-26. The summary of kinetic UV-Vis spectra with the different metal complexes, $[\text{Cu}^{\text{II}}\text{OPBI}](\text{TMA})_2$ and $[\text{Ni}^{\text{II}}\text{OPBI}](\text{TMA})_2$ is shown in Fig. 3-27. Each metal complexes have different kinetics under the same conditions. The initial kinetic of $\text{Ni}^{\text{II}}\text{OPBI}$ was the faster than $\text{Cu}^{\text{II}}\text{OPBI}$. In addition, the abs value at the wavelength 605 nm which indicates yield of MV^+ in 2 hrs. also was in order $\text{Ni}^{\text{II}}\text{OPBI} > \text{Cu}^{\text{II}}\text{OPBI}$.

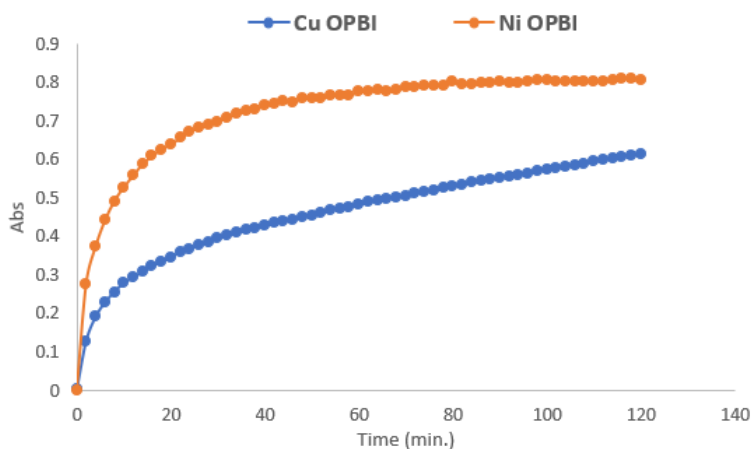


Figure 3-27 UV-Vis time resolved plot Abs vs. Time (min.) at the wavelength 605 nm of the mixture between 10mM of $\text{MV}(\text{PF}_6)_2$ with different metal complexes 100 μM $[\text{Cu}^{\text{II}}\text{OPBI}](\text{TMA})_2$ and $[\text{Ni}^{\text{II}}\text{OPBI}](\text{TMA})_2$ at RT.

3.6.2. Cu^{II}OBBZ ([Cu^{II}OBBZ]²⁻)

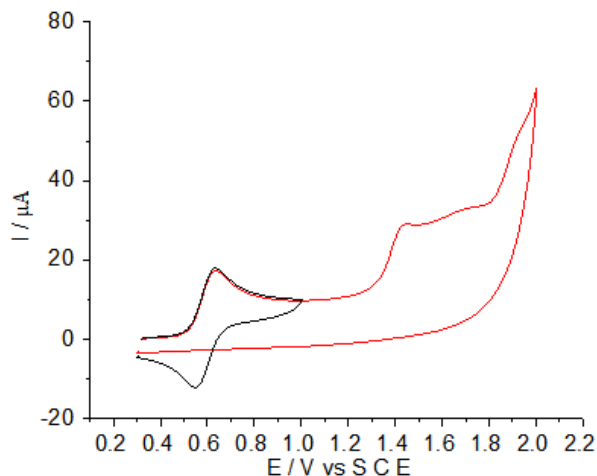


Figure 3-29 CV of 1 mM solutions of [Cu^{II}OBBZ](TMA)₂ complex in ACN containing 0.1 M TBAPF₆ as supporting electrolyte. E / V vs. SCE. $\nu = 100 \text{ mVs}^{-1}$

The different Cu complex of (OBBZ = N,N¹-oxamido bis(benzoato)) OBBZ ligand which has 2- charge, [Cu^{II}OBBZ]²⁻ was also investigated for ion pair formation with MV²⁺.^[86] The electrochemical study of Cu^{II}OBBZ was investigated by CV in the previous **chapter 2** (Fig. 3-29) and the first reversible oxidation occurs around $E_{1/2} = 0.62 \text{ V vs. SCE}$, which it corresponds to a Cu^{II/III} couple. That is, the redox potential of the metal was highly positive than MV²⁺ that these complexes were chosen based on the thermodynamically impossible reactions. Simply, the UV-Vis results of mixture [Cu^{II}OBBZ]²⁻ and MV²⁺ did not yield any new absorption bands, especially at 400 and 605 nm which indicate ion pair association of MV⁺.^[90] Therefore, this study translates the fact that the dianionic nature of the complex is not a prerequisite for the observation of charge transfer with methylviologen.

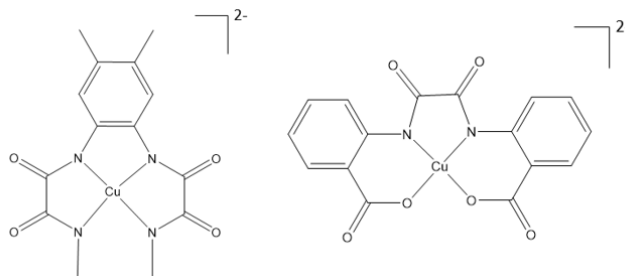


Figure 3-30 Structure of Cu(II) complexes : Cu^{II}OPBI (left), Cu^{II}OBBZ (right)

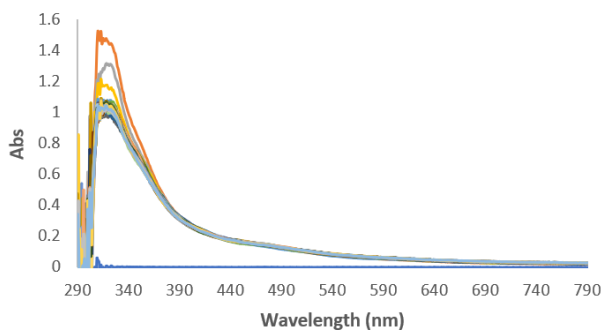


Figure 3-31 UV-Vis time resolved spectra of the mixture between 100 μM Cu^{II} OBBZ (bottom) with 10 mM $\text{MV}(\text{PF}_6)_2$ in ACN.

These preliminary results bring further interrogations on the observed electron transfer phenomenon we have evidenced with the Cu complex. While the same electron transfer phenomenon was observed with the corresponding nickel (II) complex, we have detected any charge transfer process with a dianionic copper complex with two amido and two carboxylate groups in the coordination sphere. However, it is to be pointed out that in the case of the Cu^{II} OBBZ, the redox potential of the $\text{Cu}^{\text{III/II}}$ couple is ca. 0.62 V vs SCE.

3.7. Conclusions & Perspectives

We investigated the ion pair electron transfer between the oppositely double negative charged species of complexes and electron acceptor the methylviologen dication. While we were set to perform the photocatalytic investigation of the copper complex in presence of a photosensitizer and an electron acceptor (methylviologen), we were intrigued by the discovery that the mixture of the copper (II) complex and MV^{2+} lead to the formation of $MV^{\cdot+}$. The ion pair formation was mainly studied by UV-Vis spectra, which gives clear appearance of $MV^{\cdot+}$ and the solvent dielectric constant affect to the phenomenon. Another attempt was the metathesis of $[Cu^{II}OPBI]MV$. By analysis crystal structure we found the protonated complex formed. EPR measurements were the evidence of radical species appear and Cu (II) disappeared.

The different metal species replacing to Ni had similar phenomenon as Cu complex but the yield and initial rate of $MV^{\cdot+}$ was different. Another dianionic Cu complex $Cu^{II}OBBZ$, did not lead to charge transfer phenomenon. Thus, we assume that the role of ion pair formation is strongly dependent on the ligand OPBI.

Small purple crystals of the $[Cu^{II}OPBI]MV$ were obtained upon crystallization in the glove box. However, to date we have not been able to have the x-ray analysis of the species that would accordingly described the reduced form of methylviologen together with the oxidized copper complex. However, the color of these crystals already is clearly not the yellow ones obtained in aerobic conditions. Our effort is guided to have the crystal structure of the charge separated state and its more intimate characterization.

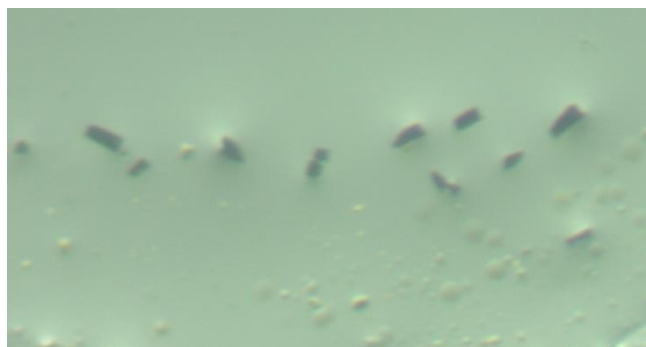


Figure 3-32 Microscopic crystal of $[Cu^{II}OPBI]MV$ in the glove box.

Chapter IV.

Intramolecular Electron Transfer

4. Intramolecular Electron Transfer

In this chapter, we have studied the light-induced intramolecular electron transfer in a Ru-Mn supramolecular complexes, which consist of photosensitizer and a manganese complex linked through an imidazole unit. We discussed here the electron transfer steps and investigated the change in the Mn oxidation states upon exciting the photosensitizer with visible light in the presence of an electron acceptor.

4.1. Introduction

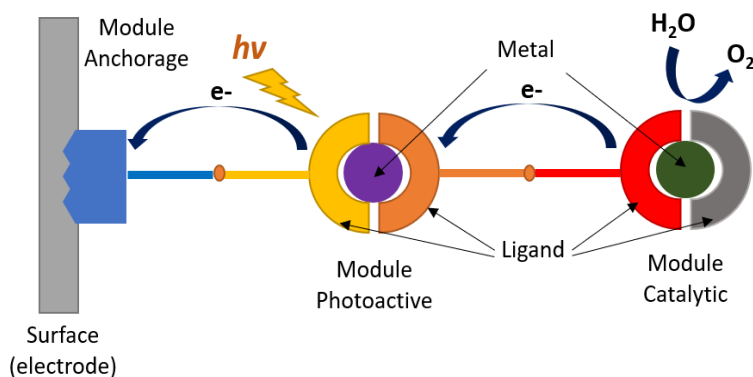


Figure 4-1 modular device for photo-oxidation of water

Light-driven activation of a catalyst in intramolecular systems has gained a considerable attention in recent years and the main aim is to attach such complexes to electrode surfaces and use them as photoanode or photocathode in photoelectrochemical cells.^[25,26] Fig. 4-1 shows the simple diagram of a modular device for photo-oxidation of water. A chromophore, as a photo-active module is able to transform light energy into redox equivalents by photo-induced electron transfer to a catalyst. The final target in artificial photosynthesis study is to perform the water splitting reaction. Many studies have investigated the water oxidation catalysis chemically by using polynuclear manganese complexes with large amounts of oxidizing agents.^[112,113] In these reactions, their mechanisms and the origin of the oxygen atoms were not clearly revealed. An elegant way to decipher the multielectronic activation pathways consists in studying the

sequential one electron processes photochemically. Several studies have been performed along this line with ruthenium chromophores linked to metal complexes.^[114,115]

In this section, we described the synthesis, characterization and photophysical studies of different Ru-Mn assemblies incorporating a photosensitizer and a manganese complex. The ligand surrounding the manganese ion was designed to wrap up the metal ion in a pentacoordinated fashion leaving a free site for a water molecule as substrate. The goal in this study is to unveil the light induced activation of the bound water molecule to generate an active metal oxo species that can ultimately perform an oxidation reaction. We have to point out the manganese (III)-OH complex with this ligand set was reported before in our lab.^[120] We found that a manganese (IV)-oxo type could be generated electrochemically.^[120] In addition, non-oxidizable mono zinc complex was inserted in place of manganese to serve as a reference.

4.2. Synthesis and Characterizations

4.2.1. Synthesis of Ru^{II}LMn^{III}

For the synthesis of the compound, all procedures were done by Dr. Shyamal Das. The characterizations of NMR are presented in Annex. The synthetic pathway of the represented dyad, abbreviated as Ru^{II}LMn^{III} (**6**), is described in scheme 4-2.

The reaction between 1,10-Phenanthroline-5,6-dione (**1**) with 3-tertiary butyl p-hydroxy benzaldehyde was done via a Steck–Day reaction.^[116] From this the 3-tertiary butyl phenol precursor (**2**) to 3-tertiary butyl salicylaldehyde analogues (**3**) was prepared by a modified Duff reaction. Synthesis of the ligand (**L**, **4**) was performed by condensation of (**3**) with the dipicodolyl ethyl amine, which had been obtained by the reaction of the dipicodolyl amine and N-(2-bromoethyl) phthalimide. Formation of (**5**) was achieved by coordination of Ru(bpy)₂Cl₂ to the phenanthroline end of (**4**).^[117] Target compound (**6**) was obtained by insertion of manganese (II) cation inside the five dentated coordination site of the ligand, **L**. Mn^{II} was oxidized to its Mn^{III} state by air oxidation. In addition, for these two different chromophore structures, zinc derivatives, abbreviated Ru^{II}LZn^{II} (**7**) was synthesized.

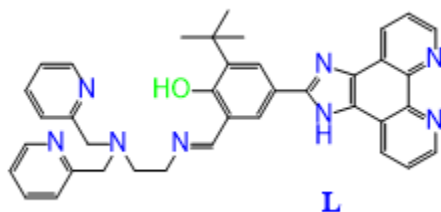
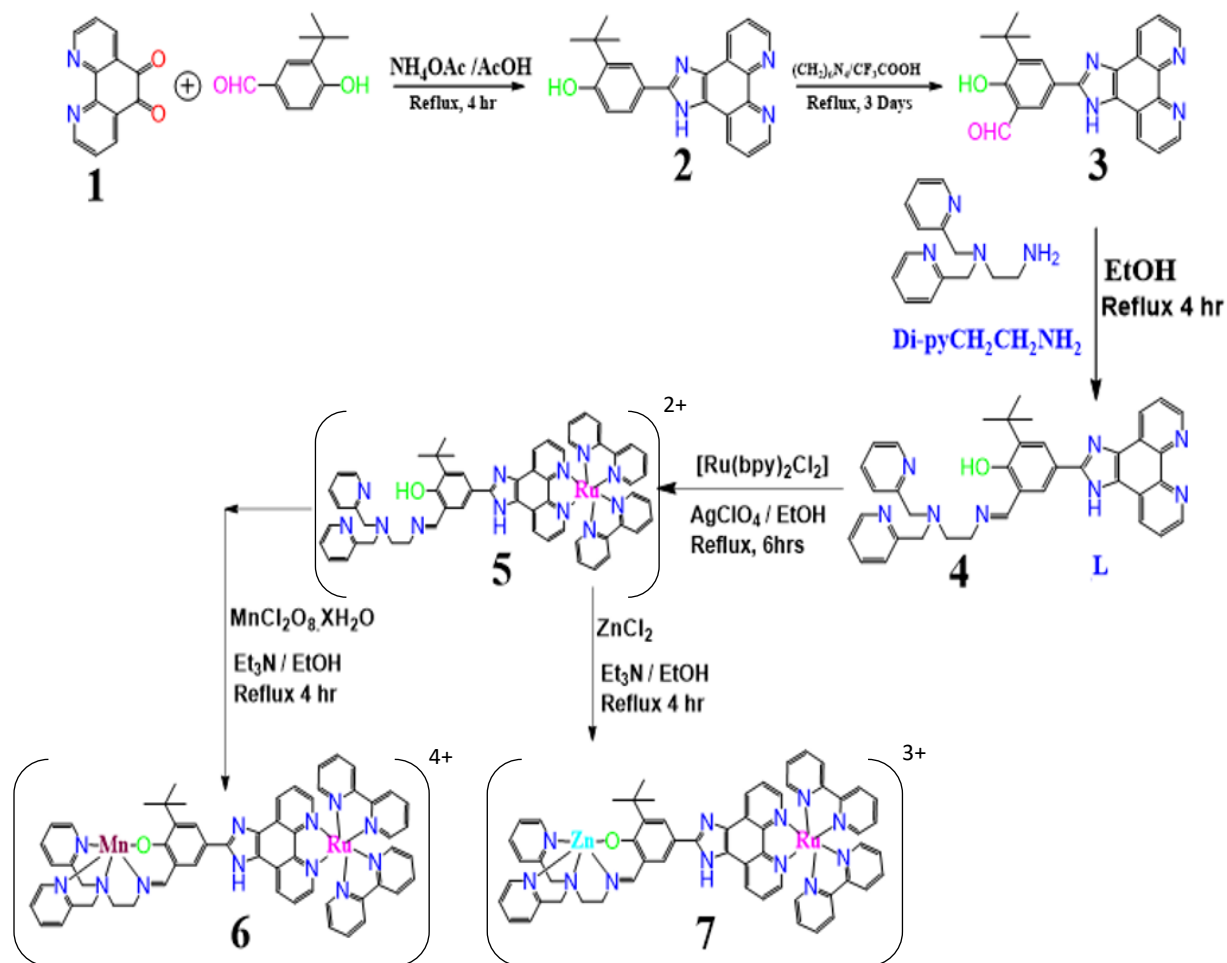


Figure 4-2 Chemical structure of ligand (L).



Scheme 4-1 Synthetic pathway for the formation of $\text{Ru}^{\text{II}}\text{LMn}^{\text{III}}$ (**6**), $\text{Ru}^{\text{II}}\text{LZn}^{\text{II}}$ (**7**).

4.2.2. Characterizations

A) Cyclic Voltammetry (CV)

Electrochemical properties of Ru^{II}L (**5**) and different complexes, Ru^{II}LMn^{III} (**6**) and Ru^{II}LZn^{II} (**7**) were investigated by cyclic voltammetry in acetonitrile solutions. Redox behavior in acetonitrile with reference to the SCE (-0.292 vs. Ag/AgClO₄) are shown in Fig. 4-3 and Table 4-1.

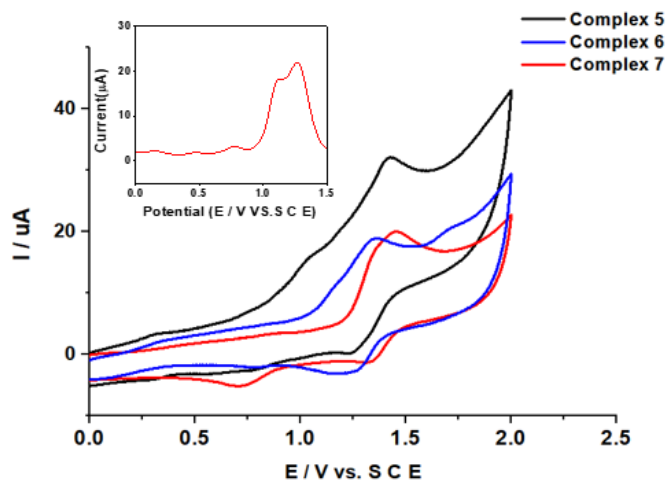


Figure 4-3 CV of 1 mM solutions of Ru^{II}L (**5**), Ru^{II}LMn^{III} (**6**) and Ru^{II}LZn^{II} (**7**) containing 0.1 M TBAPF₆ as supporting electrolyte in acetonitrile. DPV of Ru^{II}LMn^{III} (**6**) (inset). GCE (WE), Pt (CE), E / V vs. SCE. $\nu = 100 \text{ mVs}^{-1}$.

Table 4-1 Electrochemical data for 1 mM solutions of Ru^{II}L (**5**), Ru^{II}LMn^{III} (**6**) and Ru^{II}LZn^{II} (**7**) containing 0.1 M TBAPF₆ as supporting electrolyte in acetonitrile. GCE (WE), Pt (CE), E / V vs. SCE. $\nu = 100 \text{ mVs}^{-1}$.

Complexes	$E_{1/2}(\text{Ru}^{\text{III/II}})$	$E_{1/2} = \text{Mn}^{\text{III}} / \text{Mn}^{\text{IV}}$	$E_{1/2}(\text{Ligand})$	$E_{1/2}(\text{bipyridines})$
Ru ^{II} L (5)	1.28	--	0.95	-0.65,-0.85,-1.02,-1.41,-1.64
Ru ^{II} LMn ^{III} (6)	1.24	0.82	1.05	-0.81,-1.45
Ru ^{II} LZn ^{II} (7)	1.25		0.76	-0.81,-1.45

CV of Ru^{II}LMn^{III} (**6**) in acetonitrile shows two quasi-reversible waves at 1.24 V and 0.82 V (vs. SCE) that were attributed to the Ru^{II}/Ru^{III} and Mn^{III}/Mn^{IV} couples, respectively. The electrochemical results indicate a driving force of 0.42 eV to oxidize the Mn (III) ion by the covalently linked Ru(III)-chromophore which is generated by the absorption of visible light in the presence of electron acceptor.

B) Absorption spectra of complexes and their emission properties

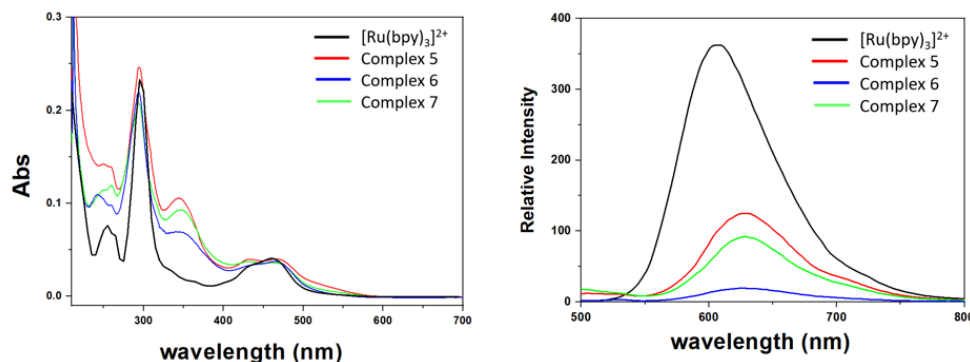


Figure 4-4 Ground state absorption (left) and emission (right) spectra in acetonitrile for Ru^{II}L (5), Ru^{II}LMn^{III} (6) and Ru^{II}LZn^{II} (7) and their emission.

Fig. 4-4 shows the absorption spectra of [Ru(bpy)₃]²⁺ and the complexes Ru^{II}LMn^{III} (**6**) and Ru^{II}LZn^{II} (**7**). The attachment of salen moiety covalently with the ruthenium(II)-polypyridyl chromophore yields Ru^{II}L (**5**) that indicates $\pi \rightarrow \pi^*$ and $n \rightarrow \pi^*$ ligand centered transitions at 282, 312 nm respectively and the broad MLCT band at 462 nm. Ru^{II}LMn^{III} (**6**) shows ligand field transitions at 272, 312 and 333 nm in the ultraviolet region and a broad MLCT band at 463 nm in the visible region similar to (**5**). The absorption spectrum of the Ru^{II}LMn^{III} (**6**), shows a strong absorption around 295 nm due to a π - π^* transition, another band at 348 nm which results from an intraligand charge transfer, and finally a band at 455 nm, the typical MLCT band of ruthenium complexes. In the case of the dinuclear complexes Ru-Mn (**6**), the yield of emission is decreased. This quenching process, which has been detected by several groups, has been described as an energy transfer process between ruthenium and manganese.

Table 4-2 Summary of absorption and emission spectral data of complexes RuL (5), Ru^{II}LMn^{III} (6) and Ru^{II}LZn^{II} (7) in acetonitrile.

Complexes	Absorption λ_{\max} , nm	Emission, λ_{\max} , nm
Ru ^{II} L (5)	234, 282, 312, 415, 462	628
Ru ^{II} LMn ^{III} (6)	272, 312, 333, 463	628
Ru ^{II} LZn ^{II} (7)	259, 294, 347, 430, 467	628

When pentadentate ligand is attached with pyridine part, the emission maximum is 628 nm (Table 4-2). This shift of emission wavelength may be attributed to the presence of the higher extent of conjugation. The bimetallic complexes Ru^{II}LMn^{III} (**6**) and Ru^{II}LZn^{II} (**7**) show same emission peaks at 628 nm in acetonitrile.

4.2.3. Photophysical Studies : Laser Flash Photolysis

The study of Laser Flash Photolysis (LFP) was to focus on internal electron transfer between the excited chromophore part and the catalytic part leading to activation of the Mn ion in presence of electron acceptors under the different pH conditions.

A) Ru^{II}L

The photo-induced electron-transfer process in the complex was studied by the laser flash photolysis. Transient absorption spectroscopy was performed to follow the internal electron transfer between the excited chromophore part and the catalytic part leading to activation of the Mn ion. First, the ruthenium(II)-polypyridiyl chromophore holding the covalently linked 'salen-type' ligand Ru^{II}L (**5**) was studied. As mentioned in the characterization part (4.2.2), the emission maximum of Ru^{II}L (**5**) shows typical emission decay at 628 nm in ACN and the excited state lifetime was about 1.1 μ s that corresponds to the ³MLCT transition. Fig. 4-7 shows transient absorption spectra of Ru^{II}L (**5**) in the range 30 μ s to 300 μ s in presence of methylviologen as a reversible electron acceptor.

Fig. 4-5 shows transient absorption spectra of Ru^{II}L (**5**) in presence of reversible electron acceptors MV²⁺ (left) and RH³⁺ (right). The reduction of MV²⁺ to MV^{•+} is observed at 400 nm and 605 nm, the characteristic absorptions bands for MV^{•+} radical.^[90] While irradiating in the presence of ruthenium(III) hexaammine (RH³⁺) provides a more clear optical properties of the oxidized species. The absorption peaks appeared at 410 nm, 460 nm and broad band around 800 nm.

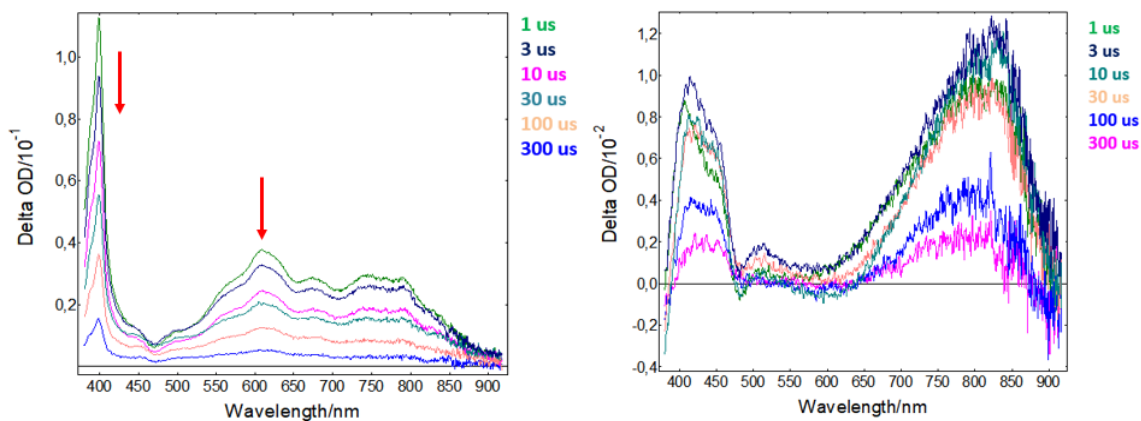


Figure 4-5 Transient absorption spectra of Ru^{II}L (**5**) in presence of MV²⁺ (left) in ACN and RH³⁺ (right) in ACN+H₂O in the range 1 μ s to 300 μ s after laser flash excitation at 460 nm.

B) Ru^{II}LMn^{III}

Fig. 4-6 shows representative profiles of typical emission decay at 628 nm with lifetime of 1.2 μ s in ACN for the compound Ru^{II}LMn^{III} (**6**) and oxidative quenching in presence of electron acceptor. Table 4-3 shows the summary of the quenching effect with diverse electron acceptors and good quenching is observed with methyl viologen (MV²⁺) and ruthenium hexamine (RH³⁺).

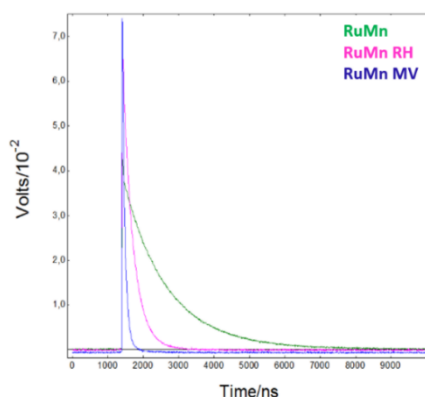


Figure 4-6 Emission kinetics at 628 nm of Ru^{II}LMn^{III} (**6**), Ru^{II}LMn^{III} (**6**) in presence of RH³⁺ (pink) in ACN +H₂O (50:50) and Ru^{II}LMn^{III} (**6**) in presence of MV²⁺ (blue) in ACN

Table 4-3 Emission kinetics at 628 nm of Ru-Mn with different electron acceptors; Ar-purged, excitation wavelength 460 nm.

	RuMn (O.D = 0.5, 35 μ M)			
Electron acceptor	-	MV(PF ₆) ₂	[Ru(NH ₃) ₆]Cl ₃	[Co ^{III} (NH ₃) ₅ Cl]Cl ₂
Concentration		10 mM	10 mM	10 mM
Life time (τ)	1224 ns	75 ns	290 ns	1170 ns
Results		good quenching	good quenching	Not good candidate

As shown in Fig. 4-6 and Table 4-3, in presence of MV²⁺ as an electron acceptor, quenching occurred decreasing the excited state lifetime of Ru^{II*} from 1224 ns to 75 ns. The formation of MV⁺ was detected by the characteristic absorption bands at 400 nm and 605 nm.^[90] The initially formed Ru^{III} state decays quickly (< 150 ns) and after 100 μ s the MV⁺ has also disappeared as shown in Fig. 4-10. The disappearance of the MV⁺ and recovery of the Ru(II) state of the chromophore give rise to new absorption features, maxima at 400 nm and broad band around 770 nm. These oxidized species do not correspond to the absorption peaks of Mn^{IV} species. however, this clearly evidenced an efficient activation of certain species to the oxidized form by the photo-oxidized chromophore. In another experiment we used a different electron acceptor,

RH^{3+} . The quenching process in presence of RH^{3+} occurred in 290 ns and after 1 μs , absorption peaks appeared at 410 nm, 460 nm and broad band around 800 nm. These two different electron acceptors both lead a species presenting absorption peak around 800 nm. Based on the work of Fujii, the observed bands can be assigned to generation of Mn^{III} -phenoxy radical species.^[118,119]

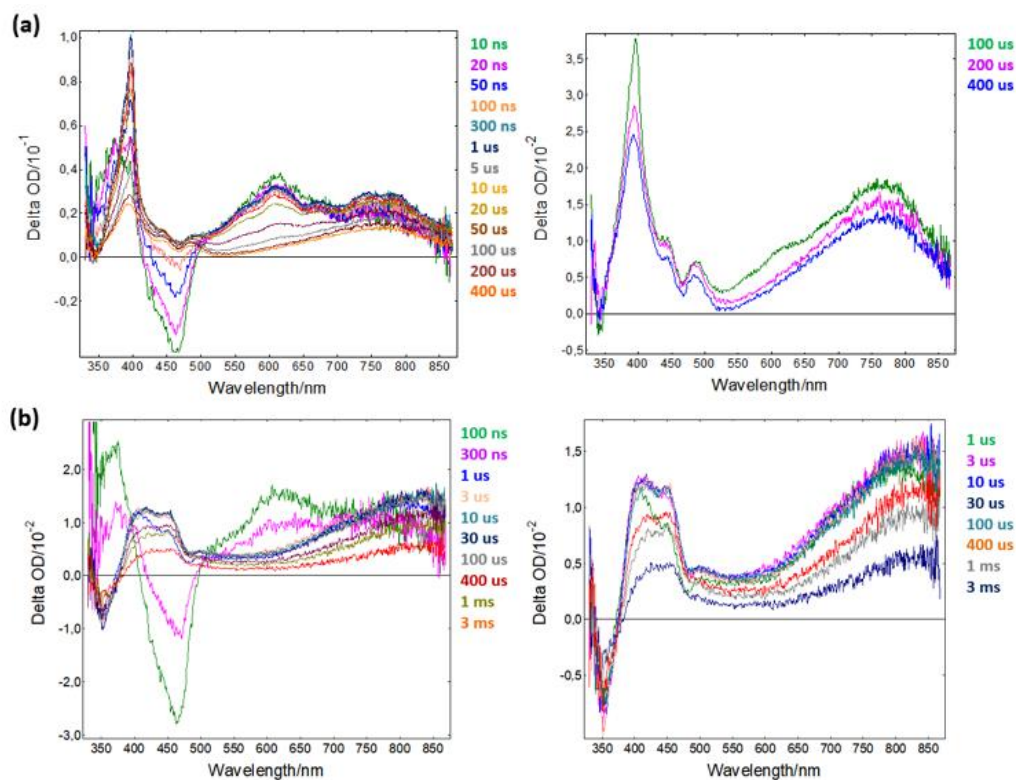


Figure 4-7 Transient absorption spectra of $\text{Ru}^{\text{II}}\text{LMn}^{\text{III}}$ (6) (a) in presence of MV^{2+} in ACN, recorded from 10 ns to 400 μs (left) and 100 μs to 400 μs (right) (b) in presence of RH^{3+} in ACN+ H_2O , recorded from 100 ns to 3 ms (left) and 1 μs to 3 ms (right), after excitation at 460 nm.

C) Ru^{II}LZn^{II}

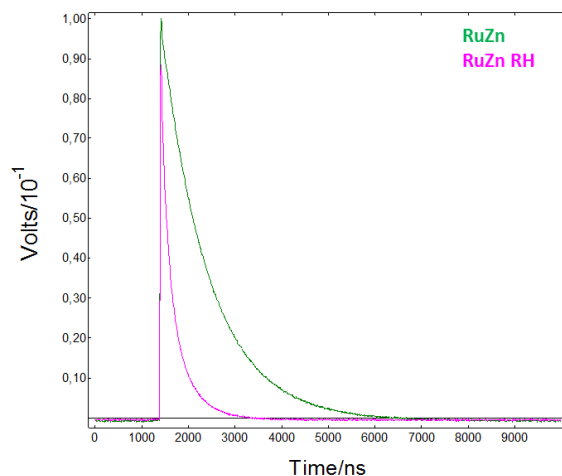


Figure 4-8 Emission kinetics at 628 nm of Ru^{II}LZn^{III} (7) and Ru^{II}LZn^{II} (7) in presence of RH³⁺ in ACN+H₂O (50:50)

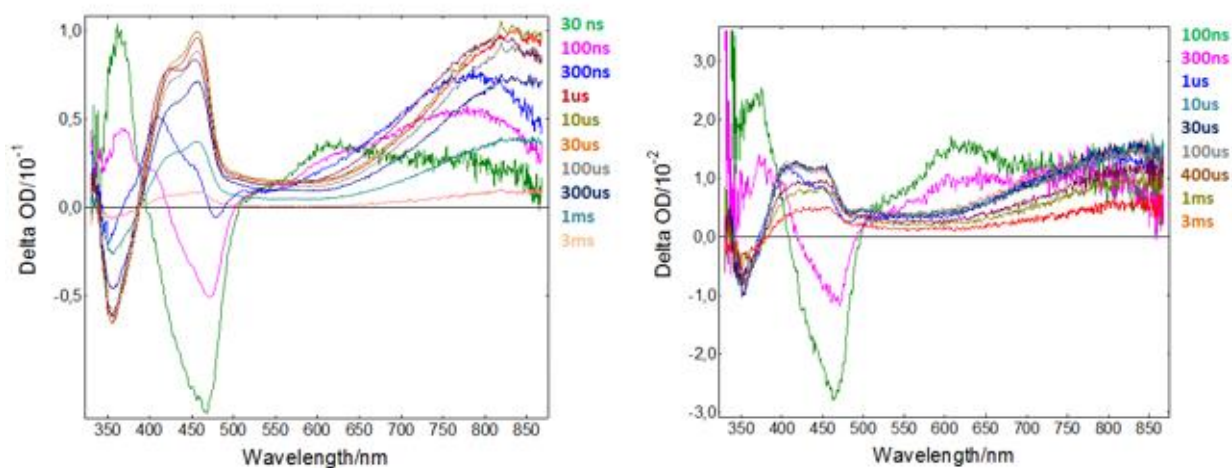


Figure 4-9 Transient absorption spectra of Ru^{II}LZn^{II} (7) in presence of RH³⁺ in ACN+H₂O (left) and Ru^{II}LMn^{III} (6) in presence of RH³⁺ in ACN+H₂O (right) in the range 30 ns to 3 ms after laser flash excitation at 460 nm.

The complex Ru^{II}LZn^{II} (**7**), which contains zinc ion rather than manganese was also investigated in presence of RH³⁺. The purpose of study Ru^{II}LZn^{II} (**7**) was to compare the photophysical events with those of Ru^{II}LMn^{III} (**6**). Based on the electrochemical properties of the Ru^{II}LZn^{II} (**7**) complex, an oxidation wave was observed prior the Ru^{III/II} couple. This wave was assigned to the oxidation of the ligand surround the Zn (II) ion. Henceforth, it was obvious for us to interrogate the electron transfer event in this system where the zinc (II) ion is redox inactive. Fig. 4-8 shows the quenching from 1017 ns to 119 ns at the emission wavelength of Ru^{II/III*}, 628 nm in presence of RH³⁺ as an electron acceptor.

In Fig. 4-9 we compare the absorbance spectra between $[\text{Ru}^{\text{II}}\text{LZn}^{\text{II}}]^{\text{ox}}$ and $[\text{Ru}^{\text{II}}\text{LMn}^{\text{III}}]^{\text{ox}}$ obtained after light excitation in presence of RH^{3+} . After 30 μs , they have similar spectra. To observe the band at high wavelength, we blocked the blue range by using filter and after 300 ns it is obvious that the peak at 840 nm shifted to 783 nm as shown in Fig. 4-10.

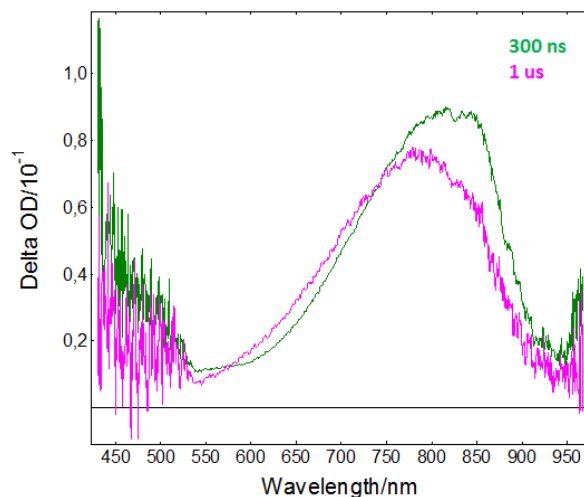


Figure 4-40 Transient absorption spectra of $\text{Ru}^{\text{II}}\text{LZn}^{\text{II}}$ (**7**) in presence of RH in $\text{ACN}+\text{H}_2\text{O}$ in the range 300 ns and 1 μs blocking blue range by filter.

Interestingly, in presence of RH^{3+} , the results give similar spectra as $\text{Ru}^{\text{II}}\text{LMn}^{\text{III}}$ (**6**) and $\text{Ru}^{\text{II}}\text{LZn}^{\text{II}}$ (**7**), indicating that the oxidized species is formed on the ligand and not on the metal in the pentadendate cavity.

4.3. Conclusions & Perspectives

We have studied intramolecular electron transfer from manganese to ruthenium-based photosensitizer. We could induce the intramolecular oxidation by visible light absorption of photosensitizer component.

In presence of ruthenium hexamine as electron acceptor, the results of transient spectra for $\text{Ru}^{\text{II}}\text{L}$, $\text{Ru}^{\text{II}}\text{LMn}^{\text{III}}$, and $\text{Ru}^{\text{II}}\text{LZn}^{\text{II}}$ were similar. It indicates that the oxidized species is formed on the ligand, which is probably a phenoxyl radical species.^[118,119] Therefore, to investigate the oxidized form, X-band EPR technique might be useful.

Studies on different pH solutions is another challenge to examine the reactivity of photogeneration. The bridging ligands, imidazole may participate to the electron transfer depending on the pH conditions. Employing organic compound as substrate will be the further study to demonstrate the photochemical generation of catalytic center.

These are preliminary results and the work is in progress to study in depth.

References

- [1] N. Cox, M. Retegan, F. Neese, D. A. Pantazis, A. Boussac, W. Lubitz, *Science* **2014**, *345*, 804–808.
- [2] N. Cox, D. A. Pantazis, F. Neese, W. Lubitz, *Acc. Chem. Res.* **2013**, *46*, 1588–1596.
- [3] X.-G. Zhu, S. P. Long, D. R. Ort, *Current Opinion in Biotechnology* **2008**, *19*, 153–159.
- [4] Y. Umena, K. Kawakami, J.-R. Shen, N. Kamiya, *Nature* **2011**, *473*, 55.
- [5] F. R. WHATLEY, K. TAGAWA, D. I. ARNON, *Proc Natl Acad Sci U S A* **1963**, *49*, 266–270.
- [6] L. Hammarström, L. Sun, B. Åkermark, S. Styring, *Biochimica et Biophysica Acta (BBA) - Bioenergetics* **1998**, *1365*, 193–199.
- [7] M.-D. Weitze, *Artificial Photosynthesis-State of Research, Scientific-Technological Challenges and Perspectives*, Acatech – National Academy Of Science And Engineering.
- [8] N. Oreskes, *Science* **2004**, *306*, 1686.
- [9] Lockwood Mike, *Proceedings of the Royal Society A: Mathematical, Physical and Engineering Sciences* **2010**, *466*, 303–329.
- [10] J. Twidell, T. Weir, *Renewable Energy Resources | Taylor & Francis Group*, London: Routledge, **2015**.
- [11] C. Zou, Q. Zhao, G. Zhang, B. Xiong, *Natural Gas Industry B* **2016**, *3*, 1–11.
- [12] P. Richard, *The International Energy Agency SHC Programme Solar Update* **2009**, *50*, 2–3.
- [13] M. Perez, R. Perez, **2015**, *62*, 4.
- [14] W. Lubitz, M. Chrysin, N. Cox, *Photosynthesis Research* **2019**.
- [15] J. P. McEvoy, G. W. Brudvig, *Chem. Rev.* **2006**, *106*, 4455–4483.
- [16] J. P. McEvoy, J. A. Gascon, V. S. Batista, G. W. Brudvig, *Photochem. Photobiol. Sci.* **2005**, *4*, 940–949.
- [17] L. V. Kulik, B. Epel, W. Lubitz, J. Messinger, *J. Am. Chem. Soc.* **2007**, *129*, 13421–13435.
- [18] B. Limburg, E. Bouwman, S. Bonnet, *ACS Catal.* **2016**, *6*, 5273–5284.
- [19] T. Ishizuka, A. Watanabe, H. Kotani, D. Hong, K. Satonaka, T. Wada, Y. Shiota, K. Yoshizawa, K. Ohara, K. Yamaguchi, et al., *Inorg. Chem.* **2016**, *55*, 1154–1164.
- [20] T. J. Wydrzynski, W. Hillier, *Molecular Solar Fuels*, The Royal Society Of Chemistry, **2012**.
- [21] S. Funyu, T. Isobe, S. Takagi, D. A. Tryk, H. Inoue, *J. Am. Chem. Soc.* **2003**, *125*, 5734–5740.
- [22] S. Funyu, M. Kinai, D. Masui, S. Takagi, T. Shimada, H. Tachibana, H. Inoue, *Photochemical & photobiological sciences: Official journal of the European Photochemistry Association and the European Society for Photobiology* **2010**, *9*, 931–936.
- [23] S. Fukuzumi, T. Kishi, H. Kotani, Y.-M. Lee, W. Nam, *Nature Chemistry* **2010**, *3*, 38.
- [24] W. Chen, F. N. Rein, R. C. Rocha, *Angewandte Chemie International Edition* **2009**, *48*, 9672–9675.
- [25] J. A. Treadway, J. A. Moss, T. J. Meyer, *Inorg. Chem.* **1999**, *38*, 4386–4387.
- [26] D. L. Ashford, W. Song, J. J. Concepcion, C. R. K. Glasson, M. K. Brennaman, M. R. Norris, Z. Fang, J. L. Templeton, T. J. Meyer, *J. Am. Chem. Soc.* **2012**, *134*, 19189–19198.
- [27] E. A. Karlsson, B.-L. Lee, R.-Z. Liao, T. Åkermark, M. D. Kärkäs, V. S. Becerril, P. E. M. Siegbahn, X. Zou, M. Abrahamsson, B. Åkermark, *ChemPlusChem* **2014**, *79*, 936–950.
- [28] E. Y. Tsui, R. Tran, J. Yano, T. Agapie, *Nat Chem* **2013**, *5*, 293–299.
- [29] L.-X. Xue, T.-T. Meng, W. Yang, K.-Z. Wang, *Journal of Photochemistry and Photobiology B: Biology* **2015**, *152*, 95–105.
- [30] Z. Yu, F. Li, L. Sun, *Energy Environ. Sci.* **2015**, *8*, 760–775.
- [31] H. Berglund-Baudin, L. Sun, R. Davidov, M. Sundahl, S. Styring, B. Åkermark, M. Almgren, L. Hammarström, *The Journal of Physical Chemistry A* **1998**, *102*, 2512–2518.
- [32] C. Herrero, J. L. Hughes, A. Quaranta, N. Cox, A. W. Rutherford, W. Leibl, A. Aukauloo, *Chemical Communications* **2010**, *46*, 7605.
- [33] C. Herrero, A. Quaranta, R.-A. Fallahpour, W. Leibl, A. Aukauloo, *The Journal of Physical Chemistry C* **2013**, *117*, 9605–9612.

- [34] V. Balzani, N. Sabbatini, F. Scandola, *Chem. Rev.* **1986**, *86*, 319–337.
- [35] M. H. V. Huynh, D. M. Dattelbaum, T. J. Meyer, *Coordination Chemistry Reviews* **2005**, *249*, 457–483.
- [36] D. P. Rillema, C. B. Blanton, R. J. Shaver, D. C. Jackman, M. Boldaji, S. Bundy, L. A. Worl, T. J. Meyer, *Inorg. Chem.* **1992**, *31*, 1600–1606.
- [37] S. Campagna, F. Puntoriero, F. Nastasi, G. Bergamini, V. Balzani, in *Photochemistry and Photophysics of Coordination Compounds I* (Eds.: V. Balzani, S. Campagna), Springer Berlin Heidelberg, Berlin, Heidelberg, **2007**, pp. 117–214.
- [38] A. Juris, V. Balzani, F. Barigelletti, S. Campagna, P. Belser, A. von Zelewsky, *Coordination Chemistry Reviews* **1988**, *84*, 85–277.
- [39] K. Kalyanasundaram, *Coordination Chemistry Reviews* **1982**, *46*, 159–244.
- [40] P. A. Anderson, G. F. Strouse, J. A. Treadway, F. R. Keene, T. J. Meyer, *Inorg. Chem.* **1994**, *33*, 3863–3864.
- [41] J.-P. Collin, R. Kayhanian, J.-P. Sauvage, G. Calogero, F. Barigelletti, A. De Cian, J. Fischer, *Chem. Commun.* **1997**, 775–776.
- [42] J. M. Gonçalves, T. A. Matias, K. C. F. Toledo, K. Araki, in *Advances in Inorganic Chemistry* (Eds.: R. van Eldik, C.D. Hubbard), Academic Press, **2019**, pp. 241–303.
- [43] S. Fukuzumi, D. Hong, *European Journal of Inorganic Chemistry* **2014**, *2014*, 645–659.
- [44] B. M. Hunter, H. B. Gray, A. M. Müller, *Chem. Rev.* **2016**, *116*, 14120–14136.
- [45] A. Singh, S. L. Y. Chang, R. K. Hocking, U. Bach, L. Spiccia, *Energy Environ. Sci.* **2013**, *6*, 579–586.
- [46] D. J. Wasylenko, R. D. Palmer, C. P. Berlinguette, *Chem. Commun.* **2013**, *49*, 218–227.
- [47] C. Panda, J. Debgupta, D. Díaz Díaz, K. K. Singh, S. Sen Gupta, B. B. Dhar, *J. Am. Chem. Soc.* **2014**, *136*, 12273–12282.
- [48] E. A. Karlsson, B.-L. Lee, T. Åkermark, E. V. Johnston, M. D. Kärkäs, J. Sun, Ö. Hansson, J.-E. Bäckvall, B. Åkermark, *Angewandte Chemie International Edition* **2011**, *50*, 11715–11718.
- [49] H.-Y. Wang, E. Mijangos, S. Ott, A. Thapper, *Angewandte Chemie International Edition* **2014**, *53*, 14499–14502.
- [50] S. Nestke, E. Ronge, I. Siewert, *Dalton Transactions* **2018**, *47*, 10737–10741.
- [51] M.-T. Zhang, Z. Chen, P. Kang, T. J. Meyer, *J. Am. Chem. Soc.* **2013**, *135*, 2048–2051.
- [52] R. Ruiz, C. Surville-Barland, A. Aukauloo, E. Anxolabehere-Mallart, Y. Journaux, J. Cano, M. C. Muñoz, *Journal of the Chemical Society, Dalton Transactions* **1997**, 745–752.
- [53] X. Ottenwaelder, R. Ruiz-García, G. Blondin, R. Carasco, J. Cano, D. Lexa, Y. Journaux, A. Aukauloo, *Chem. Commun.* **2004**, 504–505.
- [54] S. M. Barnett, K. I. Goldberg, J. M. Mayer, *Nat Chem* **2012**, *4*, 498–502.
- [55] P. Garrido-Barros, I. Funes-Ardoiz, S. Drouet, J. Benet-Buchholz, F. Maseras, A. Llobet, *J. Am. Chem. Soc.* **2015**, *137*, 6758–6761.
- [56] M. K. Coggins, M.-T. Zhang, Z. Chen, N. Song, T. J. Meyer, *Angewandte Chemie International Edition* **2014**, *53*, 12226–12230.
- [57] T. Zhang, C. Wang, S. Liu, J.-L. Wang, W. Lin, *J. Am. Chem. Soc.* **2014**, *136*, 273–281.
- [58] L. A. Stott, K. E. Prosser, E. K. Berdichevsky, C. J. Walsby, J. J. Warren, *Chem. Commun.* **2017**, *53*, 651–654.
- [59] A. Prevedello, I. Bazzan, N. Dalle Carbonare, A. Giuliani, S. Bhardwaj, C. Africh, C. Cepek, R. Argazzi, M. Bonchio, S. Caramori, et al., *Chemistry – An Asian Journal* **2016**, *11*, 1281–1287.
- [60] S. J. Koepke, K. M. Light, P. E. VanNatta, K. M. Wiley, M. T. Kieber-Emmons, *J. Am. Chem. Soc.* **2017**, *139*, 8586–8600.
- [61] R. A. Marcus, *The Journal of Physical Chemistry B* **1998**, *102*, 10071–10077.
- [62] N. Bjerrum, *Danske Vid. Selskab, Math.-fys. medd* **1926**, *7*, 1–48.
- [63] M. Szwarc, *Ions and Ion Pairs in Organic Reactions*, Wiley- Interscience, **1972**.
- [64] K. Y. L. G, S. Michael, *Journal of the American Chemical Society* **1971**, *93*, 4614.

- [65] C. Reichardt, *Solvent and Solvent Effects in Organic Chemistry*, VCH: New York, **1988**.
- [66] J. H. Montoya, L. C. Seitz, P. Chakthranont, A. Vojvodic, T. F. Jaramillo, J. K. Nørskov, *Nature Materials* **2017**, *16*, 70–81.
- [67] N. S. Lewis, D. G. Nocera, *Proceedings of the National Academy of Sciences* **2006**, *103*, 15729–15735.
- [68] V. Balzani, A. Credi, M. Venturi, *ChemSusChem* **2008**, *1*, 26–58.
- [69] T. R. Simmons, G. Berggren, M. Bacchi, M. Fontecave, V. Artero, *Coordination Chemistry Reviews* **2014**, *270–271*, 127–150.
- [70] H. Takeda, C. Cometto, O. Ishitani, M. Robert, *ACS Catal.* **2017**, *7*, 70–88.
- [71] H. Dau, A. Grundmeier, P. Loja, M. Haumann, *Philos. Trans. Royal Soc. B* **2008**, *363*, 1237–1243.
- [72] M. D. Kärkäs, O. Verho, E. V. Johnston, B. Åkermark, *Chem. Rev.* **2014**, *114*, 11863–12001.
- [73] S. W. Gersten, G. J. Samuels, T. J. Meyer, *J. Am. Chem. Soc.* **1982**, *104*, 4029–4030.
- [74] C. W. Chronister, R. A. Binstead, J. Ni, T. J. Meyer, *Inorg. Chem.* **1997**, *36*, 3814–3815.
- [75] J. F. Hull, D. Balcells, J. D. Blakemore, C. D. Incarvito, O. Eisenstein, G. W. Brudvig, R. H. Crabtree, *J. Am. Chem. Soc.* **2009**, *131*, 8730–8731.
- [76] K. S. Joya, N. K. Subbaiyan, F. D'Souza, H. J. M. de Groot, *Angew. Chem., Int. Ed.* **2012**, *51*, 9601–9605.
- [77] J. S. Kanady, E. Y. Tsui, M. W. Day, T. Agapie, *Science* **2011**, *333*, 733.
- [78] C. Zhang, C. Chen, H. Dong, J.-R. Shen, H. Dau, J. Zhao, *Science* **2015**, *348*, 690.
- [79] M.-T. Zhang, Z. Chen, P. Kang, T. J. Meyer, *J. Am. Chem. Soc.* **2013**, *135*, 2048–2051.
- [80] J. Serrano-Plana, I. Garcia-Bosch, A. Company, M. Costas, *Acc. Chem. Res.* **2015**, *48*, 2397–2406.
- [81] P. Garrido-Barros, C. Gimbert-Suriñach, D. Moonshiram, A. Picón, P. Monge, V. S. Batista, A. Llobet, *J. Am. Chem. Soc.* **2017**, *139*, 12907–12910.
- [82] R. Ruiz, C. Surville-Barland, A. Aukauloo, E. Anxolabehere-Mallart, Y. Journaux, J. Cano, M. C. Muñoz, *Dalton Trans.* **1997**, 745–752.
- [83] F. C. Anson, T. J. Collins, T. G. Richmond, B. D. Santarsiero, J. E. Toth, B. G. R. T. Treco, *J. Am. Chem. Soc.* **1987**, *109*, 2974–2979.
- [84] S. W. Gordon-Wylie, B. L. Claus, C. P. Horwitz, Y. Leychikis, J. M. Workman, A. J. Marzec, G. R. Clark, C. E. F. Rickard, B. J. Conklin, S. Sellers, et al., *Chem. Eur. J.* **1998**, *4*, 2173–2181.
- [85] J. J. Steggerda, J. J. Bour, P. J. M. W. L. Birker, *Inorg. Chem.* **1971**, *10*, 1202–1205.
- [86] J. Soto, R. Martinez-Manez, J. Paya, F. Lloret, M. Julve, *Transition Metal Chemistry* **1993**, *18*, 69–72.
- [87] F. Lloret, J. Sletten, R. Ruiz, M. Julve, J. Faus, M. Verdagner, *Inorg. Chem.* **1992**, *31*, 778–784.
- [88] H. Ojima, K. Nonoyama, *Coordination Chemistry Reviews* **1988**, *92*, 85–111.
- [89] F. Lloret, M. Julve, J. Faus, Y. Journaux, M. Philoche-Levisalles, Y. Jeannin, *Inorg. Chem.* **1989**, *28*, 3702–3706.
- [90] T. Watanabe, K. Honda, *J. Phys. Chem.* **1982**, 2617.
- [91] N. Chitose, J. A. LaVerne, Y. Katsumura, *J. Phys. Chem. A* **1998**, 2087.
- [92] M. Borja, P. K. Dutta, *Nature* **1993**, *362*, 43–45.
- [93] X. ZHU, M. HUANG, J. LI, H. HE, X. ZHANG, S. WANG, *Analytical Sciences* **2017**, *33*, 585–590.
- [94] S. H. Kang, Y.-M. Jeon, K. Kim, S. Houbrechts, E. Hendrickx, A. Persoons, *J. Chem. Soc., Chem. Commun.* **1995**, 635–636.
- [95] E. Pizzolato, M. Natali, B. Posocco, A. Montellano López, I. Bazzan, M. Di Valentin, P. Galloni, V. Conte, M. Bonchio, F. Scandola, et al., *Chem. Commun.* **2013**, *49*, 9941–9943.
- [96] M. D. Kärkäs, T. Åkermark, E. V. Johnston, S. R. Karim, T. M. Laine, B.-L. Lee, T. Åkermark, T. Privalov, B. Åkermark, *Angewandte Chemie International Edition* **2012**, *51*, 11589–11593.
- [97] J.-M. Lehn, R. Ziessel, *Proc Natl Acad Sci USA* **1982**, *79*, 701.
- [98] C. Zoski, *Handbook of Electrochemistry - 1st Edition*, Elsevier Science, **2007**.
- [99] A. J. Bard, L. R. Faulkner, *Electrochemical Methods: Fundamentals and Applications*, John Wiley & Sons, **2006**.

- [100] N. Elgrishi, K. J. Rountree, B. D. McCarthy, E. S. Rountree, T. T. Eisenhart, J. L. Dempsey, *J. Chem. Educ.* **2018**, *95*, 197–206.
- [101] A. de Aguirre, P. Garrido-Barros, I. Funes-Ardoiz, F. Maseras, *European Journal of Inorganic Chemistry* **2019**, DOI 10.1002/ejic.201801534.
- [102] C. Costentin, J.-M. Savéant, *ChemElectroChem* **2014**, *1*, 1226–1236.
- [103] C. Costentin, S. Drouet, M. Robert, J.-M. Savéant, *J. Am. Chem. Soc.* **2012**, *134*, 11235–11242.
- [104] O. Poizat, C. Sourisseau, J. Corset, *Journal of Molecular Structure* **1986**, *143*, 203–206.
- [105] V. Novakovic, M. Z. Hoffman, *Journal of the American Chemical Society* **1987**, *109*, 2341–2346.
- [106] Farhana Haque, MS Rahman, Etmina Ahmed, PK Bakshi, AA Shaikh, *DUJS* **2013**, *61*.
- [107] E. M. Kosower, J. L. Cotter, *Journal of the American Chemical Society* **1964**, *86*, 5524–5527.
- [108] K. Kim, N. Selvapalam, Y. H. Ko, K. M. Park, D. Kim, J. Kim, *Chem. Soc. Rev.* **2007**, *36*, 267–279.
- [109] V. Van Even, M. C. Haulait-Pirson, *Journal of Solution Chemistry* **1977**, *6*, 757–770.
- [110] J. Peisach, W. E. Blumberg, *Archives of Biochemistry and Biophysics* **1974**, *165*, 691–708.
- [111] B. Bennett, J. M. Kowalski, *Methods Enzymol* **2015**, *563*, 341–361.
- [112] A. K. Poulsen, A. Rompel, C. J. McKenzie, *Angewandte Chemie International Edition* **2005**, *44*, 6916–6920.
- [113] W. Rüttinger, G. C. Dismukes, *Chem. Rev.* **1997**, *97*, 1–24.
- [114] L. Hammarstrom, *Current Opinion in Chemical Biology* **2003**, *7*, 666–673.
- [115] M. D. Kärkäs, T. Akermark, E. V. Johnston, S. R. Karim, T. M. Laine, B.-L. Lee, T. Akermark, T. Privalov, B. Akermark, *Angewandte Chemie (International ed. in English)* **2012**, *51*, 11589–11593.
- [116] C. Hiort, P. Lincoln, B. Norden, *J. Am. Chem. Soc.* **1993**, *115*, 3448–3454.
- [117] G. Sprintschnik, H. W. Sprintschnik, P. P. Kirsch, D. G. Whitten, *J. Am. Chem. Soc.* **1976**, *98*, 2337–2338.
- [118] T. Kurahashi, A. Kikuchi, T. Tosha, Y. Shiro, T. Kitagawa, H. Fujii, *Inorg. Chem.* **2008**, *47*, 1674–1686.
- [119] T. Kurahashi, A. Kikuchi, Y. Shiro, M. Hada, H. Fujii, *Inorg. Chem.* **2010**, *49*, 6664–6672.
- [120] S. El Ghachtouli, B. Lassalle-Kaiser, P. Dorlet, R. Guillot, E. Anxolabéhère-Mallart, C. Costentin, A. Aukauloo, *Energy Environ. Sci.* **2011**, *4*, 2041–2044.

Annex.

Annex

(A) Experimental part

A.1. Electrochemistry

A.1.1 Cyclic Voltammetry

Cyclic voltammetry (CV) is a transient technique in which the potential is scanned between two limiting values (Fig. A-1) and the resulting current crossing the system measured, giving rise to graphs named cyclic voltammograms ($I = f(E)$). Cyclic voltammetry has become a very popular technique for initial electrochemical studies of new systems and has proven useful in obtaining information about complicated electrode reactions.

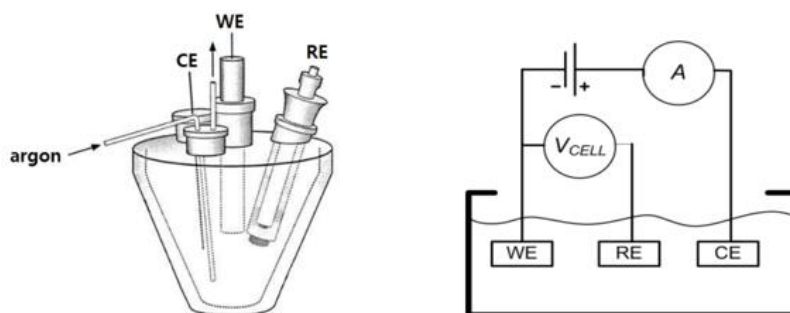


Figure A-1 Electrochemical cell for cyclic voltammetry.

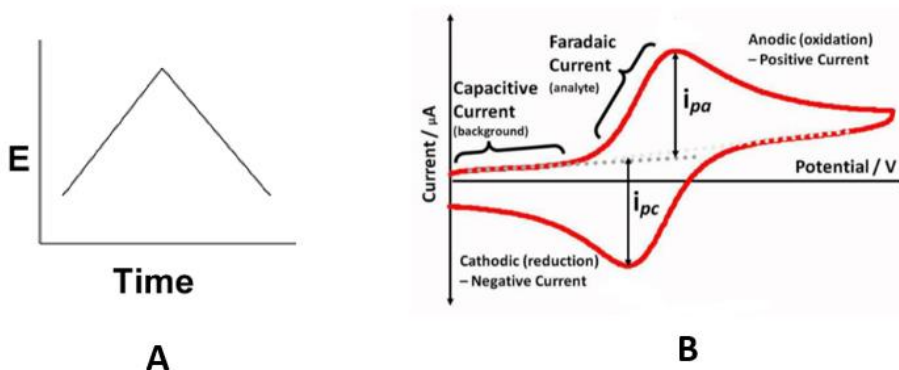


Figure A-2 (A) Cyclic potential sweep ramp, (B) Resulting cyclic voltammogram.

A potentiostat from AUTOLAB 204, controlled by the NOVA 1.10 software, was used for cyclic voltammetry (CV), Differential Potential Voltammetry (DPV) and Chronoamperometry (CA). A conventional three-electrode compartment cell was used. The working electrode was a glassy carbon electrode, GCE (diameter = 3mm, area = 0.07 mm², Fig. A-3), the reference electrode was a silver-silver chloride electrode (Ag/AgCl) for aqueous solution, silver-silver nitrate electrode (Ag/AgNO₃) for non-aqueous solution and Saturated Calomel Electrode (SCE) for both aqueous and non-aqueous solution. The counter electrode was a platinum electrode. All studies were carried out at room temperature and kept under an argon flow. Most of the CVs were obtained under the following experimental conditions: a scan rate of 100 mVs⁻¹. The GCE was conditioned by a polishing procedure using diamond pastes of 6, 3 and 1 μm on a micro-cloth polishing pad, and then the electrode was rinsed with ultra-pure water for aqueous experiments and with acetone and ethanol for non-aqueous experiments.

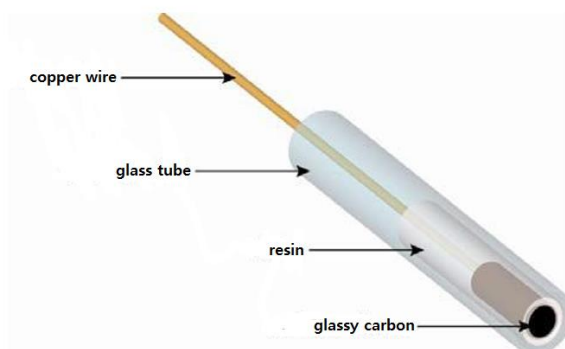


Figure A-3 Glassy carbon electrode

A.1.2 Controlled-Potential Coulometry

Controlled-potential coulometry is based on an exhaustive electrolysis of the analyte in which we apply a constant potential to the electrochemical cell. The analyte is completely oxidized or reduced at the working electrode or that it reacts completely with a reagent generated at the working electrode.

During an electrolysis, the total charge, Q , in coulombs, passing through the electrochemical cell is proportional to the absolute amount of analyte by Faraday's law,

$$Q = nFN_0$$

where n is the overall number of electrons per mole of analyte consumed in the experiment, F is Faraday's constant (96,485 C/mol), and N_0 is the total moles of redox species present. A coulomb is equivalent to an A·sec. Thus, when passing a constant current, i , the total charge is

$$Q = i \times t_e$$

where t_e is the electrolysis time. If the current varies with time, as it does in controlled-potential coulometry, then the total charge is

$$Q = \int_0^{t_e} i(t) dt$$

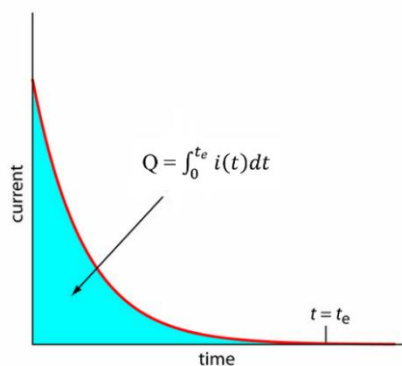


Figure A-4 Total charge area by using CPC

The technique of controlled-potential coulometry (CPC) was used to oxidise H_2O in the presence of the metal complex and an applied potential at which water oxidation occurred. The purpose was to assess the quantity of oxygen involved during water oxidation so that faraday's efficiency could be calculated. The Faraday efficiency (FE) of oxygen evolution is determined according to the expression :

$$\text{Faradaic efficiency} = \frac{O_2 \text{ (measured)}}{O_2 \text{ (theoretical)}} \times 100 \%$$

A.2. UV-Visible Spectrophotometry

Ultraviolet-visible spectroscopy refers to absorption spectroscopy which uses electromagnetic radiations between 210 nm to 900 nm and is divided into the ultraviolet (UV, 200-400 nm) and visible (VIS, 400-900 nm) regions. Since the absorption of ultraviolet or visible radiation by a molecule leads transition among electronic energy levels of the molecule, it is also often called as electronic spectroscopy. The transition that result in the absorption of electromagnetic radiation in this region of the spectrum are transitions between electronic energy levels. As a rule, energetically favored electron promotion will be from the highest occupied molecular orbital (HOMO) to the lowest unoccupied molecular orbital (LUMO), and the resulting species is called an excited state. The particular frequencies at which light is absorbed are affected by the structure and environment of the chromophore (light absorbing species).

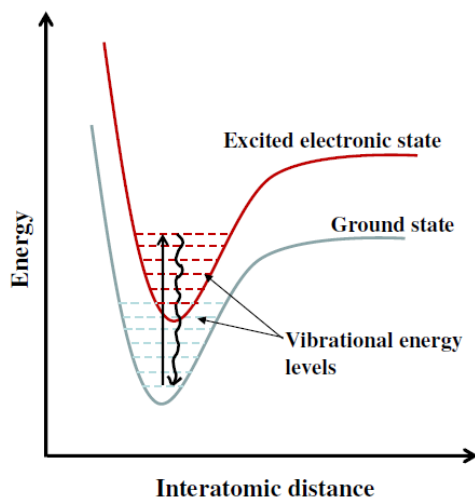


Figure A-5 Energy transition diagram

When sample molecules are exposed to light having an energy that matches a possible electronic transition within the molecule, some of the light energy will be absorbed as the electron is promoted to a higher energy orbital. An optical spectrometer records the wavelengths at which absorption occurs, together with the degree of absorption at each wavelength. The resulting spectrum is presented as a graph of absorbance (A) versus wavelength.

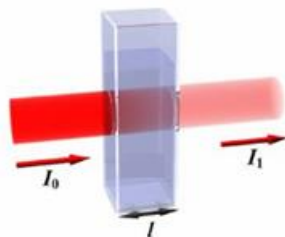


Figure A-6 Absorbance and Beers-Lambert law

The absorption, A is defined as $\log(I_0/I)$, where I_0 is the intensity of the incident light and I is the intensity of the transmitted light. The Beer-Lambert law quantifies the process of absorption. At a given wavelength,

$$A = \epsilon cl$$

Where ϵ is the extinction co-efficient, c is the concentration of the sample in the cuvette and l is the length of the light path through the sample. The extinction co-efficient is a constant for the absorbing species and defines the absorption of the species at a particular wavelength. It is determined by the number and type of chromophores present in each molecule of the absorbing species.

The fundamental characterization of chemicals such as MLCT of $[\text{Ru}(\text{bpy})_3]^{2+}$ and metal complexes were assessed using UV-Visible spectrophotometry (Cary 5000 spectrophotometer) with 1 cm or 1 mm quartz cell. It used to determine ϵ of compounds based on Beer-Lambert law. For kinetic study of ion pair formation between Cu complex and MV^{2+} , mostly kinetic spectra (time drive) technique used.

A.3. Infrared (IR) Spectroscopy

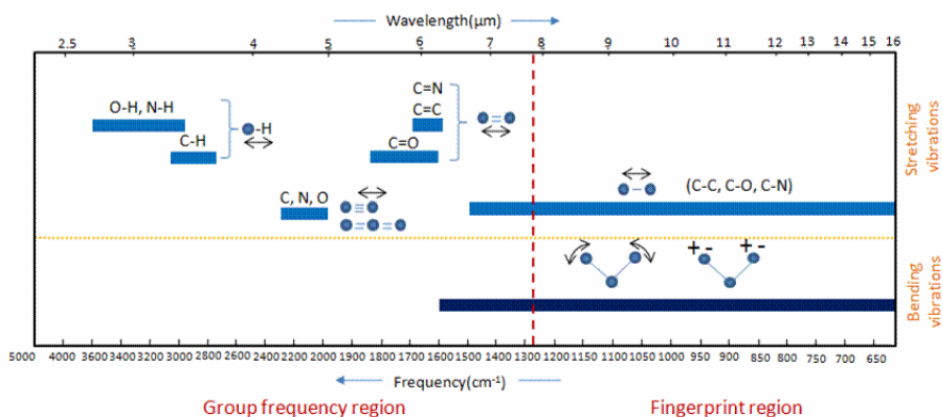


Figure A-7 Infrared functional group diagram

Many functional groups absorb infrared radiation at the certain wavenumber, regardless of the structure of the rest of the molecule. That is, normal way to approach interpretation of an IR spectrum is to identify the functional group region to determine which groups might be present, then to note any unusually strong bands or particularly prominent patterns in the fingerprint region. The group frequency region is from 4000 to 1200 cm^{-1} and the peaks in this region are characteristic of specific kinds of bonds, and therefore can be used to identify whether a specific functional group is present. The region of the infrared spectrum from 1200 to 700 cm^{-1} is called the fingerprint region and is notable for the large number of infrared bands that are found there. Peaks in this region arise from complex deformations of the molecule. They may be characteristic of molecular symmetry, or combination bands arising from multiple bonds deforming simultaneously.

In the experiment, the concentration of the sample in KBr was in 2 %. In this case, I used 100 mg of KBr with 2 mg of samples (MVCl_2 , CuLMV , CuL(TMA)_2). In the pump chamber, pumped until the pressure reaches 10 ton then left for 2 min. After removing the pallet which should be homogenous and transparent in appearance, inserted into the IR sample holder.

A.4. Nuclear magnetic resonance (NMR) Spectroscopy

NMR spectroscopy is useful tool both studying different properties of atomic nuclei and determining the molecular structure of organic compounds.

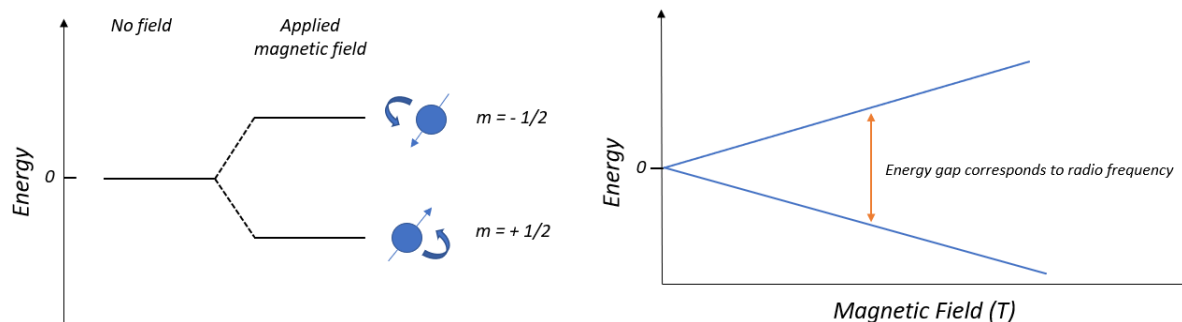


Figure A-8 Charged spins of electron and its energy diagram as function of magnetic field.

Considering electrons have a $+1/2$, $-1/2$ spin, charged spins create a magnetic field (magnetic moment). The nuclei which has half-integer spin such as hydrogen (^1H), ^{13}C isotope of carbon, ^{15}N isotope of nitrogen, ^{19}F isotope of fluorine, and the ^{31}P isotope of phosphorus, all they have magnetic moments that can be detectable by NMR.

For ^1H NMR spectra of organic molecules it can be measured in solution state. In this case, not to interfere from solvent protons, deuterated (deuterium = ^2H , often symbolized as D) solvents are used in NMR. (deuterated water, D_2O , deuterated acetone, $(\text{CD}_3)_2\text{CO}$, deuterated methanol, CD_3OD , deuterated dimethyl sulfoxide, $(\text{CD}_3)_2\text{SO}$, and deuterated chloroform, CDCl_3 .) However, carbon tetrachloride, CCl_4 or carbon disulfide, CS_2 , which don't have hydrogen can be used.

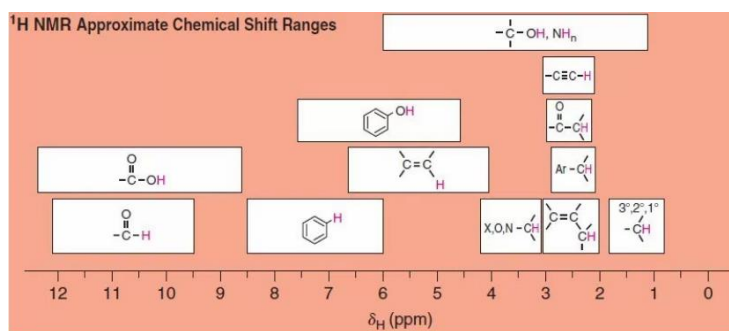


Figure A-9. ^1H NMR Approximate Chemical Shift Ranges

Chemical shift which is the x-axis of an NMR spectrum gives information the structural environments in a molecule. In a ^1H NMR spectrum, the number of signals correspond to the number of distinct proton surroundings. The ^1H NMR chemical shifts generally fall in the range of 13–0 ppm, which is the resonant frequency in a magnetic field. Electron density of molecule affect to the local magnetic environment of nucleus indicates that the actual frequency produced by the nuclei and it gives the NMR signals.

Integration of Signal Area in a ^1H NMR spectrum represents to the number of hydrogen atoms. The height of the integral brings the information of the ratio between the height associated with one and another signal so that it is possible to compare the number of hydrogen atoms in each. Spin-Spin Coupling (signal splitting or signal multiplicity) is another property of ^1H NMR spectra and it gives the information about the structure of a compound. It is due to the magnetic effect of nonequivalent hydrogen atoms. A group of equivalent atoms are split into multiple peaks and a rule 'n+1' explain the number of peaks in a ^1H NMR signal.

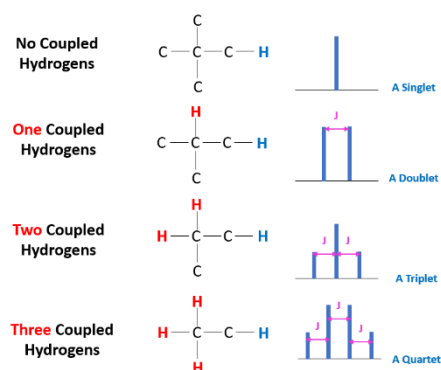


Figure A-10 Spin-spin coupling

In the experiments, mostly ^1H NMR spectra were used for the analysis of ligand OPBI, using deuterated dimethyl sulfoxide, $(\text{CD}_3)_2\text{SO}$ as solvent. The spectra were recorded on AM360 (360 MHz) spectrometers. The chemical shifts δ were described in ppm and coupling constants J were given in hertz (Hz).

A.5. Electron Paramagnetic Resonance (EPR)

Electron paramagnetic resonance spectroscopy (EPR) (or electron spin resonance, ESR) is a spectroscopic technique to study unpaired electrons in chemical species. EPR spectroscopy has a crucial role in organic and inorganic radicals, transition metal complexes, and some biomolecules. Generally, EPR and NMR has similar concept, however in EPR the magnetic moments observe nuclear spins rather than electron spins.

EPR spectrometers analysis the absorption of electromagnetic radiation. A example of the EPR spectra is shown in Fig. A-11. The normal absorption shows as on the above in the figure but usually they present the converted signal to its derivative (on the bottom). In the EPR spectrum, the x-axis represents to the magnetic field with the unit gauss (G) or tesla (T) which is 10000 times of gauss. That is, the peak of absorption spectrum corresponds to the spectrum passes through zero.

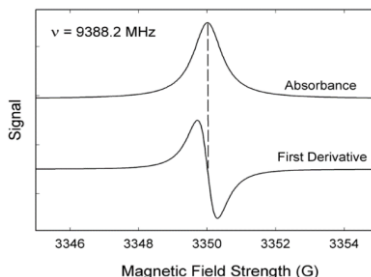


Figure A-11 Comparison of absorption spectrum and EPR spectrum.

Proportionality factor (g-factor) and Hyperfine Interactions

There are 2 main factors in EPR : Proportionality factor (g-factor) and Hyperfine Interactions. For the g-factor, based on the Zeeman Effect the energy difference of an electron with $s=1/2$ in magnetic field can be expressed as below. According to Plank's law $\Delta E=h\nu$ (h is Planck's constant), the microwave frequency involve in the equation where β is the constant, Bohr magneton and the magnetic field B.

$$\Delta E=g\beta B = h\nu$$

The g-factor is a constant of proportionality which represent the property of the electron. By using the constant values of h and β , g value can be shown as below.

$$g=71.4484\nu(\text{in GHz})/B (\text{in mT})$$

Knowing the magnetic field and microwave frequency can give the g factor. For example, at the magnetic field of 331.85 mT, a free electron absorbs the microwave with an X-band frequency of 9.300 GHz so, a free electron in vacuum has a g value $g_e = 2.00232$.

On the other case, when the electron is in a certain circumstance, such as transition metal-ion complex, the additional magnetic field produced by the nuclei, ΔB , will also affect the electron. At this kind of surrounding, Equation will be

$$h\nu = g\beta(B_e + \Delta B)$$

A fingerprint which is Δg includes the chemical information like the interaction between the electron and the electronic structure of the molecule. Simply we express the value of $g = g_e + \Delta g$ as a fingerprint of the molecule. For organic radicals, the g value is very close to g_e with values ranging from 1.99-2.01. For transition metal complexes, the g value diverse in large range (1.4-3.0) because of the spin-orbit coupling and zero-field splitting and it depends on the geometry of the complex. The center of the signal apply to calculate the g factor of the absorption in the spectrum. The value of g factor is related to the electronic environment, as well as related to anisotropy.

The magnetic moments of atoms nuclei in a molecule or complex are their own properties. The hyperfine interaction is occurred between the electron and the nuclei produced local magnetic field. The energy level of the electron is below, where

$$E = g m_B B_0 M_S + a M_S m_I$$

B_0 is applied magnetic field, a is the hyperfine coupling constant, m_I is the nuclear spin quantum number. Hyperfine interactions give many information such as the number and identity of atoms in a molecule or compound, distance from the unpaired electron.

Table A-1 Bio transition metal nuclear spins and EPR hyperfine pattern

Metal	Valency	Isotope	Spin (abundance)	EPR lines
V	IV	51	7/2	8
Mn	II	55	5/2	6
Fe	III	54, 56, 57, 58	0 + 1/2 (2%)	1 + 2 (1%)
Co	II	59	7/2	8
Ni	III, I	58, 60, 61, 62, 64	0 + 3/2 (1%)	1 + 4 (0.25%)
Cu	II	63, 65	3/2	4
Mo	V	92, 94, 95, 96, 97, 98, 100	0 + 5/2 (25%)	1 + 6 (4%)
W	V	180, 182, 183, 184, 186	0 + 1/2 (14%)	1 + 2 (7%)

The common thing between NMR and EPR is the rules for determining which nuclei will interact. The ground state nuclear spin quantum number, I , of isotopes which have even atomic and even mass numbers is zero, and these isotopes have no EPR (or NMR) spectra. On the other hands, with odd atomic numbers and even mass numbers, the values of I are integers. The isotopes with odd mass numbers, the values of I are fractions. For example, the spin of ^2H and ^1H are 1 and $1/2$, respectively and the spin of ^{23}Na is $7/2$.

Table A-2 Bio ligand atom nuclear spins and their EPR hyperfine pattern

Ligand	Isotope	Spin (abundance)	EPR lines
H	1, 2	$1/2 + 1$ (0.015%)	2 + 3
C	12, 13	$0 + 1/2$ (1.1%)	1 + 2
N	14, 15	$1 + 1/2$ (0.4%)	3 + 2
O	16, 17, 18	$0 + 5/2$ (0.04%)	1 + 6
F	19	$1/2$	2
P	31	$1/2$	2
S	32, 33, 34	$0 + 3/2$ (0.8%)	1 + 4
Cl	35, 37	$3/2$	4
As	75	$3/2$	4
Se	76, 77, 78, 80, 82	$0 + 1/2$ (7.6%)	1 + 4
Br	79, 81	$3/2$	4
I	127	$5/2$	6

The formula provides the number of lines from the hyperfine interaction $2NI + 1$. N is the number of equivalent nuclei and I is the spin. The coupling relative intensity of each line is determined by the number of interacting nuclei and the most common $I=1/2$ nuclei the intensity follows Pascal's triangle.

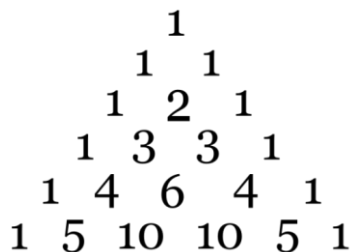


Figure A-12 Pascal's triangle $I=1/2$ and relative Intensities of each line

A.6. Mass Spectrometry (MS)

Mass spectrometry is an analytical technique used to detection and characterization of the materials, in terms of ionizes chemical species into a spectrum based by their mass-to-charge ratio (m/z). There are 3 main functions and their associated components. A sample is ionized by losing an electron (gas phase ions of the compound) and high energy beam of electrons affect ionization in the ion source. Then the mass analyzer distinguishes the separated ions (fragments) can be sorted by their mass and charge. Finally, they detected electronically and the information on a screen.

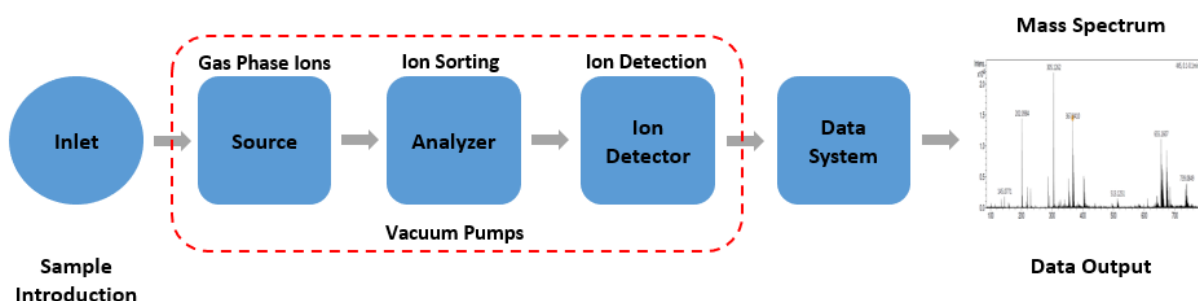
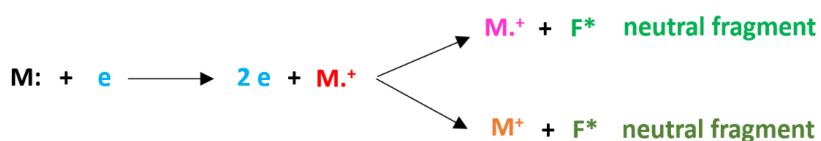


Figure A-13 Components of Mass Spectrometer



Electrospray ionization Mass Spectrometry (ESI-MS) is one of popular ionization technique for MS. The electrospray is made by using a high voltage and it affect that droplets become desolvated via combination of heat, vacuum and acceleration. Usually it is used for larger molecules that the ions may contain multiple charges and it allows to detect of very large molecules which have limitation mass to charge ratio ranges.

For analysis of diverse metal complexes, mass spectra were used, and it was manipulated by MicroTOFq (Bruker, 2009) with the ESI^+ or ESI^- method in high resolution mode. Samples were prepared by diluting 1 mg of product in 1 mL of solvent (water or MeOH) and these solutions were diluted 10 times in ACN.

A.7. Transient Absorption (TA) / Laser Flash photolysis (LFP)

Transient Absorption / Laser Flash Photolysis is a technique applied by a short intense light pulse from a pulsed laser source (pump source). It is used to study kinetic and mechanism of chemical species by absorption and emission change at certain wavelength. The intense light pulse brings photo-excited intermediates (excited states, radicals and ions) which might be long or short-lived depends on the photo properties of the molecules. Then the absorption characters which modified temporally can be observed. For a probe source, a spectrally continuous Xenon lamp is used and to improve the photon flux it is operated in a pulsed mode. Kinetic and spectral mode are two modes of operation of the laser flash photolysis spectrometer. In kinetic mode, it provides the decay of the species at a single wavelength as a function of time. In spectral mode, the spectra are measured at a specific time after excitation using an ICCD detector. The transient spectral features give information of the transient species which was exposed only a few laser shots. This is especially useful to study electron transfer which can easily influence by light.

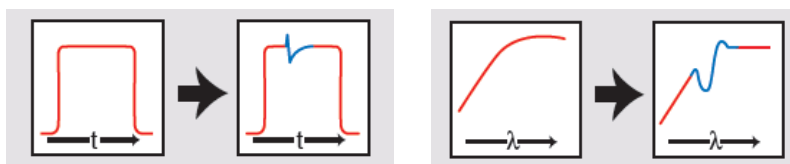


Figure A-14. Kinetic data acquisition (left) and Spectral data acquisition (right)

Edinburgh Instruments LP920 flash photolysis spectrometer system was used for both transient absorption kinetics and time-resolved spectral measurements. A Continuum Surelite Q-switched Nd:YAG laser coupled with Continuum optical parametric oscillator (OPO) for sample excitation (~5 ns pulse duration at a wavelength of 460 nm with a typical laser energy of 10 mJ per flash) was incorporated. The probe source was a pulsed 450 W xenon arc lamp for the transient absorption measurements. Detection of the signal was performed either by a Hamamatsu photomultiplier tube (PMT) for kinetic mode or a water-cooled Andor intensified charge coupled device (ICCD) camera for spectral mode.

A.8. Clark Electrode

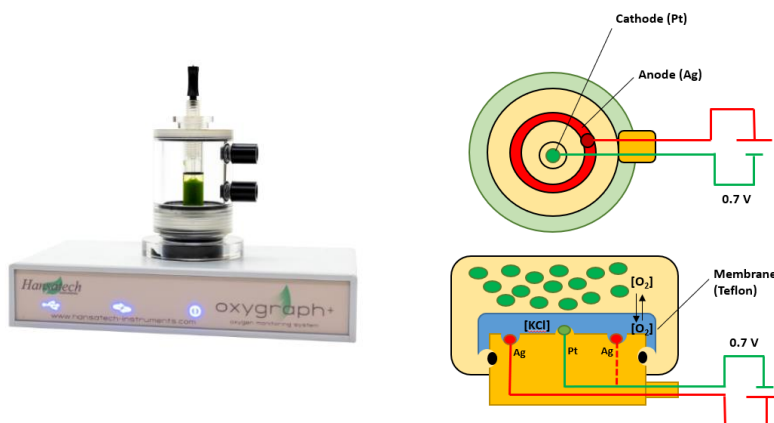


Figure A-15. Hansatech Instruments oxygen electrode systems (left) scheme of the oxygen electrode (right)

Clark electrode is oxygen electrode system which measures in two phases, liquid or gas-phase. The measurement is detected dissolved oxygen in liquid-phase systems or gas-phase systems. The oxygen electrode disc consists of a platinum cathode and a silver anode in an electrolyte solution. They are set in an epoxy resin disc. The cathode which located in the center of a dome and the silver anode in a circular groove as shown in Fig. A-15. The electrodes are protected by a thin teflon membrane which traps a thin layer of electrolyte (potassium chloride) over the surface of the electrodes. A paper spacer is placed at the bottom of the membrane to provide a uniform layer of electrolyte between anode and cathode. When a voltage is applied to the electrodes, from the cathode (Pt) electrode to the anode (Ag), the current becomes polarized. When the potential is reached to 0.7 V, oxygen is reduced at the platinum surface to hydrogen peroxide H_2O_2 then the polarity discharge as electrons are donated to oxygen which acts as an electron acceptor.

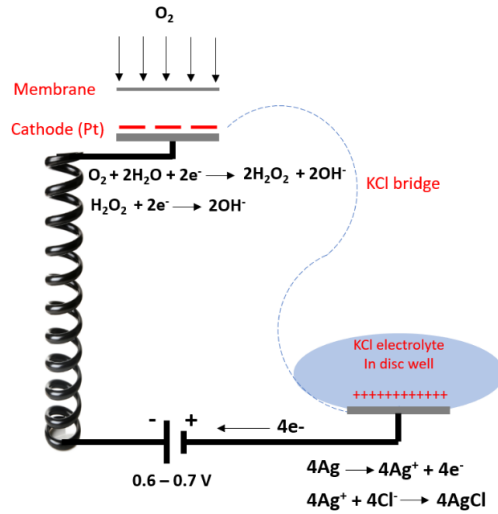


Figure A-16 Oxygen electrode reactions in Clark electrode

The diagram in Fig. A-16 shows the oxygen electrode reactions. When a potentiating voltage is applied across the two electrodes, the platinum (Pt, cathode) becomes negative and the silver (Ag, anode) becomes positive. The Oxygen reduce at the cathode surface then current flows through the circuit. On the other hands, the silver is oxidized and silver chloride deposits on the anode.

A.9. Glove box system

Glove box is a leak-tight container to control atmospheres or to use with hazardous substances. It protects from dangerous materials and provides safe surrounding for contamination or oxygen-sensitive materials. As purpose, there are two types of glove boxes. To manipulate in oxygen-free atmosphere, the glove box controlled by argon or nitrogen and we called it Inert atmosphere work. In my experiment, to prevent the reaction of methylviologen (MV^{2+}) with oxygen, the experiments were manipulated in glove box.



Figure A-17. Glove box

(B) Synthesis and Characterizations

B.1. [Ni^{II}OPBI](TMA)₂

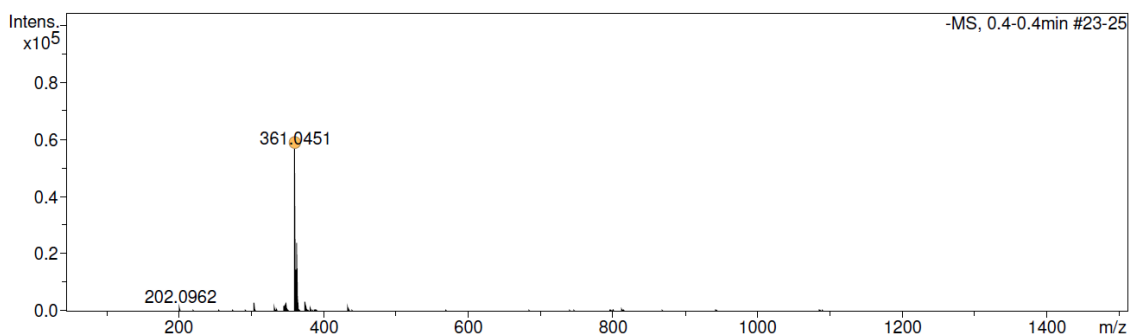
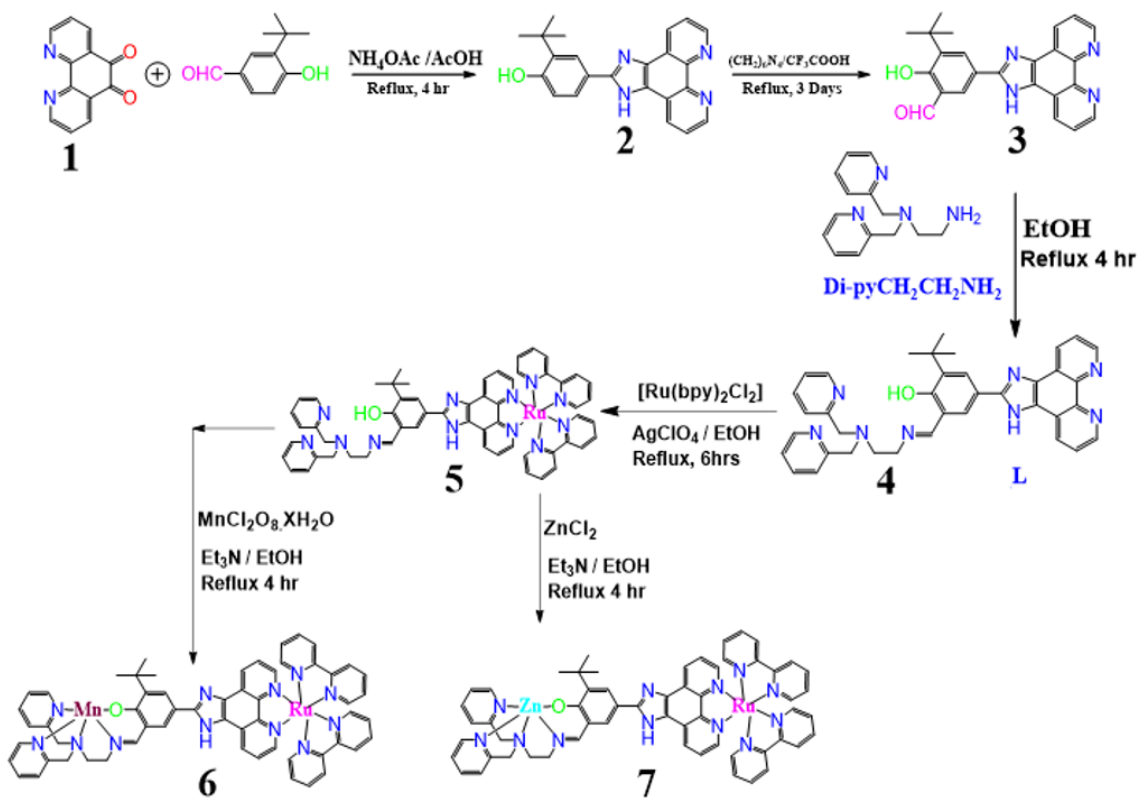


Figure B-1 ESI-MS (negative mode) of the complex Ni OPBI anion, [NiL+H]⁻ (m/z = 361.04)

B.2. Ru^{II}LMn^{III}



Scheme B-1 Synthesis pathway for the formation of Ru^{II}LMn^{III} (6) and Ru^{II}LZn^{II} (7).

The ligand (**4**) was characterized by ^1H NMR and Mass spectroscopy. ^1H NMR (400 MHz, DMSO) δ 11.99 (s, 1H), 10.16 (s, 1H), 9.02 (d, $J = 2.7$ Hz, 2H), 8.96 (d, $J = 6.1$ Hz, 2H), 8.62 (d, $J = 40.8$ Hz, 2H), 8.48 (t, $J = 7.2$ Hz, 2H), 8.20 (d, $J = 9.0$ Hz, 1H), 7.84 (dd, $J = 7.7, 4.1$ Hz, 1H), 7.62 (dd, $J = 10.7, 4.4$ Hz, 2H), 7.56 (d, $J = 7.7$ Hz, 2H), 7.25 – 7.19 (m, 2H), 3.87 (s, 4H), 3.38 (s, 2H), 2.84 (dd, $J = 13.9, 8.6$ Hz, 2H), 1.52 (d, $J = 10.8$ Hz, 10H).

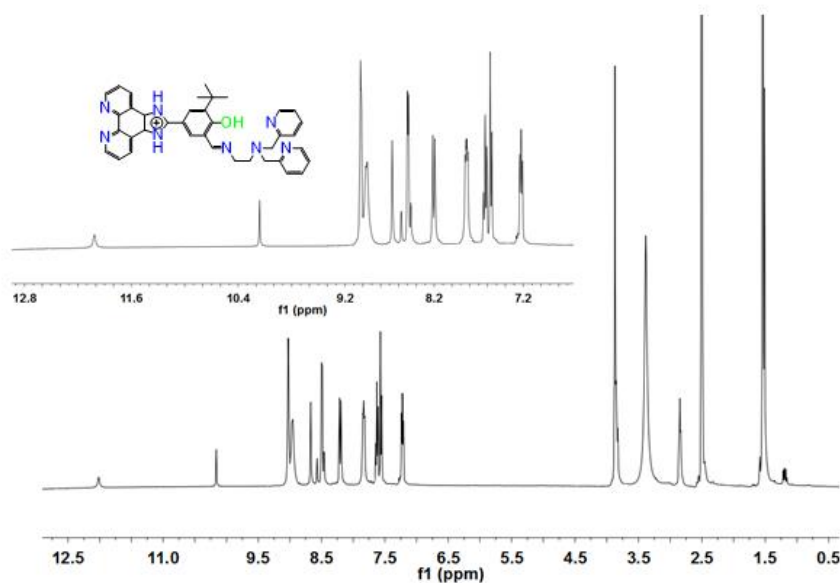


Figure B-2 NMR spectra for the ligand (L) in DMSO solvent.

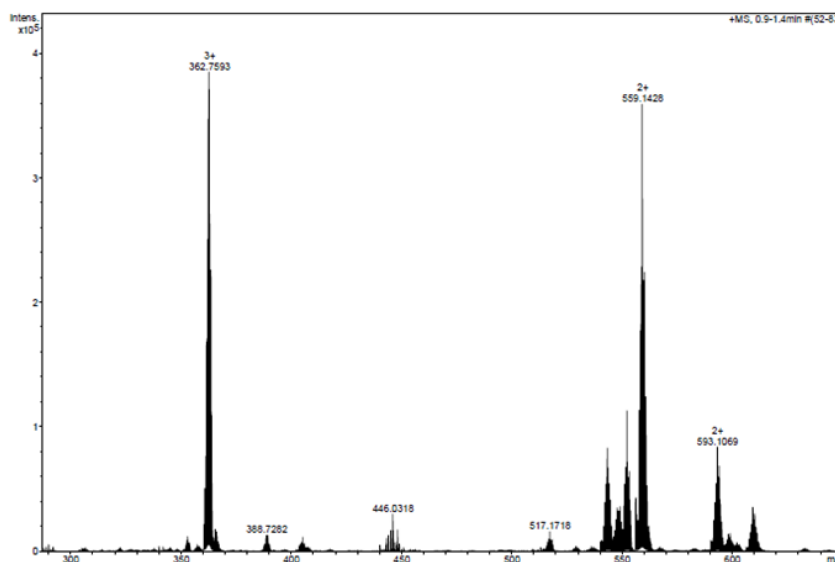


Figure B-3 ESI-MS (positive) for the complex $\text{Ru}^{\text{II}}\text{LMn}^{\text{III}}$ (**6**) cations, $[(\text{bpy})_2\text{Ru}(\text{HL})\text{Mn}]^{3+}$ ($m/z = 362.75$), $[(\text{bpy})_2\text{Ru}(\text{HL})\text{Mn}]^{2+}$ ($m/z = 593.10$) and $[(\text{bpy})_2\text{Ru}(\text{HL})(\text{OMe})\text{Mn}]^{2+}$ ($m/z = 559.14$).

(C) X-ray Crystal Structure

X-ray diffraction data for compounds was collected by using a VENTURE PHOTON100 CMOS Bruker diffractometer with Micro-focus IuS source Mo K α radiation. X-ray diffraction data were collected by using a VENTURE PHOTON100 CMOS Bruker diffractometer with Micro-focus IuS source Cu K α radiation. Crystals were mounted on a CryoLoop (Hampton Research) with Paratone-N (Hampton Research) as cryoprotectant and then flashfrozen in a nitrogen-gas stream at 100 K. For compounds, the temperature of the crystal was maintained at the selected value by means of a 700 series Cryostream or an N-Helix to within an accuracy of ± 1 K. The data were corrected for Lorentz polarization, and absorption effects. The structures were solved by direct methods using SHELXS-97 and refined against F by full-matrix least-squares techniques using SHELXL-2018 with anisotropic displacement parameters for all non-hydrogen atoms. All calculations were performed by using the Crystal Structure crystallographic software package WINGX.

C.1. [Cu^{II}OPBI](TMA)₂ and [Cu^{II}OPBI]MV

Table C-1 Crystallographic data and structure refinement details.

Compound	[Cu ^{II} OPBI](TMA) ₂	[Cu ^{II} OPBI]MV
Empirical Formula	C ₁₄ H ₁₄ Cu N ₄ O ₄ , 2(C ₃ H ₇ N O), 2(C ₄ H ₁₂ N), H ₂ O	C ₁₄ H ₁₅ Cu N ₄ O ₄ , 0.5(C ₁₂ H ₁₄ N ₂), 3(H ₂ O)
<i>M_r</i>	678.33	514.01
Crystal color	very pale pink	pale yellow
Crystal size, mm ³	0.12 x 0.10 x 0.025	0.12 x 0.07 x 0.03
Crystal system	monoclinic	triclinic
Space group	<i>C</i> 2/ <i>m</i>	<i>P</i> -1
<i>a</i> , Å	24.3426(7)	8.943(14)
<i>b</i> , Å	6.6902(2)	10.464(14)
<i>c</i> , Å	21.4391(6)	12.522(16)
α , °	90	100.63(3)
β , °	101.1270(10)	106.29(3)
γ , °	90	93.06(4)
Cell volume, Å ³	3425.87(17)	1099(3)
<i>Z</i> ; <i>Z'</i>	4 ; 1/2	2 ; 1
<i>T</i> , K	100 (1)	100 (1)
Radiation type ; wavelength Å	CuK α ; 1.54178	MoK α ; 0.71073
<i>F</i> ₀₀₀	1452	536
μ , mm ⁻¹	1.347	1.046
θ range, °	2.100 - 66.693	2.353 - 30.609
Reflection collected	24 881	34 789
Reflections unique	3 303	6 714
<i>R</i> _{int}	0.0364	0.2298
GOF	1.049	0.993
Refl. obs. (<i>I</i> > 2 σ (<i>I</i>))	3 051	3 151
Parameters	287	303
w <i>R</i> ₂ (all data)	0.0897	0.2141
<i>R</i> value (<i>I</i> > 2 σ (<i>I</i>))	0.0347	0.0741
Largest diff. peak and hole (e ⁻ ·Å ⁻³)	0.567 ; -0.624	1.345 ; -1.201

C.2. [Cu^{II}OPBI]MV (in glove box, Oxygen-free condition)

It was obtained by slow diffusion of diethyl-ether and the dissolved compound in mixture solvents of acetonitrile and methanol. To make the oxygen-free condition, all experiments were manipulated in glove box, which had low concentration of oxygen (< 10 ppm).

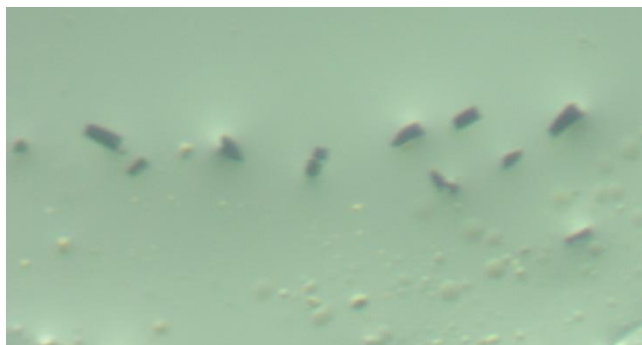


Figure C-1 Microscopic Crystal of CuLMV in glove box.

C.3. [Ni^{II}OPBI](TMA)₂

Crystal of NiL(TMA)₂ was obtained by slow diffusion of diethyl-ether in DMF solution of the compound.



Figure C-2 Microscopic Crystal of Cu OPBI MV (left) and its structure (right).

Table C-2 Crystallographic data and structure of NiL(TMA)₂ refinement details.

Compound	NiL(TMA) ₂
Empirical Formula	C ₁₄ H ₁₄ N ₄ Ni O ₄ , 2(C ₄ H ₁₂ N), 5/2(H ₂ O)
<i>M_r</i>	549.29
Crystal color	orange
Crystal size, mm ³	0.18 x 0.07 x 0.04
Crystal system	monoclinic
Space group	<i>C</i> 2/ <i>c</i>
a, Å	16.7611(10)
b, Å	8.7767(5)
c, Å	37.022(2)
α, °	90
β, °	100.958(2)
γ, °	90
Cell volume, Å ³	5346.9(5)
Z ; Z'	8 ; 1
T, K	100 (1)
Radiation type ; wavelength Å	MoKα; 0.71073
F ₀₀₀	2336
μ, mm ⁻¹	0.774
θ range, °	2.241 - 30.792
Reflection collected	122 201
Reflections unique	8 321
R _{int}	0.0654
GOF	1.188
Refl. obs. (<i>I</i> >2σ(<i>I</i>))	7 166
Parameters	347
wR ₂ (all data)	0.1301
R value (<i>I</i> >2σ(<i>I</i>))	0.0509
Largest diff. peak and hole (e ⁻ .Å ⁻³)	0.837 ; -0.696

C.4. [Cu^{II}OBBZ](TBA)₂

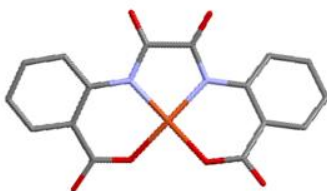


Figure C-3 Structure of Cu^{II}OBBZ

Table C-3 Crystallographic data and structure of Cu OBBZ(TBA)₂ refinement details.

Compound	Cu OBBZ(TBA) ₂
Empirical Formula	C ₁₆ H ₈ Cu N ₂ O ₆ , 2(C ₁₆ H ₃₆ N), 8(H ₂ O)
<i>M_r</i>	1016.82
Crystal color	pale blue
Crystal size, mm ³	0.10 x 0.06 x 0.03
Crystal system	triclinic
Space group	<i>P</i> - 1
a, Å	11.864(3)
b, Å	12.475(4)
c, Å	21.600(6)
α, °	105.463(12)
β, °	92.923(12)
γ, °	113.023(12)
Cell volume, Å ³	2792.0(14)
Z ; Z'	2 ; 1
T, K	100 (1)
Radiation type ; wavelength Å	MoKα; 0.71073
F ₀₀₀	1106
μ, mm ⁻¹	0.452
θ range, °	2.263 - 32.771
Reflection collected	128 088
Reflections unique	20 488
R _{int}	0.0968
GOF	1.027
Refl. obs. (<i>I</i> >2σ(<i>I</i>))	14 965
Parameters	612
wR ₂ (all data)	0.1321
R value (<i>I</i> >2σ(<i>I</i>))	0.0526
Largest diff. peak and hole (e ⁻ .Å ⁻³)	0.783 ; -1.147

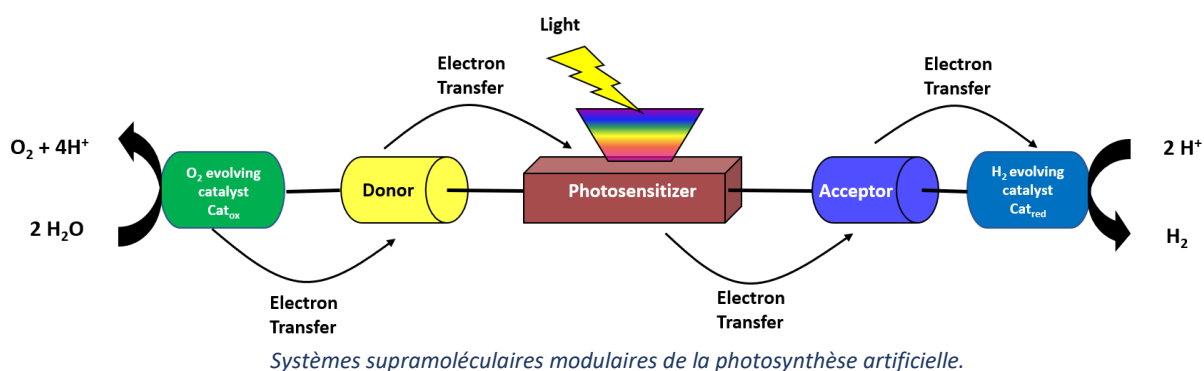
References

1. A.J. Bard, L.R. Faulkner, *Electrochemical methods: fundamentals and application*, 2nd ed., John Wiley & Sons, Inc., New York, **2001**.
2. F. C. Anson, *Electroanalytical Chemistry, ACS Audio Course Manual*, ACS, Washington, D. C., **1976**, 55.
3. L. R. Faulkner, *Chem. Educ.*, **60**, **1983**, 262.
4. L. R. Faulkner, *Physical Methods in Modern Chemical Analysis*, Vol. 3, Ed Academic, New York, **1983**.
5. H. H. Perkampus, *UV-VIS spectroscopy and its applications*, Berlin:Springer-Verlag, **1992**.
6. Bougeard, M. Buback, A. Cao, *Infrared and raman spectroscopy : methods and applications*, Weinheim VCH, cop. **1995**.
7. A. C. Testa and W. H. Reinmuth, *Anal. Chem.*, **33**, **1961**.
8. Breitmaier, E., *Structure elucidation by NMR in organic chemistry : a practical guide.*, Wiley, West Sussex, England, **2002**.
9. K. C. Khulbe, A. F. Ismail, T. Matsuura, *Electron Paramagnetic Resonance Spectroscopy, Membrane Characterization*, Elsevier, **2017**.
10. K. Downard, *Mass Spectrometry, The Royal Society of Chemistry*, **2004**.
11. R. Berera, R. van Grondelle, J. T. M. Kennis, *Photosynthesis Research* **2009**, *101*, 105–118.
12. L. C. Clark, R. Wolf, D. Granger, Z. Taylor, *Journal of Applied Physiology* **1953**, *6*, 189–193.
13. Sheldrick, G. M. SHELXS-97, Program for Crystal Structure Solution, University of Göttingen, Göttingen, Germany, **1997**.
14. Sheldrick, G. M. *Acta Crystallogr., Sect. A: Found. Crystallogr.*, **2008**, *64*, 112-122.
15. Farrugia, L. J. *J. Appl. Cryst.* **1999**, *32*, 837.

Résumé (en français)

En guise de préambule, je voudrais souligner que le présent travail n'a été effectué que depuis mai 2018. Je ai mené mon projet de recherche dans le groupe de la «photosynthèse artificielle» que pendant 17 mois. Compte tenu des contraintes de temps, je n'étais pas en mesure de mener à bien les tâches que je visais. Dans ce manuscrit, j'ai rassemblé mes résultats et j'ai pu, en partie, apporter de nouvelles perspectives et compréhension, alors que dans d'autres, des études plus approfondies seront nécessaires pour apporter plus de connaissances.

Mon travail de thèse s'articule autour du thème de la photosynthèse artificielle.



Le développement de sources d'énergie renouvelables telles que les combustibles solaires est une question cruciale dans le contexte actuel du réchauffement de la planète. L'eau est une source abondante, respectueuse de l'environnement, bon marché et abondante en électrons et en protons nécessaires à la production de combustible. Par conséquent, l'oxydation de l'eau activée par la lumière est une étape clé de la photosynthèse artificielle et le développement de catalyseurs efficaces, robustes et durables constitue un objectif important pour les chimistes.

La photosynthèse artificielle vise à extraire les principes de base de la photosynthèse naturelle et à les mettre dans un dispositif «artificiel» pour convertir l'énergie solaire en énergie chimique. Il entreprend trois étapes principales : capturer l'énergie lumineuse par photosensibilisateur, transférer cette énergie sous forme d'états à charge séparée et générer une source de combustible chimique lors de réactions d'oxydoréduction. Ce manuscrit consiste en :

Une Introduction générale qui aborde les problèmes d'énergie et la photosynthèse artificielle en termes d'étude électrochimique et photochimique de l'oxydation de l'eau. De plus, le concept de base du transfert d'électrons et de la formation de paires d'ions sont mentionnés. La fin du chapitre explique les objectifs de ce travail.

Le chapitre 2. Dans ce chapitre nous nous concentrons sur le développement de tels catalyseurs basés sur des complexes métalliques à base de métaux de la première série des éléments de transition tel que le cuivre pour cette étude. L'électrocatalyse et la photocatalyse par oxydation de l'eau ont été étudiées. Nous décrivons l'oxydation électrochimique de l'eau avec des complexes moléculaires de cuivre(II) bisoxamidate. Ces complexes ont fait l'objet de recherche dans notre laboratoire dans les 90's. Récemment, ces complexes ont été rapportés comme catalyseurs d'oxydation de l'eau par une équipe en Espagne. En collaboration avec l'équipe du Pr. Abhishek Dey à Calcutta nous avons voulu mieux comprendre les mécanismes de fonctionnement de ces catalyseurs moléculaires. J'ai d'abord préparé une série de complexes de cuivre(II) oxamidate avec différents substituents, Me, Cl et NO₂. Pour ma part, j'ai effectué des électrochimiques en solutions en faisant varier les conditions de pH. J'ai pu mettre en évidence l'évolution du potentiel d'oxydation de l'eau en fonction de la nature des substituents. Les résultats, obtenus par nos collaborateurs ont montré une évolution nette dans les étapes d'activation de la molécule d'eau. Nous avons aussi la possibilité de faire la photo-oxydation de l'eau en utilisant un photosensibilisateur tel que le ruthénium(II) trisbipyridine et un accepteur d'électron. Cependant, cette étude nous a conduit vers d'autres problématiques que nous décrivons dans le **chapitre 3**.

Au chapitre 3. Formation des paires d'ions : Nous avons remarqué dans les études de photoactivation du complexe de Cu(II), un transfert d'électron dans l'état excité du photosensibilisateur. De plus nous avons observé un phénomène très intrigant lors de l'ajout de l'accepteur d'électron le méthyleviologène et le complexe de cuivre(II). En effet bien que la thermodynamique soit défavorable nous observons un transfert d'électron du complexe de cuivre(II) vers l'accepteur d'électron dans l'état fondamentale. Ce phénomène a été mis en évidence par la spectroscopie RPE et l'UV-Visible.

Le chapitre 4. Transfert d'électron intramoléculaire, nous avons synthétisé des assemblages modulaires constitués d'un chromophore photoactif et d'un catalyseur de manganèse. Nous avons étudié les processus de transfert d'électrons intramoléculaires et les caractérisations photophysiques. Nous avons pu montrer que nous pouvons photooxyder le complexe de Mn(III) en Mn(IV) et aussi nous avons réalisé des études de photocatalyse d'oxydation de substrats organiques.

Par conséquent, l'étude des complexes moléculaires pour la photosynthèse artificielle fournit diverses orientations pour développer le rendement d'utilisation de l'énergie solaire.

Tous les détails des principes expérimentaux, des caractérisations et des structures cristallines des complexes sont décrits en **Annexe**.

Titre : Complexes moléculaires pour la photosynthèse artificielle

Mots clés : Photosynthèse artificielle, Transfert électron photo-induit, Oxydation de l'eau, Paire d'ions, Transfert électron

Résumé : Le développement de sources d'énergie renouvelables telles que les combustibles solaires est une question cruciale dans le contexte actuel du réchauffement de la planète. L'eau est une source abondante, respectueuse de l'environnement, bon marché et abondante en électrons et en protons nécessaires à la production de combustible. Par conséquent, l'oxydation de l'eau activée par la lumière est une étape clé de la photosynthèse artificielle et le développement de catalyseurs efficaces, robustes et durables constitue un objectif important pour les chimistes. Dans la première partie de cette étude, nous nous concentrons sur le développement de tels catalyseurs basés sur des complexes métalliques à base de métaux de la première série des éléments de transition tel que le cuivre pour cette étude. L'électrocatalyse et la photocatalyse par oxydation de l'eau ont été étudiées.

La deuxième partie du travail concerne la formation de paires d'ions entre les espèces à double charge opposée du catalyseur complexe et de l'accepteur d'électrons et du photosensibilisant et du catalyseur complexe. Cette étude devrait apporter des preuves solides de l'influence de chaque composant du photosystème par l'association et la dissociation de paires d'ions.

Dans la troisième partie, nous étudions un système synthétique sensibilisant-catalyseur capable de photoactiver une molécule d'eau liée à l'unité catalytique par le biais d'une oxydation à deux électrons et à deux protons, réalisant toute la caractérisation photophysique de la dyade. Par conséquent, l'étude des complexes moléculaires pour la photosynthèse artificielle fournit diverses orientations pour développer le rendement d'utilisation de l'énergie solaire.

Title : Molecular complexes for artificial photosynthesis

Keywords : Artificial photosynthesis, Photo-induced electron transfer, Water oxidation, Ion pair, Electron transfer

Abstract : Development of renewable energy sources like solar fuels is a crucial issue in the actual context of global warming. Water is an environmentally friendly, cheap and abundant source of the electrons and protons needed for fuel production. Therefore, light-activated water oxidation is a key step in artificial photosynthesis and the development of efficient, robust and sustainable catalysts is an important goal for chemists. In the first part of this study, we focus on the development of such catalysts based on earth abundant copper complexes. The water oxidation electrocatalysis and photocatalysis were investigated.

The second part of the work concerns the ion pair formation between the oppositely double charged species of complex catalyst and electron acceptor and Photosensitizer and complex catalyst are investigated. This study should bring solid evidence on the influence of each component in photosystem through the ion pair association and dissociation. In the third part, we study a synthetic sensitizer-catalyst system that can photoactivate a water molecule bound to the catalytic unit through a two-electron, two-proton abstraction, performed all the photophysical characterization of the dyad. Therefore, studying molecular complexes for artificial photosynthesis provides diverse direction to develop the utilization efficiency of solar energy.

